Dissertation

submitted to the

Combined Faculty of Mathematics, Engineering and Natural Sciences

of Heidelberg University, Germany

for the degree of

Doctor of Natural Sciences

Put forward by

Varsiha Sothilingam

Born in: London, United Kingdom

Oral examination: 14th July 2025

Probing Anomalous Gauge Couplings via Photon-Induced WW Production with Forward Protons at the ATLAS Experiment

Referees: Prof. Dr. Monica Dunford

Prof. Dr. Stephanie Hansmann-Menzemer

Abstract

Photon-induced WW production in proton-proton collisions at the Large Hadron Collider provides a clean environment to probe the electroweak structure of the Standard Model. Quasi-real photons, emitted by the electromagnetic fields of the protons, collide peripherally. The protons that remain intact scatter into the forward region of the experiment, where the ATLAS Forward Proton (AFP) detectors can measure their kinematic properties. This enables the full kinematic reconstruction of the WW system, independent of the central ATLAS detector. This thesis presents the measurement of the semileptonic photon-induced WW production in Run 2 of LHC at a centre-of-mass energy of $\sqrt{s} = 13$ TeV, corresponding to an integrated luminosity of 14.6 fb^{-1}. Two reconstruction methods for the hadronically decaying W boson are studied: the resolved and boosted topologies. Both reconstructions are used to test the sensitivity to potential anomalous quartic gauge couplings. Data-driven techniques are employed to estimate background contributions, with cross-checks between different methods confirming consistency. Good agreement is observed between the background predictions and the observed number of events in data. The results are interpreted within the framework of the Standard Model Effective Field Theory, and are used to constrain the coefficients of dimension 8 operators. Confidence intervals for the anomalous quartic gauge couplings are derived, confirming existing limits.

Zusammenfassung

Die Struktur der elektoschwachen Wechselwirkung kann mit Hilfe von photoninduzierter WW-Produktion durch Proton-Proton-Kollissionen am Large Hadron Collider untersucht werden. Hierbei kollidieren quasi-reale Photonen, welche durch die elektromagnetischen Felder der Protonen emittiert werden, peripher. Die Protonen bleiben bei dieser Kollision intakt und werden dabei in die Vorwärts-Region des Experiments gestreut. In dieser Region können die kinematischen Eigenschaften der Protonen von den ATLAS Forward Proton (AFP) Detektoren vermessen werden. Dadurch wird eine vollständige Rekonstruktion der Kinematik des WW-Systems unabhängig von dem zentralen ATLAS Detektor ermöglicht. Diese Arbeit behandelt die Messung des semileptonischen Zerfalls von durch Photoninduktion erzeugten W-Boson-Paaren. Die Messung verwendet Daten aus dem Run 2 des LHCs bei einer Schwerpunktsenergie von $\sqrt{s} = 13$ TeV und enhält Daten, die einer integrierten Luminosität von 14.6 fb^{-1} entsprechen. Für diese Messung werden zwei Methoden zur Rekonstruktion des hadronischen Zerfalls des W-Bosons untersucht: Eine aufgelöste und eine boosted Topolgie. Beide Methoden werden benutzt um die Sensitivität auf anomale quartische Eichkopplungen zu evaluieren. Der Untergrund wird mit datenbasierten Verfahren abgeschätzt und die Konsistenz beider Methoden wurde durch Vergleichsstudien bestätigt. Die Zahl beobachteter Ereignisse ist konsistent mit dem erwarteten Untergrund. Die Ergebnisse der Studie werden im Kontext der effektiven Feldtheorie des Standardmodells interpretiert und benutzt, um die Koeffizienten der Operatoren der Dimension acht einzugrenzen. Daraus können Konfidenzintervalle für die anomalen quartischen Eichkopplungen bestimmt werden, welche bereits bestehende Grenzen bestätigen.

CONTENTS

CHAPTER 1

INTRODUCTION

Understanding the fundamental building blocks of matter and the forces that govern their interactions is a central aim of particle physics. Over the past decades, this pursuit has led to the development of the Standard Model - a theoretical framework that successfully describes the electromagnetic, weak, and strong interactions among elementary particles. This theory has been confirmed by many experimental results at high energy particle colliders such as the Large Hadron Collider (LHC). The discovery of the Higgs boson in 2012 by the ATLAS and CMS experiments [1, 2] at the LHC was a hallmark achievement of the Standard Model, confirming the mechanism responsible for providing the elementary particles mass. Despite the successes of this theory, several profound questions remain unanswered, such as the origin of neutrino masses, the matter-antimatter asymmetry and the nature of dark matter. Theories beyond the Standard Model can offer potential solutions to these questions.

The ATLAS experiment is a general-purpose detector at the LHC and is designed to perform precise measurements of known processes as well as search for rare particles produced in proton-proton collisions. One avenue explored by the experiment is the measurement of the multiboson interactions in the electroweak sector. Such measurements simultaneously test the Standard Model and probe New Physics interactions which may modify the boson couplings.

Small deviations between the Standard Model predictions and what is observed in the experiments can be quantified through New Physics theories. One unique test is the interaction of photon-induced production of the W bosons via the interaction $\gamma\gamma \to WW$. At the TeV energy scales of the LHC, the electromagnetic fields of the protons emit quasi-real photons. The photons interact peripherally, resulting in photon-induced processes. The protons in these interactions scatter at very small angles and can be experimentally reconstructed with the ATLAS Forward Proton (AFP) detector. The proton kinematics

reconstructed in the AFP detector are matched with the kinematic properties of the semileptonic WW decays reconstructed in the ATLAS detector. This provides a unique constraint on the event topology as the energy of difference between the protons and WW bosons can be used to distinguish photon-induced processes from other background contributions. This process directly probes the self-interactions of the electroweak gauge bosons, a fundamental aspect of the Standard Model that arises from its non-Abelian $\mathrm{SU(2)_L} \otimes \mathrm{U(1)_Y}$ symmetry. Measurements of this distinctive experimental signature, with the use of the AFP detector, provides a unique foundation to test the Standard Model predictions. Any observed anomaly could hint at modifications to the gauge structure, such as the presence of anomalous quartic gauge couplings.

This thesis will explore the search for semileptonic photon-induced WW production and quantify the limits one can set on potential anomalous gauge boson couplings. It is the first measurement of anomalous couplings in this process by the ATLAS experiment which also takes advantage of the forward detectors. Two reconstructions of the hadronic final state objects will be studied: the resolved and boosted topologies. The limits set using the two different reconstruction methods will be tested and compared.

The structure of this thesis is as follows: the theoretical overview of the Standard Model and new physics models will be presented in Chapter 2. The experimental setup of the LHC, ATLAS experiment and ATLAS Forward Proton detector will be presented in Chapter 3. The particle reconstruction algorithms applied to the detector signals from data collected and simulations are summarised in Chapter 4. The generation of simulations is described in Chapter 5, along with the data-driven methodology implemented to reconstruct pileup protons in the AFP detector. The data and simulations will have kinematic criteria applied to the various particles in order optimise the search for the photon-induced process. The event selection applied to the resolved and boosted channels will be presented in Chapter 6 alongside the analysis strategy. The estimation of the backgrounds in the signal regions is described in Chapter 7 with discussion of the systematics for both channels. The results of this analysis are shown in Chapter 8. This chapter will also present the Effective Field Theory interpretation of the unblinded results, quantifying the sensitivity this process has to anomalous couplings. Lastly, the work of this thesis will be summarised in Chapter 9. Additional material are supplemented by the Appendix and will be referenced to throughout the thesis when required.

Author's Contributions

This work is performed in the framework of the ATLAS collaboration, an international community that together conceived, constructed and operates the ATLAS detector. The recording of the data analysed in this thesis is a common effort, as it requires full time supervision of the detector. The author contributed to the collection of ATLAS Run 3 data through shifts in the experimental control room, with responsibilities for parts of the trigger and data acquisition system, and the run control system. Additionally work was completed to aid the commissioning of the Level-1 Calorimeter trigger system by implementation of the hardware trigger algorithms into a bitwise correct simulation. This work is now part of the complete ATLAS Level-1 trigger simulation in the ATLAS software framework, Athena. The author contributed to other analyses using the ATLAS Forward Proton Detector. Trigger studies were completed for the ATLAS Run 2 search of single diffractive dijets, focusing on optimisation of the jet and proton triggers. The Time-of-Flight subdetector of the AFP detector was commissioned by authors of Ref. [3] and the work was presented by the author at the LHCPhysics conference in 2023, with proceedings found in Ref. [4].

For the start of Run 3, the author was responsible for the commissioning of the AFP triggers in the early data collected at the ATLAS experiment. This involved measuring trigger rates and hit efficiencies of the AFP detector which can be used for photon-induced and diffractive searches performed with the AFP and ATLAS detectors. The author worked with and supervised a Master's student who commissioned the Minimum Bias Tile Scintillator triggers, also during the early Run 3 data taking period. This study was also focused on measuring tracking efficiencies using minimum bias data, found in Ref. [5].

The main analysis presented in this thesis, the measurement of anomalous gauge couplings in the semileptonic $\gamma\gamma \to WW$ process, was completed predominantly by the author and presented in this thesis. The software used for this analysis was developed by a large team of colleagues within the collaboration creating the "Common Analysis Framework" (CAF) [6]. The analysis team aided in production of part of the simulation samples produced and many lively discussions about the measurement. The rest of the simulations was produced by the author.

The full analysis was completed by the author. This includes development of a new analysis derivation format used to filter the simulation and data for only particles and objects of interest. The optimisation of this derivation format by the author was completed in order to reduce potential background contributions. The implementation of proton information from AFP into the CAF was done by the author. This provided the full setup to complete the measurement of this process, which can be found in this thesis.

CHAPTER 2

THEORETICAL OVERVIEW

The *Standard Model of Particle Physics* (SM) provides the theoretical foundation which underpins the interactions of fundamental particles, through a quantum field theory [7, 8]. A summary of the SM theory will be given in Section 2.1 where the limitations of the SM will be briefly explored. The success of this theory can be tested through particle interactions such as multiboson interactions. This thesis will explore the specific interaction of $\gamma\gamma \to WW$ which can be used to test the SM and additionally has sensitivity to New Physics. In Section 2.2 an extension to the SM via an Effective Field Theory is presented, allowing for New Physics interactions beyond that currently described by the SM. Sensitivity to this model will be studied in this thesis via the $\gamma\gamma \to WW$ process. A summary of vector-boson-scattering processes at the LHC will be provided in Section 2.3 comparing the differences between quark-induced and photon-induced boson scatterings.

2.1 The Standard Model of Particle Physics

The Lagrangian of the SM is constructed to be symmetric under the Poincaré group, with the combined local gauge group $\mathrm{SU(3)_C} \otimes \mathrm{SU(2)_L} \otimes \mathrm{U(1)_Y}$. The gauge group $\mathrm{SU(3)_C}$ is associated to the strong interaction which describes Quantum Chromodynamics in the SM [9, 10]. The $\mathrm{SU(2)_L} \otimes \mathrm{U(1)_Y}$ gauge group is associated to the unification of the electromagnetic and weak force in the Glashow-Salam-Weinberg model [11, 12, 13]. The Lagrangian of the SM is composed of the sum of four Lagrangians

$$\mathscr{L}_{\mathrm{SM}} = \mathscr{L}_{\mathrm{Gauge}} + \mathscr{L}_{\mathrm{Fermions}} + \mathscr{L}_{\mathrm{Higgs}} + \mathscr{L}_{\mathrm{Yukawa}}. \tag{2.1}$$

The gauge symmetries of the SM that give rise to the fundamental forces are described by the term $\mathscr{L}_{\mathrm{Gauge}}$. The fermionic fields describing the fundamental particles of matter in

the SM are encoded in the term $\mathscr{L}_{\text{Fermions}}$. The interaction of the gauge bosons interacting with the Higgs field prompting the spontaneous symmetry breaking is implemented by $\mathscr{L}_{\text{Higgs}}$. The final term, $\mathscr{L}_{\text{Yukawa}}$, describes the nature and coupling strengths of the interactions between the Higgs field and fermions. The implications of each term will be described in the subsequent sections.

Gauge Symmetries of the Standard Model

The gauge sector of the SM describes *gauge bosons* which mediate strong, weak and electromagnetic interactions. Each local gauge symmetry has associated gauge fields shown in Table 2.1.

Symmetry	Bosonic Fields
SU(3)_C	G^a_μ a $\in \{1, 2, .., 8\}$
SU(2)_L	W^i_μ i $\in \{1, 2, 3\}$
U(1)_Y	B_μ

Table 2.1. Summary of gauge fields associated to local gauge symmetries of the Standard Model.

The field strength tensors of the Lagrangian can be constructed from the gauge fields defined as:

$$G^a_{\mu\nu} = \partial_\mu G^a_\nu - \partial_\nu G^a_\mu + g_s f^{abc} G^b_\mu G^c_\nu, \tag{2.2}$$

$$W^i_{\mu\nu} = \partial_\mu W^i_\nu - \partial_\nu W^i_\mu + g\epsilon_{ijk} W^j_\mu W^k_\nu, \tag{2.3}$$

$$B_{\mu\nu} = \partial_\mu B_\nu - \partial_\nu B_\mu, \tag{2.4}$$

where f^{abc} are structure constants of the SU(3)_C group, ϵ_{ijk} is the structure constant of SU(2)_L and the coupling constants of the respective groups are g_s and g. The gauge terms provide the kinematic terms of the gauge fields. The additional terms in the case of the non-Abelian gauge groups can give rise to triple and quartic gauge interactions. The gauge Lagrangian of the SM can be written as [14]

$$\mathscr{L}_{\text{Gauge}} = -\frac{1}{4} G^a_{\mu\nu} G^{a\mu\nu} - \frac{1}{4} W^i_{\mu\nu} W^{i\mu\nu} - \frac{1}{4} B_{\mu\nu} B^{\mu\nu}. \tag{2.5}$$

The first term of the Lagrangian describing gauge symmetries provides a description of the gluon dynamics *Quantum Chromodynamics* (QCD). The SU(3)_C group is generated by the eight 3×3 Gell-mann matrices, λ^a with generators $t^a = \frac{1}{2}\lambda^a$ [15]. It relates to the structure constant f^{abc} by $[t^a, t^b] = if^{abc}t^c$. The generators do not commute and it can give rise to the gluon fields (G^a_μ) having self-interactions. Therefore the QCD component

of the gauge Lagrangian encodes the self interactions of gluons, both triple and quartic interactions. Gluon self interactions have been experimentally observed [16].

The g_s the strong coupling constant varies with the energy scale, Q^2. It can be written as $g_s = \sqrt{4\pi\alpha_s}$ where α_s is the fine structure. The fine structure, at leading order, is a function of the energy scale Q^2 and can be expressed as [7]

$$\alpha_s(Q^2) = \frac{12\pi}{(33 - 2n_f)\ln(Q^2/\Lambda^2_{QCD})}, \tag{2.6}$$

where n_f is the number of quark flavours and Λ_{QCD} represents the energy scale of QCD. If $Q^2 < \Lambda_{\mathrm{QCD}}$, it follows that α_s is too large for perturbative calculations in QCD. At this energy scale, quarks are bound by the strong force into colourless bound states, known as the process of *colour confinement*. This leads to the formation of hadrons which are colourless bound states constructed of two or three quarks. When α_s becomes small, with $Q^2 >> \Lambda_{\mathrm{QCD}}$, one can treat quarks and gluons as free particles, which are no longer bounded. This is known as asymptotic freedom and is reached at energy scales of $\Lambda_{\mathrm{QCD}} \sim$ 1 GeV [15].

Fermions of the Standard Model

Particles with half-integer spin are known as fermions. A summary of fermions in the SM can be found in Table 2.2. Fermions have intrinsic quantum numbers: the weak isospin ($\mathrm{I_3}$), the weak hypercharge (Y) and the electric charge (Q), where $\mathrm{Q} = \mathrm{I_3} + \frac{\mathrm{Y}}{2}$ [7]. Left handed fermions in a doublet have a third component of weak isospin equal to $\mathrm{I_3} = \pm 1/2$ and right handed fermions in a singlet have a third component of weak isospin equal to $\mathrm{I_3} = 0$. The SM also predicts that each fermion has an associated antiparticle of identical mass, that is opposite in charge. The potential exception to this are neutrinos [17]. Fermions are categorised into three generations, differing by mass and lifetime, where the third generation is the heaviest. They can be further categorised into *quarks* and *leptons* where only quarks can interact via the strong interaction.

Each generation of leptons comprises of a charged lepton and a neutral lepton known as a neutrino (ν). As seen in Table 2.2 there are three generations of charged leptons: the electron (e), the muon (μ) and the tau (τ), listed from the lightest to heaviest generation [18]. The neutrinos are labelled as electron neutrino (ν_e), muon neutrino (ν_μ) and tau neutrino (ν_τ) for the respective generations. Charged leptons can interact via both the weak and electromagnetic force while neutrinos only interact via the weak force due to its neutral electric charge. For left-handed charged leptons, the third component of weak isospin is $\mathrm{I_3} = +1/2$. They form a doublet with their corresponding neutrino, which carry a third component of weak isospin of $\mathrm{I_3} = -1/2$. The right-handed charged leptons form

a weak isospin singlet. The hypothesised right-handed neutrinos do not interact with any of the forces described by the SM [15]. Neutrinos are often considered to be massless, however the discovery of neutrino oscillations indicates neutrino masses [19, 20].

		Generations					
		I	II	III	I_3	Y	Q
Leptons	$\overrightarrow{\mathbf{e_L}}$	$\begin{pmatrix}\nu_e\\ e\end{pmatrix}_L$	$\begin{pmatrix}\nu_\mu\\ \mu\end{pmatrix}_L$	$\begin{pmatrix}\nu_\tau\\ \tau\end{pmatrix}_L$	$+1/2$ $-1/2$	-1 -1	0 -1
	$\mathbf{e_R}$	e_R	μ_R	τ_R	0	-2	-1
Quarks	$\overrightarrow{\mathbf{Q_L}}$	$\begin{pmatrix}u\\ d\end{pmatrix}_L$	$\begin{pmatrix}c\\ s\end{pmatrix}_L$	$\begin{pmatrix}t\\ b\end{pmatrix}_L$	$+1/2$ $-1/2$	$+1/3$ $+1/3$	$+2/3$ $-1/3$
	$\mathbf{u_R}$	u_R	c_R	t_R	0	$+4/3$	$+2/3$
	$\mathbf{d_R}$	d_R	s_R	b_R	0	$-2/3$	$-1/3$

Table 2.2. Summary of Standard Model fermions and their corresponding quantum numbers. Fermions can be organised into quarks and leptons.

There are six quarks, for which three have an electromagnetic charge of $Q = +2/3$ and are known as up-type quarks: up (u), charm (c) and top (t). The remaining three quarks have an electromagnetic charge of $Q = -1/3$, known as down-type quarks: down (d), strange (s) and bottom (b). For left handed quarks, up-type quarks have the third component of weak isospin of $I_3 = +1/2$ and for down-type, $I_3 = -1/2$. The right handed quarks form singlets with no third component of weak isospin. All quarks and gluons carry colour charges (red, blue, green) which are conserved quantities. The coupling of gluons to fermions conserves the quantum colour charge, therefore the only fermions gluons coupling to are quarks [7], explained further in the following sections.

The covariant derivative acting on fermion fields is constructed to determine the interactions between the fermions and gauge bosons. It follows as

$$D_\mu = \partial_\mu - ig_s\frac{\lambda^a}{2}G^a_\mu - ig\frac{\tau^i}{2}W^i_\mu - ig'\frac{Y}{2}B_\mu, \tag{2.7}$$

where τ^i are the generators of the $SU(2)_L$ gauge group and and g' is the coupling constant of $U(1)_Y$. The first generation of the fermion Lagrangian then follows

$$\mathscr{L}_{\text{Fermion}} = \sum_f \bar{f}\gamma^\mu D_\mu f, \tag{2.8}$$

where $f = \overrightarrow{\mathbf{e_L}}, \mathbf{e_R}, \overrightarrow{\mathbf{Q_L}}, \mathbf{u_R}, \mathbf{d}_R$. The covariant derivative acting on the singlet states will give a zero result due to the different matrix form. Therefore it eliminates interactions with right-handed fermions.

Higgs Mechanism in the Standard Model

The inclusion of mass terms in the electroweak component of the SM Lagrangian violates the local gauge invariance. Their masses are therefore obtained through spontaneous symmetry breaking. In QFT, the spontaneous symmetry breaking (SSB) of a system is designed in such a way that the complete Lagrangian is invariant under the symmetry while the vacuum state (i.e the state that minimises the Lagrangian), is not. This is done by introducing the Higgs Mechanism. The Higgs field is a complex scalar field realised as a colourless $\mathrm{SU(2)_L}$ doublet ϕ, where $\phi = \binom{\phi^+}{\phi^0}$ [21, 22]. The Higgs Lagrangian takes the form

$$\mathscr{L}_{\text{Higgs}} = (D_\mu \phi)^\dagger (D^\mu \phi) - V(\phi), \tag{2.9}$$

with a Higgs potential $V(\phi) = \mu^2 \phi^\dagger \phi + \lambda(\phi^\dagger \phi)^2$. For $\mu^2 < 0$ and $\lambda > 0$, the potential has the shape of a "Mexican hat" that is symmetric around a central point, with a ring of minima at the non-zero radius. At this potential the Higgs field has a vacuum expectation value v, breaking the symmetry spontaneously with the condition that

$$|\phi|^2 = \frac{\mu^2}{2\lambda} = \frac{v^2}{2}. \tag{2.10}$$

The Higgs field in the spontaneous broken state can be parametrised as $\phi_0 = \frac{1}{\sqrt{2}}\binom{0}{v+h}$ where h is the excitation of the Higgs field. Inserting ϕ_0 into the Higgs Lagrangian breaks the $\mathrm{SU(2)_L} \otimes \mathrm{U(1)_Y}$ gauge symmetry to $\mathrm{U(1)_Y}$ due to the vacuum expectation value being non-zero. The breaking of the symmetry results in three massless Goldstone bosons and a massive scalar boson. The $W^\pm$ and Z bosons absorb the goldstone bosons providing them mass. The absorbed goldstone bosons become the longitudinal polarisations of the $W^\pm$ and Z bosons. The physical $W^\pm_\mu$ gauge bosons can be constructed as:

$$W^\pm_\mu = \frac{1}{\sqrt{2}}(W^1_\mu \mp W^2_\mu) \tag{2.11}$$

The W^3_μ and B_μ fields mix to form the physical photon (A_μ) and Z boson in the following form:

$$A_\mu = \cos(\theta_W) B_\mu + \sin(\theta_W) W^3_\mu, \tag{2.12}$$

$$Z_\mu = -\sin(\theta_W) B_\mu + \cos(\theta_W) W^3_\mu, \tag{2.13}$$

where the Weinberg angle θ_W (weak mixing angle) is defined as:

$$\cos(\theta_\mathrm{W}) = \frac{g}{\sqrt{g^2 + g'^2}} \tag{2.14}$$

The masses of weak bosons can be quantified in terms of the couplings and the vacuum expectation value:

$$m_{\mathrm{Z}} = \frac{v\sqrt{g^2 + g'^2}}{2} = \frac{m_W}{\cos(\theta_{\mathrm{W}})}, \tag{2.15}$$

$$m_{\mathrm{W}} = \frac{vg}{2}, \tag{2.16}$$

$$m_{\mathrm{A}} = 0. \tag{2.17}$$

Reinstating the mass eigenstates of the vector bosons into the Gauge Lagrangian gives rise to interactions between gauge bosons as well as self-interactions such as the process of interest in this thesis, interactions between photons and $W^{\pm}$ bosons. The excitation h of the Higgs field corresponds to the Higgs boson. The first experimental observation of the Higgs boson was by ATLAS and CMS [1, 2], with a measurement of its mass, $m_H = 125$ GeV. The measurement of its mass completed the picture of the SM. Additionally the vacuum expectation value has also been measured experimentally to have a value of $v = 264$ GeV [23].

Yukawa Couplings in the Standard Model

The coupling strengths of the fermions to the Higgs field are the Yukawa couplings, y_f. The magnitude of the couplings are determined experimentally [23]. The masses of fermions, m_f, arise from the couplings and are related to the Yukawa couplings as

$$m_f = y_f \frac{v}{\sqrt{2}}. \tag{2.18}$$

The Yukawa Lagrangian takes the following form for first generation quarks

$$\mathscr{L}_{\mathrm{Yukawa}} = -y_d(\bar{u}_{\mathrm{L}}, \bar{d}_{\mathrm{L}},)\phi d_{\mathrm{R}} - y_u(\bar{u}_{\mathrm{L}}, \bar{d}_{\mathrm{L}},)\tilde{\phi} u_{\mathrm{R}} + \mathrm{h.c}, \tag{2.19}$$

with $\tilde{\phi} = i\sigma_2\phi^*$ and the Hermitian conjugate. Fermions of the second and third generation will form similar Lagrangians. The probability of quark transitions can be extracted from the elements of the Cabibbo-Kobayashi-Maskawa (CKM) matrix [23], which describes the relation between quark flavours and mass eigenstates. Transitions between generations of the same quark generation are maximal, whereas transitions between different generations are suppressed. For the three generations, the CKM matrix has three rotation angles and one complex phase. The complex phase is the only CP violating component of the SM.

Success and Limitations of the Standard Model

The SM is a very successful theory of particle physics. Many experimental tests of this model are in agreement with theoretical predictions. A summary of its experimental accomplishments is shown in Figure 2.1 which shows the experimental measurements of different particle processes with their theoretical predictions.

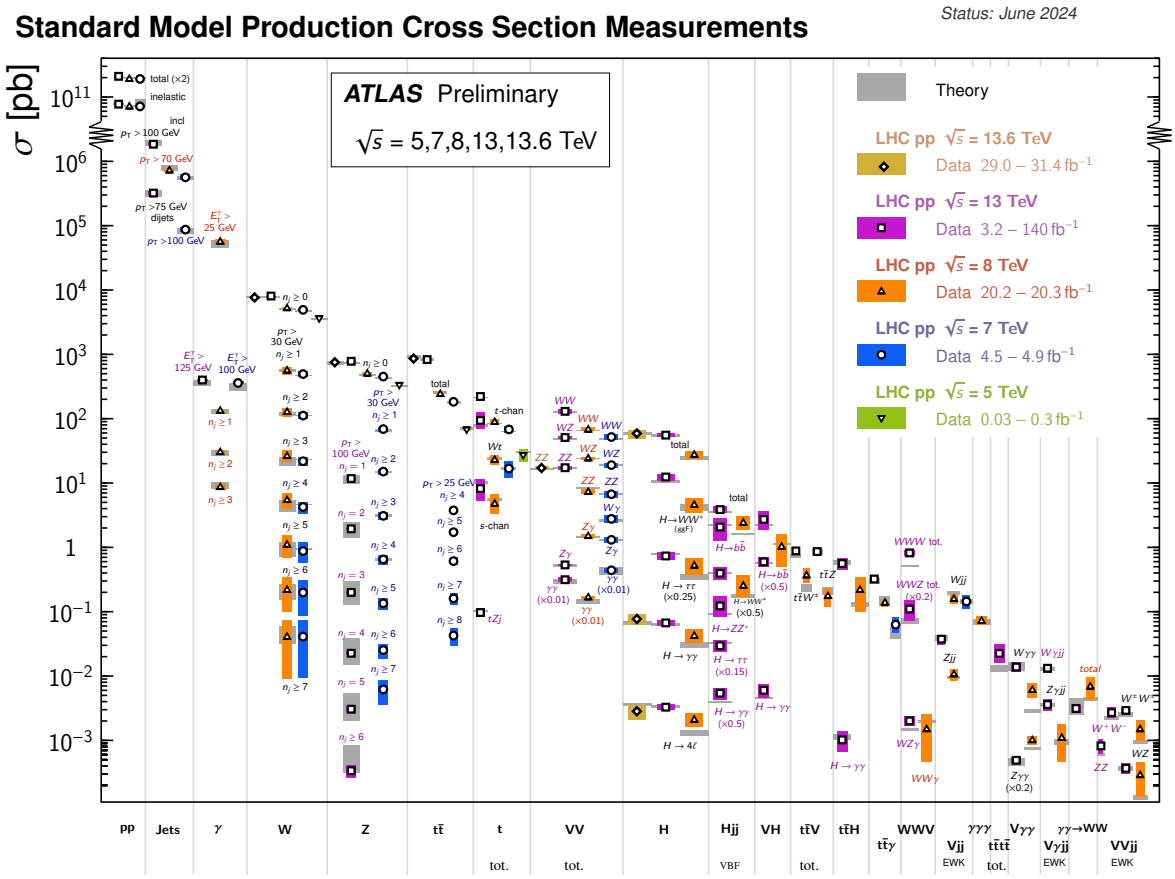

Figure 2.1. Summary of Standard Model production cross section measurements at the ATLAS detector for proton-proton collisions at different centre-of-mass energies. Theoretical predictions are also shown. Figure taken from Ref. [24].

However despite its success, it has several notable limitations and open questions which cannot be explained by the SM in its current setup.

Gravity is the only fundamental force not described by the SM. Attempts to unify gravity with other fundamental forces have been theorised, such as quantum loop gravity [25] or string theory [26], but have not been successful yet.

Astrophysical observations such as the rotation curves of spiral galaxies or gravitational lensing effects [27, 28] indicate that only 5% of the observable Universe is accounted for by the SM. The remainder is made up of dark matter (27%) and dark energy (68%).

Dark matter is theorised to interact only very weakly to SM particles. There is no candidate particle in the SM, other than neutrinos which are not abundant enough to

explain current cosmological observations.

The **baryon asymmetry** in the universe where the universe is dominated by matter over antimatter is also unexplained by the SM. The imbalance could be explained by the Sakharov conditions [29] which require baryon number violating process, departure from Thermal Equilibrium, to prevent matter and antimatter annihilating and lastly charge-parity (CP) violation. In QCD and QED processes CP is conserved but it can be violated in weak interactions. CP violation has been observed in the mixing of neutral B mesons [30] and in the decay of Kaon [31] and B mesons [32]. However, these observations are too small to explain the baryon asymmetry.

Today, it is believed that the SM is a low-energy limit of a more fundamental theory and that new processes, potentially involving new particles, will be discovered at higher energies. It is anticipated that Physics beyond the SM will unify all fundamental forces of nature and offer explanations for the incomplete components of SM.

2.2 Effective Field Theory

New Physics at high energy scales could have small effects noticeable at lower energies which are accessible experimentally. These small effects can be quantified in a model independent framework such as the *Effective Field Theory* of the SM (SMEFT). The main principle of SMEFT is that the SM is an approximation which holds true at energies on the electroweak scale. It introduces higher dimensional operators to capture New Physics effects which may appear on higher energy scales, such as the TeV or Planck scale, extending the SM. A low energy theory can integrate out particles to obtain effective vertices when below the energy scale of the propagator. A classic example is the use of Fermi Theory as an effective theory of the weak interactions, where below the energy scale of the W boson mass, the boson can be integrated out to obtain an effective point-like interaction [15]. Experimentally, such effects can be captured in the high energy tails of observed kinematic distributions in bounds of current experimental energies. A schematic of such an effect is shown in Figure 2.2.

The SMEFT Lagrangian is written as the Lagrangian of the SM plus higher dimensions

$$\mathscr{L}_{\text{EFT}} = \mathscr{L}_{\text{SM}} + \mathscr{L}^{(6)} + \mathscr{L}^{(8)} + ... \tag{2.20}$$

In Equation 2.20, only even dimensions are considered. Odd dimensions do not appear in the SMEFT due to violation of baryon and lepton conservation [33, 34]. The higher dimensional Lagrangians are defined as

$$\mathscr{L}^{(d)} = \sum_{i=1} \frac{c_i^d}{\Lambda^{d-4}} \mathscr{O}_i^d \quad \text{for} \quad d > 4, \tag{2.21}$$

where $\mathcal{O}_i^d$ are higher dimensional operators constructed from SM fields. The Wilson coefficients, c_i, scale the coupling strengths of a given operator of dimension d. The operators are suppressed by powers of the energy scale, Λ^{d-4}, at which New Physics may appear. The operators are invariant under the gauge symmetries of the SM. In the limit of $\Lambda \to \infty$ the additional EFT operators are completely suppressed and the SM Lagrangian is then restored. The SMEFT is formalised in the Warsaw basis, described further in Ref. [35]. The dimension 6 has 2499 baryon conserving operators predicted in the SMEFT [36]. In dimension 8, a total of 44,807 operators are predicted in SMEFT [37].

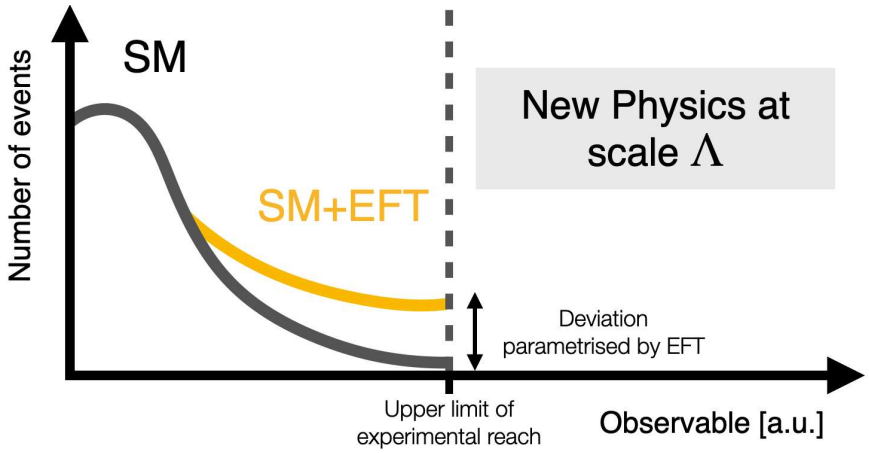

Figure 2.2. Schematic of how the low-energy effects of SMEFTs at the energy scale Λ can be parametrised by kinematic deviations from the Standard Model.

Experimentally, the sensitivity to SMEFT operators can be tested via gauge boson production processes at the LHC. Diboson production at the LHC has larger production cross sections than triple or quartic gauge couplings, as seen in Figure 2.1. However, the sensitivity of multiboson final states to EFT operators makes them interesting interactions to measure. In the context of multiboson interactions, dimension 6 is sensitive to both triple and quartic gauge couplings whereas dimension 8 is only sensitive to quartic gauge couplings. The larger suppression of $1/\Lambda^4$ in dimension 8 makes it more challenging to measure, so a process of high sensitivity is typically chosen, such as vector boson scattering.

2.3 Vector Boson Scattering at the LHC

A subset of particle interactions studied at the LHC are *Vector Boson Scattering* (VBS) processes. Such a process involves the scattering of two electroweak vector bosons ($V = \gamma, W^{\pm}, Z$) that are radiated from quarks from the proton-proton collisions. The two emitted bosons scatter off each other in a $VV \to VV$ interaction. This provides a

final state of two bosons and two quarks which will form jets, discussed further in Chapter 4. Figure 2.3 shows the diagram of this interaction. The emission of a photon or Z boson will not change the quark flavour, i.e the $q_1 = q_3$ and $q_2 = q_4$ in the diagram shown in Figure 2.3. However the emission of a $W^{\pm}$ boson will always lead to a change in the quark flavour as the weak interaction is governed by the CKM matrix and therefore will change in flavour eigenstates, for example $q_1 = u$ and $q_3 = d$. Many VBS interactions have been observed today at the LHC and the ATLAS experiment, where the cross sections measured can be found in Figure 2.1.

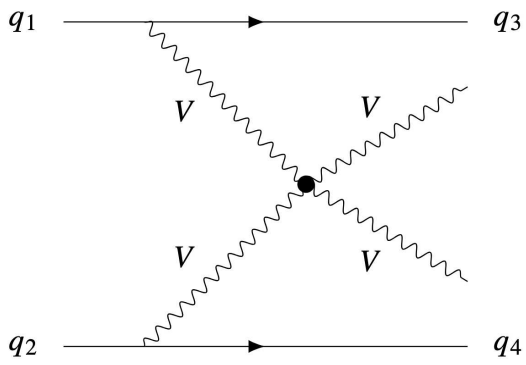

Figure 2.3. Feynman diagram of a vector boson scattering process where electroweak bosons can be emitted from quarks which scatter off each other.

Another VBS process which can also be studied at the LHC is one where photons are emitted by protons which are scattered and do not break up. As the bosons are emitted from the protons rather than the quarks, only massless and electrically neutral bosons can be emitted such as photons. This leads to so-called *photon-induced processes*.

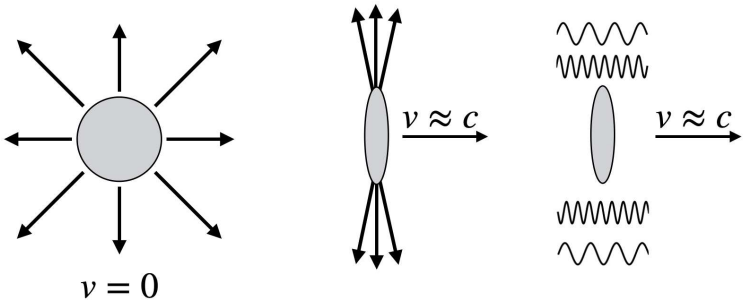

Figure 2.4. Diagram showing the occurance of relativistic proton producing coherent quasi-real photons. Schematic recreated from Ref. [38]

The emission of photons from the protons during elastic collisions is due to equivalent photon fluxes from the electromagnetic field of ultra-relativistic protons. A schematic of the emission of photons can be seen in Figure 2.4. The initial concept of electromagnetic fields being composed of photons was first proposed by Fermi [39]. The idea was extended to the relativistic case by Weizsäcker [40] and Williams [41]. When protons are at relativistic speeds such as that at the LHC, the electromagnetic field is deformed. It

is modified such that it is transverse to the direction of the Lorentz boost of the protons. As a result the electromagnetic field can be treated as a source of coherent quasi-real, high energy photons which travel parallel to the protons. At the LHC, protons interact via a peripheral collision where the photons collide, resulting in photon-induced VBS processes. The diagram of such a process is shown in Figure 2.5 where the final state can be $VV = \gamma\gamma, ZZ, W^{\pm}W^{\mp}$. The final state of W bosons will be studied in this thesis.

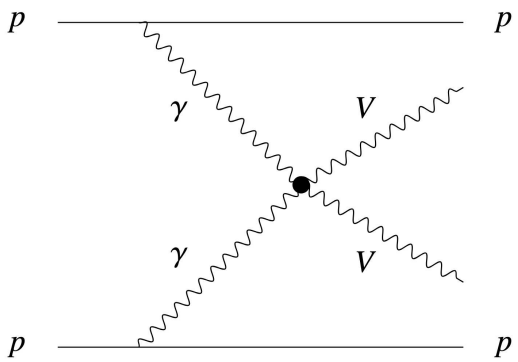

Figure 2.5. Feynman diagram of a photon-induced vector boson scattering process where photons are emitted from the protons.

The aforementioned VBS processes all have sensitivity to anomalous quartic gauge couplings which in dimension 8 of the SMEFT model are typically suppressed by $1/\Lambda^4$. A list of VBS processes which have been measured at the ATLAS experiment with a centre of mass energy of $\sqrt{s} = 13$ TeV are shown and discussed briefly below. These measurements are highlighted as they also studied the possible deviations from the SM due to the dimension 8 SMEFT operators modifying the quartic couplings of the bosons.

- Same Sign WW: Two W bosons are produced with the same electrical charge. The scattering is as follows, $W^{\pm}W^{\pm} \to W^{\pm}W^{\pm}$. The measurement made in Ref [42] is performed in the channel where both W bosons decay leptonically. The reported cross section found is in agreement with the SM.

- $WZjj$: This measurement is performed in the channel where both bosons decay leptonically. Similarly scattering is as follows, $W^{\pm}Z \to W^{\pm}Z$. The cross section measurement found agrees with the SM [43].

- $Z\gamma jj$: This measurement is found via the decay of the Z boson into neutrinos and the associated photon in the scattering. The VBS scattering is via $Z\gamma \to Z\gamma$. This vertex is not allowed in the SM as it is a neutral gauge interaction. Cross section found is consistent with the standard model [44].

- $W\gamma jj$: The process looks at the scattering of the W boson and a photon in a $W^{\pm}\gamma \to W^{\pm}\gamma$ interaction. The search is made in the leptonic decay channel of the W boson and is also in agreement with the SM [45].

In this thesis the $\gamma\gamma \to WW$ process will be explored. The fully leptonic final state was observed at the ATLAS experiment [46] however no measurements were made on the sensitivity to EFT operators via anomalous gauge couplings. This thesis will explore the sensitivity to New Physics via the semileptonic channel where the production cross sections will be larger. In contrast to the previously mentioned searches, this process has the advantage that the SM predicts it to have both triple and quartic couplings between the photons and W bosons. Therefore it has sensitivity to both the dimension 6 and dimension 8 operators. Additionally the emission of the photons from protons rather than quarks provides the experimental upper hand that the proton information can be used to measure the energy of the final state. This is experimentally performed with the use of forward detectors, discussed in Chapter 3.3. Moreover, due to the protons not breaking up, the process is a pure QED interaction and therefore will not be dominated by theoretical uncertainties from QCD. Thus, it is an interesting channel to measure sensitivity to New Physics, with many advantages.

CHAPTER 3

THE LHC, ATLAS & AFP

The Large Hadron Collider (LHC) [47] is a circular particle accelerator located at CERN[1] in Geneva, Switzerland. It sits underground in the tunnel of its predecessor accelerator, the LEP[2] collider. Both protons and lead particles can be collided at the LHC. The outcome of such collisions are reconstructed by particle detectors. Two general purpose particle detectors on the LHC ring are the ATLAS[3] [48] experiment and the CMS[4] experiment [49]. Both are constructed from specialised subdetector technologies to collect data from the particle collisions delivered by the LHC.

Additionally, the general purpose detectors have smaller detectors located around 200 m away from the interaction point (IP) which are highly specialised to measure very forward particles such as scattered protons, which are of interest in this thesis. The forward proton detector associated with the ATLAS experiment is the ATLAS Forward Proton Spectrometer (AFP) [50] and for CMS is the PPS[5] experiment [51]. Forward detectors can reconstruct protons which scatter at very small angles with respect to the LHC beam. These detectors aid the search of diffractive processes at the LHC such as photon-induced processes, as previously introduced in Section 2.3.

This chapter will provide a summary of the LHC in Section 3.1 describing how it provides particle collisions which take place at the experiments. This thesis uses data collected by the ATLAS experiment during proton collisions thus an overview of the detector and its trigger system will be summarised in Section 3.2. Section 3.3 will describe the AFP detector which is taken advantage of for the measurements made in this thesis.

[1] Conseil Européen pour la Recherche Nucléaire (European Council for Nuclear Research)
[2] Large Electron Positron
[3] A Toroidal LHC ApparatuS
[4] Compact Muon Solenoid
[5] Precision Proton Spectrometer

3.1 The Large Hadron Collider

The LHC collider is of circumference 26.7 km and sits in a tunnel located between 40 to 170 metres below the surface. The circular accelerator uses superconducting radio frequency cavities to accelerate the charged particles (protons or lead particles) to very high energies via two counter rotating beams [47]. For this thesis, only collisions of protons will be studied and discussion of lead collisions at the LHC are omitted.

The bunches form each beam which is guided around the ring by electromagnets such as dipoles, quadrapoles and higher order multipoles. The magnets also focus the beams, which increases the intensity of the colliding particles. The two beams share the same mechanical structure and cooling system. The LHC provides the beams with a revolution frequency of over 10,000 Hz. The two beams intersect at set locations on the ring where the protons collisions will occur. Collisions are separated by 25 ns in time, resulting in a collision frequency of 40 MHz.

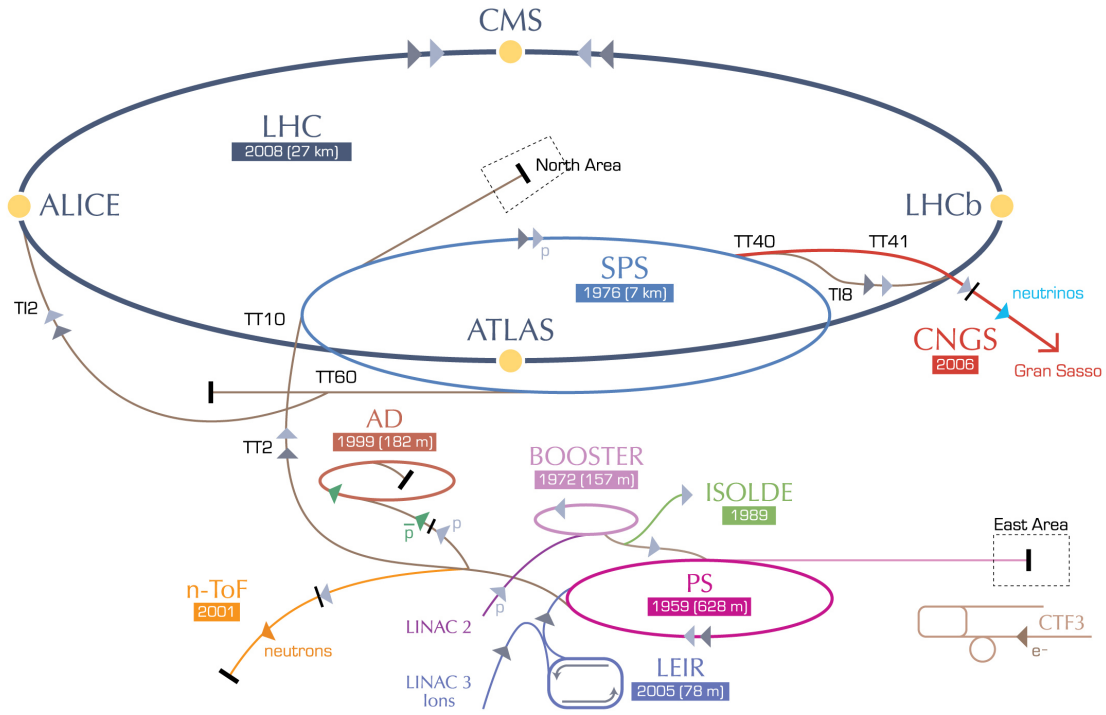

Figure 3.1. Schematic of the CERN accelerator complex. Protons are accelerated in a linear accelerator (LINAC2) then injected into a series of circular colliders, first the Proton Synchrotron Booster (PSB) followed by the the Proton Synchrotron (PS) and lastly the Super Proton Synchrotron (SPS) before entering the LHC. The image is modified from Ref. [52].

To obtain the 2808 bunches in the beam for which the LHC is designed to hold, a series of accelerators are used to fill the proton bunches into the LHC ring, shown in Figure 3.1. Since 2009, the LHC has provided proton-proton collisions of varying centre of mass energies, $\sqrt{s} = 7$ TeV, $\sqrt{s} = 8$ TeV, $\sqrt{s} = 13$ TeV and recently at $\sqrt{s} = 13.6$ TeV. The design centre of mass energy of $\sqrt{s} = 14$ TeV is projected to be achieved in future upgrades of the LHC [53]. This thesis will make use of the data collected during Run 2 of the LHC where $\sqrt{s} = 13$ TeV. The amount of collisions possible at a particle collider is defined by the *instantaneous luminosity*, $\mathcal{L}$. It is defined as,

$$\mathcal{L} = \frac{f n_b N_1 N_2}{4\pi\sigma_x\sigma_y} \tag{3.1}$$

with a revolution frequency, f, number of bunches n_b, number of particles N_1 and N_2 in each beam and the spread of the beam σ_x and σ_y [54]. During the Run 2 data-taking period, the LHC surpassed its design instantaneous luminosity, reaching $\mathcal{L} = 2.1 \times 10^{34}$ cm^{-2} s^{-1} in 2017 [55]. The instantaneous luminosity can be scaled by the cross section of a given particle process, σ, to obtain the number of events produced in a given time interval, dt, for the process such that $\frac{\mathrm{d}N}{\mathrm{d}t} = \mathcal{L} \times \sigma$. The *integrated luminosity* is expressed as $L_{\text{int}} = \int \mathcal{L}\mathrm{d}t$, which represents the quantity of data recorded. The full ATLAS Run 2 dataset corresponds to $L_{\text{int}} = 140$ fb^{-1} [6] between 2015 and 2018.

3.2 The ATLAS Detector

The ATLAS detector is structured in layers of subdetectors around the collision point, each specialised to provide different information about particles produced during particle collisions. From the innermost to outermost subdetector, ATLAS is composed of an inner detector surrounded by a thin superconducting solenoid, electromagnetic and hadronic calorimeters and a muon spectrometer. The exact layout of the ATLAS detector components is shown in Figure 3.2. The muon spectrometer has large superconducting air-core toroidal magnets. The detector is therefore submerged within a magnetic field, which aids the identification and detection of charged particles. Section 3.2.1 will define the coordinate system of the ATLAS detector followed by descriptions of the subdetector hardware, in Sections 3.2.2 - 3.2.4. Due to the high luminosity of the LHC, the ATLAS detector requires a robust and efficient trigger system with specialised firmware to handle the large collision rate, described further in Section 3.2.5.

[6] The unit barn (b) corresponds to 10^{-28} m^2

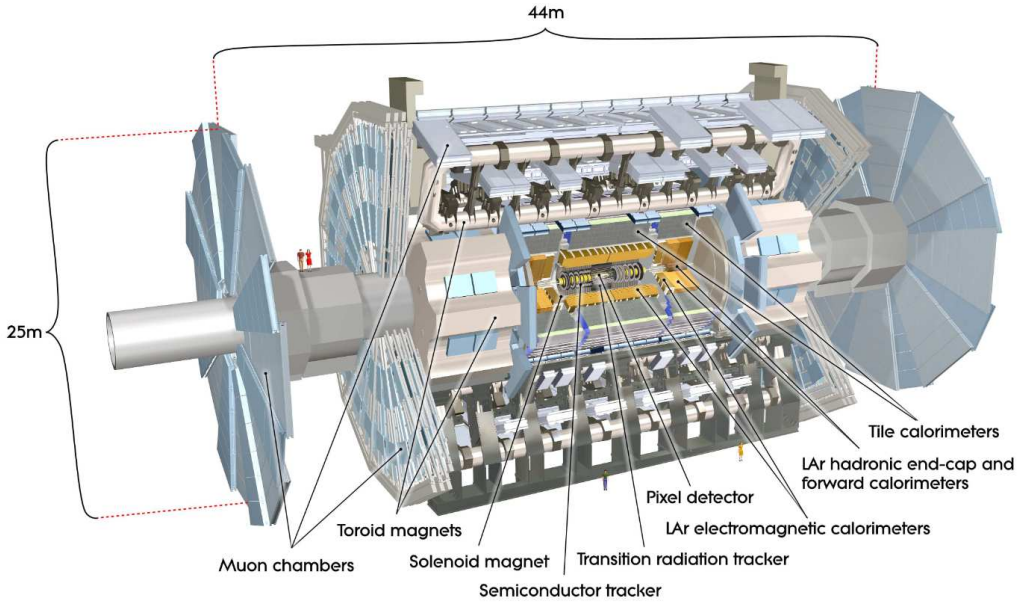

Figure 3.2. Overview of the ATLAS detector, with its subdetectors labelled in the schematic. Taken from Ref. [56]

3.2.1 Coordinate System

A right-handed coordinate system is used in the ATLAS experiment, with the origin at the nominal interaction point (IP) in the detector. The z-axis coincides with the axis of the beam pipe, the x-axis points from the interaction point to the centre of the LHC ring and the y-axis points upwards. Transverse kinematics are defined as the xy-plane, for example, transverse momentum (p_{T}) and missing transverse energy ($E_{\mathrm{T}}^{\mathrm{miss}}$). The azimuthal angle φ is the angle of the transverse plane with respect to the positive x-axis. The polar angle θ is the transverse plane with respect to the positive z-axis. The polar angle is more often expressed as the pseudorapidity, η, where η = -ln [tan(θ/2)]. In the ultrarelativistic limit, the pseudorapidity approaches the rapidity, y, where $y = \frac{1}{2}\ln\left[(E + p_z)/(E - p_z)\right]$ which is a Lorentz invariant quantity. The angular distance between two particles in the $\eta - \varphi$ plane is defined as $\Delta R = \sqrt{(\Delta\eta)^2 + (\Delta\varphi)^2}$.

3.2.2 Inner Detector

The *inner detector* (ID) is closest to the interaction point. It is designed to reconstruct large track density from particle collisions, providing kinematic information on charge, momentum and identification of charged particles. It is surrounded by a superconducting solenoid providing a 2 T axial magnetic field, shown in Figure 3.2, which bends the trajectories of charged particles due to the Lorentz force. The direction of the curvature indicates the particle charge, and the radius is proportional to the particle momentum. Information about the tracks allows the reconstruction of collision vertices, of particular interest are primary and secondary vertices. This is important in physics searches as it

can be used to distinguish vertices of interest from pileup, and additionally to identify secondary vertices of longer-lived particles, which is essential in identifications of the particles.

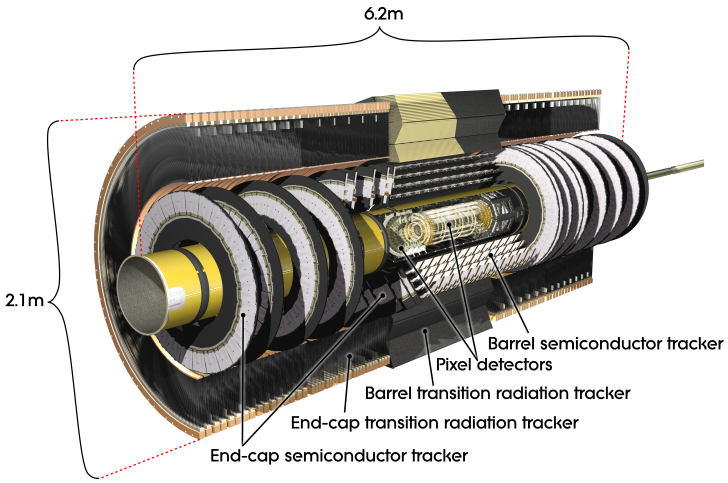

Figure 3.3. Schematic of the ATLAS Inner Detector and its subcomponents labelled. Figure taken from Ref. [57].

Three main components make up the inner detector: the *pixel* detector, the *silicon microstrip tracker* (SCT), and the *transition radiation tracker* (TRT). Together the inner detector covers the phase space of $|\eta| < 2.5$. As shown in Figure 3.3 the inner detector consists of a barrel region around the beamline and end-caps which sit in the transverse plane.

The pixel detector [58] is the detector closest to the interaction point providing high spatial precision reconstruction of the tracks. The innermost layer is the Insertable B-Layer (IBL) [59], located just 3.3 cm away from the interaction point. This is achieved with small silicon pixels of nominal size 50×400 µm^2 and reduced to 50×250 µm^2, for the innermost IBL layer. The SCT [60] is located outside of the Pixel Detector providing good resolution for the momentum reconstruction using silicon strip detectors. In the barrel, the strips run parallel to the beam. Additionally, strips are placed with an angle of 40 mrad allowing in combination measurements in $R - \varphi$ to precision of 17 µm and a z precision of 580 µm. The TRT [61] is the outermost layer constructed from straw tubes filled with a xenon gas mixture. The tubes have a diameter of 4 mm which in turn provides a $R - \varphi$ resolution of 130 µm. In the barrel region, the straws of length 144 cm, run parallel to the beam pipe, whereas in the endcap region the straws run radially. Electron identification can be performed within the TRT due to the detection of photons within the straw tubes. They are produced by the interaction of the electrons with the transition radiation material. The combination of the different subcomponents of the ATLAS inner detector successfully measured a relative momentum resolution of

the tracks of

$$\frac{\sigma_{p_{\mathrm{T}}}}{p_{\mathrm{T}}} = (4.83 \pm 0.16) \times 10^{-4}\ \mathrm{GeV}^{-1} \times p_{\mathrm{T}} \tag{3.2}$$

at the ATLAS detector. The measurement was performed with cosmic rays and achieved the design requirements, explained further in Ref. [62].

3.2.3 Electromagnetic and Hadronic Calorimeters

Measurements of particle energies are performed by the calorimeters of the ATLAS detector. Sampling calorimeters are constructed from alternating dense absorber materials and active materials. The incoming particles from the interaction point create *particle showers* upon interaction with the absorber materials. The particle showers occur via electromagnetic (electron-positron pair production and bremsstrahlung) and strong interactions. The consequently produced shower particles create signals in the active material through ionisation or scintillation which are read out by electronics.

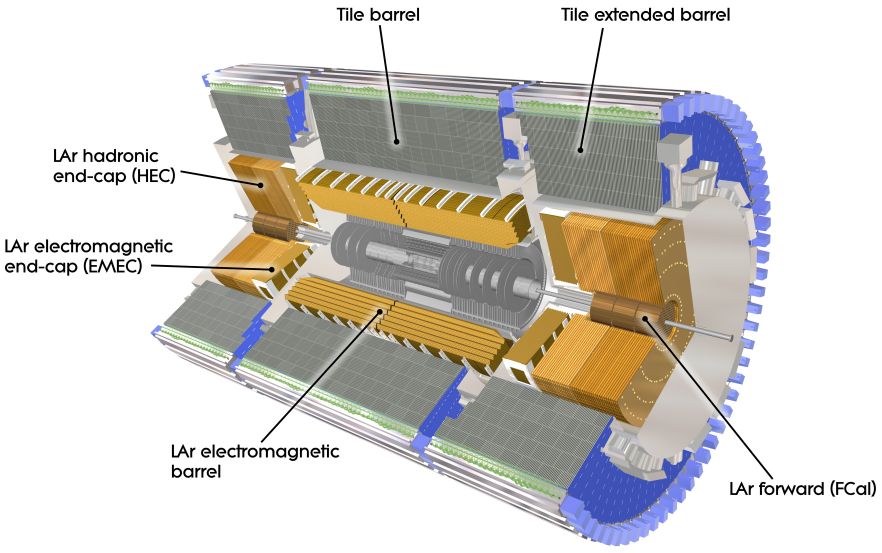

Figure 3.4. Cut-away view of the ATLAS calorimeter system. Labelled are the components of the Liquid Argon and Tile calorimeters. Figure taken from Ref. [63].

The ATLAS detector has two groups of sampling calorimeters: *Liquid Argon* (LAr) [64] and *Tile* [65]. The entire calorimeter system covers the range of $|\eta| < 4.9$. A schematic of the ATLAS calorimeter is shown in Figure 3.4 where the different calorimeter components are shown. The electromagnetic calorimeter (ECAL) has a depth of at least 22 radiation lengths (X_0) and the hadronic calorimeter (HCAL) uses material of depth 11 interaction lengths (λ) around $|\eta| = 0$. This containment of hadrons aids shielding of the muon spectrometer from high energy particle showers[7]. The shape of particle

[7] Although good shielding is provided, there are cases of very heavy hadron showers which overflow

showers indicate the nature of the particle interaction, where wide showers are hadronic and narrower are typically electromagnetic.

Electromagnetic Calorimeter

The LAr calorimeter is located outside of the ATLAS ID and is predominantly an electromagnetic calorimeter, designed to fully absorb electrons, positrons and photons. It uses either tungsten, copper or lead as the absorber material, depending on the component of the LAr detector. Liquid argon is used as the active material due to its radiation hardness and stable response. In order to maintain the argon as a liquid, it is cooled to -184 °C. The accordion-like structure of the absorber material and electrodes allows for full φ coverage. The LAr *electromagnetic barrel* (EMB) is constructed from two cylinders of length 3.2 m and thickness 53 cm which are separated by 4 mm. It covers the region of $|\eta| < 1.475$. The LAr *electromagnetic end-cap* (EMEC) covers the region of $1.375 < |\eta| < 3.2$, where it overlaps with the EMB, located on both sides of the detector. The region up to $|\eta| < 2.5$ is constructed of three layers of varying granularity in η and φ. The first layer has the finest segmentation (0.025×0.0245 in $\eta \times \varphi$) and can differentiate between electromagnetic showers induced by a single photon and those induced by the decay of a $\pi^0 \to \gamma\gamma$ decay. The second layer is where most electromagnetic showers deposit the majority of their energy. The third and most coarse layer is sensitive to energy leakage beyond the ECAL. Within $|\eta| < 1.8$, an additional thin layer of LAr and electrodes are present, called the presampler, which measures energy loss due to dead material in front of the ECAL. The presampler is present in both the EMB and EMEC. The design energy resolution of the EMB and EMC is achieved at the level of $\frac{\sigma_E}{E} = 10 \otimes 1.7\%$ [66].

Hadronic Calorimeter

The hadronic Tile calorimeter, in the barrel region is constructed with steel for the absorbing material and scintillating tiles as the active component. The higher density material allows for strong interactions of particles which passed through the ECAL, producing hadronic showers. The larger size of the Tile calorimeter with an inner radius of 2.28 m and a total extension of 4.25 m can contain the high energy showers. Particles traversing the tiles create scintillation light in the polystyrene material, which is converted from the ultraviolet spectrum to visible light via a wave length shifter and finally read out by photomultipliers. The *Tile Barrel* covers the region of $|\eta| < 1.0$ and the *Tile Extended Barrel* covers the region of $0.8 < |\eta| < 1.7$. The HCAL is coarser with modules of granularity 0.1×0.1 in $\eta \times \varphi$ space. The two LAr *Hadronic end-caps* (HEC) overlap the

into the muon system known as “calorimeter punch through”.

Tile barrel region and Forward Calorimeter, covering the region of $1.5 < |\eta| < 3.2$. This provides a smooth transition between the subcomponents of the calorimeter. The HEC has LAr for the active medium and copper plates as the absorbing material, chosen due to its radiation hardness. The energy resolutions of the Tile Calorimeter and the HEC were measured for pions as

$$\left(\frac{\sigma_E}{E}\right)_{\text{Tile}} = \frac{52.7\%}{\sqrt{E}} \oplus 5.7\% \quad \text{and} \quad \left(\frac{\sigma_E}{E}\right)_{\text{HEC}} = \frac{70.6\%}{\sqrt{E}} \oplus 5.8\%, \tag{3.3}$$

explained further in Ref. [65] and Ref. [48].

Forward Calorimeter

The Forward Calorimeter (FCAL) covers the most forward region in the calorimeter, corresponding to the region of $3.1 < |\eta| < 4.9$. As it is the only calorimeter in this region, the FCAL is constructed of an ECAL layer and two HCAL layers. The ECAL uses copper as the absorber material and the HCAL layers use tungsten. All layers use LAr as the active material. The LAr FCAL is recessed by 1.2 m with respect to the ECAL to reduce the quantity of neutron back scatter in the inner detector cavity.

3.2.4 Muon Spectrometer

The outmost layer of the ATLAS detector is the Muon Spectrometer (MS). Muons are minimally ionising at the high energies of the LHC and therefore can easily pass through the calorimeter system. Such muons can be produced both at the interaction point of the ATLAS detector and during hadronic showers. Therefore, a dedicated detector is required to reconstruct muons. The MS is designed to provide a resolution of 3% for a wide range of p_{T} and up to 10% at $p_{\text{T}} \approx 1$ TeV [67].

The detector comprises of a barrel and two end-cap sectors which together covers the range of $|\eta| < 2.7$. Two sets of specialised air-core toroidal magnets provide additional bending of the particle trajectories, aiding the particle identification. The barrel toroid runs along the z-axis of the detector. The magnetic field is non-uniform, varying from 0.15 T to 2 T [68]. The endcap toroid is located before the endcap muon chambers which sit in the xy-plane of the detector, providing a 4 T magnetic field. The location of the magnets can also be seen in Figure 3.2. Four chamber technologies are used in the different regions of the MS, two high precision tracking chambers and two trigger chambers. The tracking chambers comprises of the *Monitor Drift Tubes* (MDT) and the *Cathode Strip Chambers* (CSC). The trigger chambers are the *Resistive Plate Chambers* (RPC) and *Thin Gap Chambers* (TGC).

The barrel region, $|\eta| < 1.05$, is equipped with MDTs and RPCs. The MDTs are constructed from pressurised drift tube chambers filled with Ar/CO_2 gas. Multiple layers of the drift tubes are used in the chamber, typically three. The RPCs are gaseous detectors which have a 2 mm gas gap between two parallel resistive bakelite plates. The trigger chambers in the RPC have a time resolution of 15 ns to 25 ns and the η and ϕ positions can be read out by the electronics. Therefore, providing input to allow for triggering in the ATLAS trigger system. The endcap regions ($1.05 < |\eta| < 2.7$) use TGCs to trigger on muons. The TGCs are multiwire proportional chambers which can tolerate the high rates of forward particles up to the region of $|\eta| = 2.4$. The MDT chambers are used for tracking in all layers of the endcap with the exception of the inner layer at $|\eta| > 2.0$. The CSCs are multiwire proportional chambers with segmented cathodes oriented parallel and orthogonal to the wires. The CSCs are placed in the innermost layer of the endcap which is optimised for higher particle rates.

3.2.5 The ATLAS Trigger System

The LHC provides proton-proton collisions at a rate of 40 MHz. Given an event recorded by the ATLAS experiment amounts to 1.5 MB, it is not feasible to store all the events. To reduce this high rate, a trigger system works in unison with the detector components, filtering events in real-time and determining which events are saved. These events are in permanent storage and used for physics measurements and searches. The ATLAS trigger system reduces the 40 MHz rate down to an average rate of 1 kHz. This is done via a two stage trigger system consisting of a *Level-1* (L1) and *High Level Trigger* (HLT).

The L1 trigger is a hardware-based system which takes detector level inputs to determine if the events are of interest. The L1 consists of four main components: *L1 Calorimeter* (L1Calo), *L1 Muon*, *L1 Topology* (L1Topo) and *Central Trigger Processor* (CTP). The L1Calo system takes energy measurements provided from the LAr calorimeters in order to determine if an event contains candidates for electrons, photons and τ particles. Different energy thresholds and isolation requirements are set for the various candidates which determines if the event is triggered at L1. Additionally, total missing energy can also be inferred at the stage of the L1Calo trigger system. Similarly to the L1Calo, the L1 Muon takes as input information from the ATLAS muon spectrometer. The data is transmitted from the readout of the RPCs and TGCs. Energy thresholds are also required to determine if muon candidates are present in the event. The L1Calo and L1 Muon systems receive topological information from the events, η and ϕ but does not apply any requirements on them. The topological information along with the energy information from both L1Calo and L1Muon are sent to the L1Topo where further requirements are set such as topological, angular and kinematic selections [69].

The last stage of the Level-1 trigger is the CTP. It takes all the inputs from the other L1 systems and makes the final trigger decision. This provides a signal called the *Level 1 Accept* (L1A), which is a logical OR of all trigger items activated. The firing of this signal notifies the data acquisition system to readout the detector level information from all the subsystems. The L1A signal must occur within 2.5 µs in order for the detector electronics to readout the data to disk [70].

After the L1A signal, the information from the L1 triggers are inputted into the second stage of the trigger system, the software-based HLT. The L1 provides the HLT with *Regions of Interest* (RoI). The RoIs highlight particle candidates in the event with coarse information on the kinematics such as η, ϕ and energy. For the missing energy triggers, the whole calorimeter energy values are used as input from the L1 system. The HLT also takes as input more granular information from the subdetector systems. The reconstruction sequence in the HLT first provides early rejection of events via a dedicated fast trigger algorithm. More precise and CPU-intensive algorithms are deployed to check if events pass the threshold required for different triggers. Raw data of events passing the HLT trigger are sent for permanent storage to the Tier-0 data centre [70]. Further processing of the raw data is required to convert the information into data formats that can be used for offline physics analysis.

3.3 The ATLAS Forward Proton Detector

The goal of the ATLAS Forward Proton (AFP) detector [50] is to measure momentum and scattering angle of protons. Protons emitted from the ATLAS central interactions which scatter at very large rapidities ($|\eta| \approx 10$) are measured by the AFP detector. During the L1A signal, kinematic information from the AFP detector is also read out alongside the other ATLAS subdetectors. The protons reconstructed in the AFP detector are known as *Forward Protons*. The detection of these protons is essential for many diffractive physics searches which can be found in Ref. [50]. For this thesis, the reconstruction of protons with the AFP aids the isolation of photon-induced processes shown in Figure 3.5. It is essential to infer if it came from the photon-induced process or a background process. A brief summary of the AFP detector will be presented in the following sections. The full reconstruction of protons will be discussed further in Chapter 4.

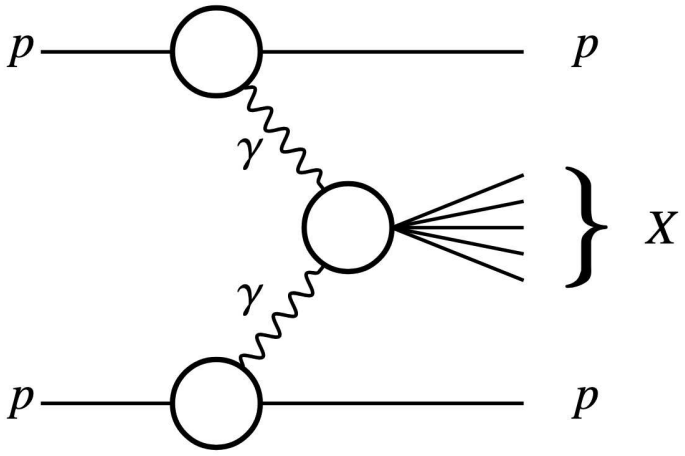

Figure 3.5. Schematic of a centrally exclusive photon-induced process, $pp \to p(\gamma\gamma \to X)p$, at the LHC. The forward scattered protons can be reconstructed with the AFP detector.

3.3.1 Detector Layout & Components

Protons scattered after an interaction in the ATLAS detector remain inside the beam pipe but are separate from the beam axis due to deflection from the LHC beamline elements. Using a *Roman Pot* (RP) system inserted into the beam pipe aperture, the protons can be intercepted and measured. The RPs are inserted once stable beams are achieved. The AFP detector is made up of four RP stations, with two located on each side of the ATLAS detector. The two "NEAR" stations are located at $z = \pm 205$ m and the two "FAR" stations are located at $z = \pm 217$ m from the ATLAS IP1. The choice of two stations per side allows for the p_{T} of the proton to also be measured, in addition to the fractional energy loss, ξ. A schematic overview of the AFP stations and the ATLAS coordinate system can be seen in Figure 3.6. All four stations compose of a *Silicon Tracker* (SiT) comprised of four silicon tracking planes which reconstruct the proton tracks in the x-axis relative to the beam axis. The two "FAR" stations additionally consist of a *Time-of-Flight* (ToF) detector using Cherenkov detectors to measure the timing information of the scattered proton and then reconstruct the proton interaction vertex along z-axis, in the ATLAS central detector.

The acceptance of the AFP detectors are influenced by the LHC beamline elements. The AFP stations are located after the LHC dipole magnets, marked as D1, D2 in Figure 3.6. This allows the protons to deflect into the acceptance of the detectors. Additionally, the collimators of the LHC marked as TCL4, 5 and 6 in Figure 3.6 remove the beam halo and prevent the magnet quenches. This changes the acceptance of the AFP detectors as it absorbs scattered particles, in particular scattered protons. Due to dependencies on the LHC beam elements, the acceptance is sensitive to the beam optics settings of the LHC. This is considered in the reconstruction via the Global Alignment, discussed further in Chapter 4.

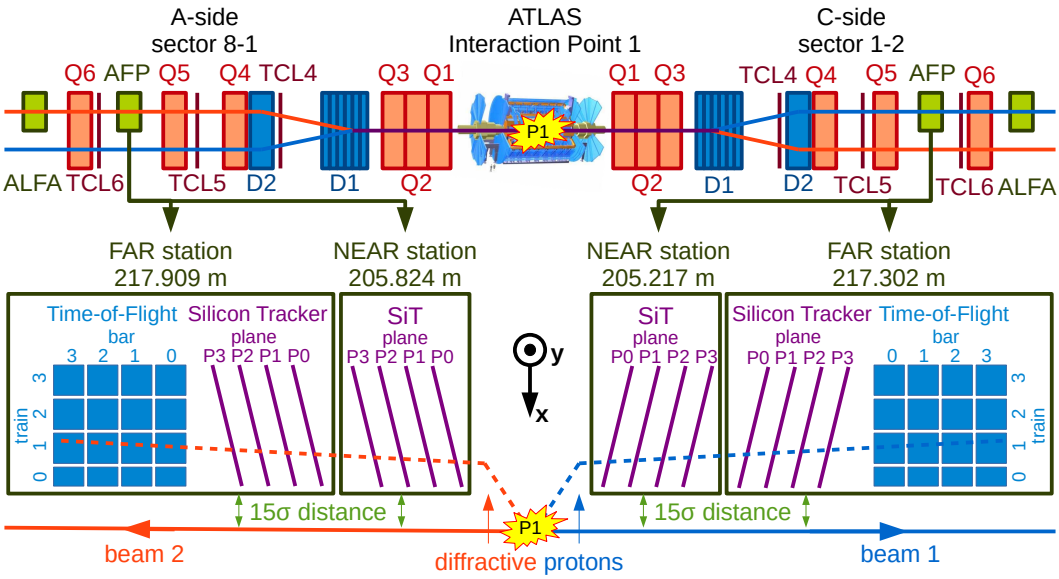

Figure 3.6. Schematic of the ATLAS Forward Proton (AFP) detector stations and their location relative to the ATLAS interaction point. The NEAR stations are located at roughly $z = \pm$ 205 m and the FAR stations roughly $z = \pm$217 m from IP. All four stations have 4 planes of silicon pixel trackers (SiT) while the outer stations have additional Cherenkov radiation time-of-flight (ToF) detectors. Figure taken from Ref. [71].

3.3.2 Silicon Tracker

The silicon tracker of the AFP detector provides the detection and kinematic measurement of forward protons which enter the tracker acceptance. In each station, the tracker is made of four pixel sensor layers which are 336×80 pixels, with pixels of size 50×250 µm^2 in the xy-plane, providing a total area of 1.68×2.00 cm^2. The planes have a depth of 230 µm in the z direction and have a distance of 9 mm between them. The silicon technology in the AFP tracker is similar to the pixel modules of the ATLAS IBL, which is based on 3D pixel sensors. This choice of sensor is motivated due to its radiation hardness. The radiation exposure is a major challenge for the AFP, as the detector located within a few mm distance of the beam. The pixel sensors are mounted onto a heat exchanger which can be seen in Figure 3.7. The planes are placed to have a small tilt of 14° about the y-axis in order to maximise the number of pixel hits. This improves the spatial resolution in the x-direction. The choice of pixels with a smaller size in x than y also aids the resolution as the protons are deflected in the y-direction due to the non-zero crossing angle θ_c at the interaction point of ATLAS. This provides a final resolution of 6×72 µm^2 in the xy-plane. Uncertainties in the alignment of planes, known as the local plane alignment, are considered in the reconstruction of the proton objects, and as a systematic. It is discussed further in the proton reconstruction in Chapter 4.

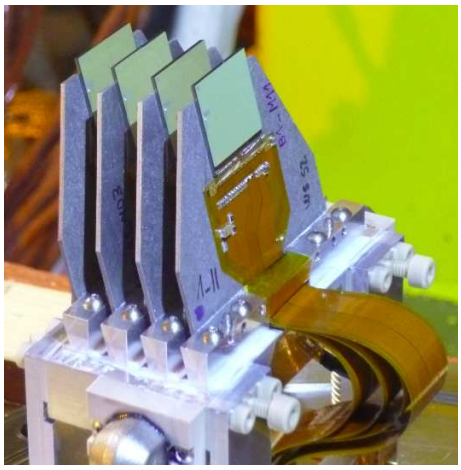

Figure 3.7. Photo of AFP SiT of a station. Pixel trackers are located on a heat exchange. Taken from Ref. [71].

3.3.3 Time-of-Flight Detector

The FAR stations have a time of flight detector which provides timing information which can be used to reject backgrounds. Protons which are detected have the time of arrival reconstructed. If a proton is detected in both A and C side FAR detectors, the interaction vertex position in the detector can be inferred as

$$z_{\text{vertex}} = \frac{c \cdot \Delta t}{2} = \frac{c \cdot (t_{\text{FAR,A}} - t_{\text{FAR,C}})}{2} \tag{3.4}$$

The position of the interaction vertex measured with the AFP ToF system can be compared to the vertex position determined by the ATLAS ID for a given event. If the same value is found then it can be said that the protons originated from the same event rather than pileup. This is very useful to understand if the forward protons are from the diffractive process such as the one shown in Figure 3.5. Timing information is reconstructed with the use of Cherenkov detectors made of L-shaped quartz bars. A photo of the ToF detector and a schematic of a single Cherenkov bar used in the detector is shown in Figure 3.8. The bars are arranged in a 4×4 layout, shown in Figure 3.8a. The Cherenkov light is produced by protons passing through the bars, which are detected by microchannel plate photomultiplier tubes (MCP-PMTs). As shown in Figure 3.8b, the short arm of the "L", known as the "radiator" arm, is the part exposed to the protons, and the longer arm is the "light-guide", which propagates the light to the PMTs. The radiator arms are positioned to be 48° with respect to the incoming beam to increase acceptance. The PMTs amplify the photo-electrons with a constant fraction discriminator (CFD) which are then inputted into the High-Performance Time-to-Digital converter (HPTDC). The signal is then sampled in 1024 bins which correspond to 25 ps, matching the interval between the LHC bunch crossings. For Run 2 of the LHC, the ToF detector was not in full operation due to inefficiency of the MCP-PMTs. Therefore forward protons reconstructed

in the data for this thesis are reconstructed only with the SiT trackers of the AFP stations.

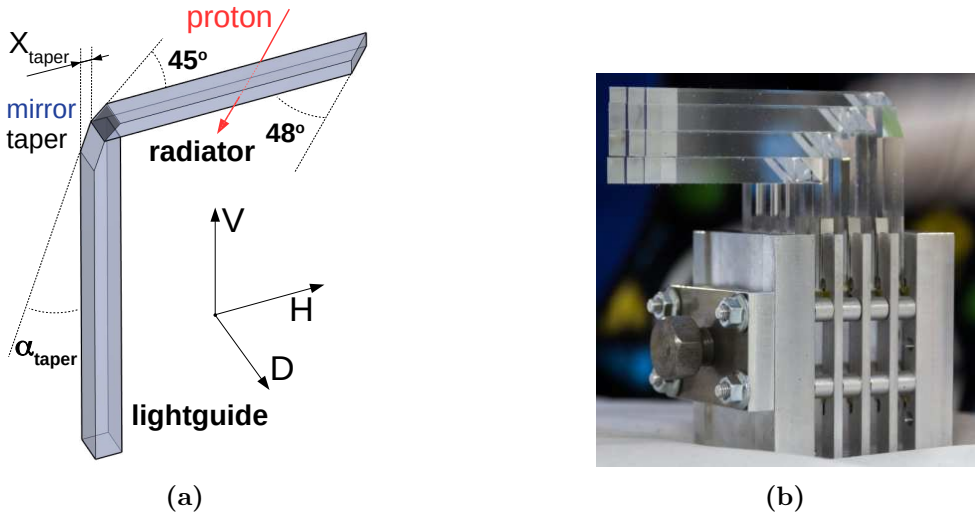

(a) (b)

Figure 3.8. Shown are (a) a schematic of the AFP ToF quartz Cherenkov LQ-bar, indicated the radiator and lightguide arms of the "L"-shaped bars and (b) photo of ToF showing the 4×4 layout used in the AFP stations. Both taken from Ref. [71].

CHAPTER 4

PARTICLE RECONSTRUCTION

The various particles produced during proton collisions at the LHC leave signatures in the subdetectors of the ATLAS and AFP detector. Signatures depend on properties of the respective particles. The tracks from the inner detector and energy recorded by calorimeters are inputs to various reconstruction algorithms of each particle type independently. Further isolations and identification criteria are applied in order to reject particles reconstructed which originate from other experimental sources. Corrections are applied to particles to compensate for subdetector inefficiencies which can skew the particle properties from its true kinematic properties.

This chapter will provide an overview of the particle reconstruction for objects of interest using the central ATLAS detector, covering jets in Section 4.1, electrons and photons in Section 4.2, muons in Section 4.3 and hadronically decaying tau leptons in Section 4.4. As the reconstruction algorithms are independent, overlap removals must be applied to reduce cases where the same detector signals are reconstructed as two different objects, described in Section 4.5. The very weakly interacting neutrinos are inferred from missing transverse momentum, discussed in more detail in Section 4.6. The longitudinal component of the neutrino momentum cannot be derived alone from missing longitudinal momentum as it is not conserved. Therefore with additional constrains applied, the longitudinal neutrino momentum is inferred using the methodology described in Section 4.7. The forward protons are reconstructed independent with the AFP detector, discussed in Section 4.8.

4.1 Jets

The quarks and gluons are bound by the strong force into colourless bound states via the process known as colour confinement during QCD- more details discussed in Section 2.1.

The baryons and mesons produced from the same quark or gluon form a so-called *jet*. A jet is defined as a cone structure produced initially by a quark and gluon containing all particles produced during its hadronisation. Various reconstruction algorithms are used to reconstruct the jets produced at the ATLAS experiment. The algorithms require as input, so-called *topological clusters (topoclusters)*. The topoclusters are formed from grouping the hits in calorimeter cells from the ATLAS ECAL. Seed cells are identified when with energy significantly above the noise threshold, typically around four standard deviations. The noise threshold is the baseline energy due to electronics noise and pileup [72]. Neighbouring cells with a significance greater than two standard deviations are also included in the cluster. Lastly, boundary conditions are applied to constrain the topocluster. All cells adjacent to the electromagnetic cells included in the cluster are summed to form the topological cluster. This topocluster provides position information in the η - ϕ plane. The topoclusters are then combined to form jets using the *anti-k_t* algorithm [73]. The algorithm is a modification of the sequential recombination algorithm k_t [74, 75] and the Cambridge/Aachen [76, 77]. Distances are measured between clusters i and j as

$$d_{ij} = \min(k_{t,i}^{-2}, k_{t,j}^{-2}) \frac{\Delta_{ij}^2}{R^2}, \tag{4.1}$$

$$d_{iB} = k_{t,i}^{-2}, \tag{4.2}$$

where $\Delta_{ij}^2 = (y_i - y_j)^2 + (\phi_i = \phi_j)^2$, $k_{t,i}$ is the transverse momentum, y_i the rapidity and ϕ_i the azimuthal angle of the cluster. The *radius parameter*, $R = \sqrt{\eta^2 + \phi^2}$, is assigned as $R = 0.4$ for small radius jets and $R = 1.0$ for large radius jets. The algorithm takes as input all reconstructed topoclusters and iteratively adds the two clusters with the smallest distance subject to Equation 4.1. Equation 4.2 is the stopping condition of the algorithm such that it terminates when all remaining clusters have distances larger than d_{iB}. The jets constructed at this stage are calibrated to the electromagnetic scale. Reconstructed tracks can also be input for the algorithm as only spatial and p_{T} information are required.

Jets can be reconstructed using information from both the topological clusters in the calorimeter with the *anti-k_t* algorithm and tracks of charged particles from the ATLAS Inner Detector. The use of track information aids the reconstruction efficiencies at low p_{T} as the ATLAS ID provides a higher resolution than the calorimeter. Additionally with the angular resolution of the tracks, the jets produced can be distinguished from pileup or hard scatter vertices. Further details of the reconstruction and calibrations for small radius and large radius jets are discussed in the following subsections.

4.1.1 Small Radius Jets ($R = 0.4$)

Reconstruction

The *Particle Flow (PFlow)* algorithm [78] aims to improve the energy resolution of the jets by using tracking information for the charged particles in hand with the calorimeter information for neutral particles produced during hadronisation. The tracks reconstructed with $p_{\mathrm{T}} > 400$ MeV, and associated to the hard scatter primary vertex[1], are selected. When extrapolating the tracks to the calorimeter, the tracks and topoclusters can be matched using both spatial and energy information. Tracks which are matched to a topocluster are subtracted from the calorimeter response from the cluster. This is essential to ensure the energy of the charged particle of the jet is not double counted as both a track and calorimeter signal. The remaining cluster is considered to originate from neutral components of the jet. Clusters without any matched tracks are also assumed to originate from neutral particles. The remaining neutral particles of the jet from the calorimeter and the charged particles from the inner detector are used as inputs into the *anti-*k_t algorithm with $R = 0.4$.

Jet Energy Scale (JES) Calibration

The jet energy scale (JES) calibration restores the reconstructed jet energy to that at the particle level. Figure 4.1 shows the full calibration chain applied to the reconstructed small radius jets where at each stage the jet kinematics are corrected.

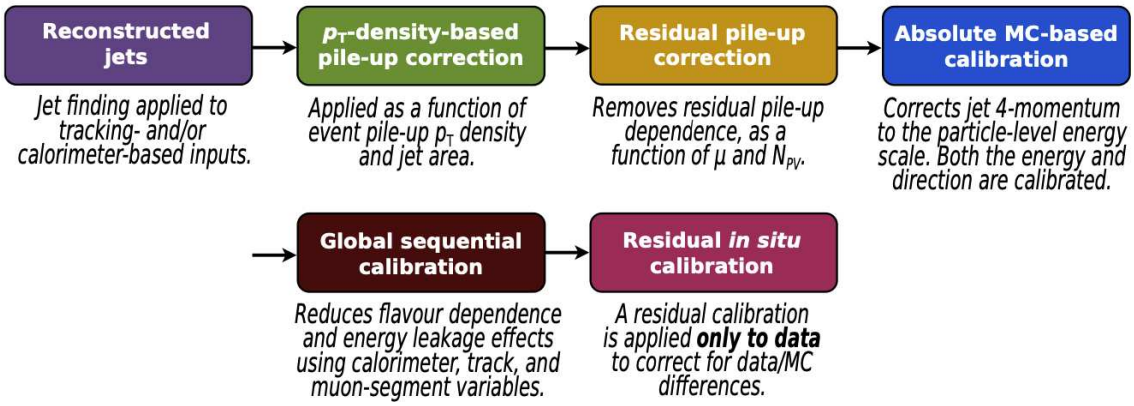

Figure 4.1. Calibration applied to reconstruct jets. For this thesis, this calibration chain is applied to the small radius jets of size $R = 0.4$. Diagram taken from Ref. [80]

The first corrections applied to the jets concern pileup mitigation. Interactions from the underlying event or neighbouring bunch crossings will produce signals in the calorimeter which are not from the hard scatter vertex. Two items must be considered to correct

[1]The primary vertex (PV) is defined as the interaction vertex with the largest sum of squares of associated track momenta. The vertex requires a minimum of two tracks with $p_{\mathrm{T}} > 500$ MeV which can be reconstructed to the beam spot of the proton-proton collision [79].

for pileup, the first is correcting the jet area (A) and the transverse momentum density of the pileup. Then a residual correction is applied to correct for the number of interactions per bunch crossing (μ) and the number of reconstructed primary vertices in the event (N_{PV}). Together the correction is $p_{\mathrm{T}}^{\mathrm{corr}} = p_{\mathrm{T}}^{\mathrm{reco}} - \rho A - \alpha(N_{\mathrm{PV}} - 1) - \beta\mu$, where ρ is the median pileup momentum density and values of α and β are derived from the fits of the jet response as a function of N_{PV} and μ respectively. The next stage of the calibration corrects the absolute energy scale and η calibration. This is determined during simulations where the jet energy response is defined as $R = E^{\mathrm{reco}}/E^{\mathrm{Truth}}$ and are derived in bins of truth η and energy. This accounts for energy loss due to the dead material and biases in the reconstructed jets. However, differences in the response can arise from other jet characteristics, such as the jet flavour. These are accounted for in the following calibration stage, the global sequential calibration. This stage improves the jet p_{T} resolution without changing the jet energy response. As a function of the detector parameters, such as number of tracks and calorimeter hits, corrections are made to the jet reconstruction [80]. This stage sequentially corrects various observables such as number of tracks, calorimeter energy distributions which had dependence on the jet flavour, and muon tracks to correct for punch-through of jets. The last stage of the jet calibration is the residual in-situ calibration. This is required due to the modelling of the detector and various processes in simulation not being perfect. The correction includes an η intercalibration where the p_{T} balance in dijets events are used to correct the energy scale of forward jets to that of central jets.

Jet Energy Resolution (JER)

The jet energy resolution is an essential parameter in jet reconstruction. The JER describing the transverse momentum can be parametrised by three parameters: a noise term, a stochastic term and a constant term. The noise term accounts for contributions of electronic noise to the signal measured by the detector front-end electronics, as well as that due to pileup. Statistical fluctuations in the amount of energy deposited are captured by the stochastic term. The constant term accounts for energy depositions in passive material such as the cryostats and solenoid coil, the origin of the hadron showers, and non-uniformities of response across the calorimeter. The JER is determined with using dijet events. The jets produced should be back-to-back if the resolution of the detector is perfect. Deviations to this are measured and quantified as the JER.

Jet Vertex Tagger (JVT)

In order to reduce the chance if jets originating from the pileup, the small radius jets used in this thesis are required to pass the jet vertex tagger (JVT) [81]. It is a likelihood discriminant that requires consideration of tracking information from the ATLAS ID to

identify if the jet originates from the the hard scatter vertex. The JVT is applied only to jets with $p_{\mathrm{T}} < 60$ GeV due to pileup only dominating at lower energies [81].

b-tagged Jets

Jets originating from the hadronisation of *b*-quarks, known as *b-jets* can be identified with specialised *b*-tagging algorithms. It is possible to distinguish these jets from lighter quarks due to the relatively long lifetime of *b*-hadrons produced in hadronisation. The heavy *b*-hadrons decay, displaced, within the inner detector volume. The tagging algorithm depends on the reconstruction of this secondary displaced vertex [82]. The mass and momentum are also used to separate these jets from *c*- or light-jets from *u*-, *d*-, *s*- quarks and gluons. The various algorithms are used as inputs into a Boosted Decision Tree (BDT) which evaluates how likely the jet is originating from a *b*-quark [83]. Working points are defined depending on the average efficiency of the jet. This thesis uses a medium working point [83] which corresponds to a 70% *b*-tagging efficiency.

4.1.2 Large Radius Jets ($R = 1.0$)

Reconstruction

Large radius jets are typically a multipronged structure depending on the origin particle decaying. The jets can contain multiple jets which are reconstructed as one large radius jet, for example a top quark decaying hadronically reconstructed as a three pronged jet. The decay products must be close in spatial proximity to be clustered together in the reconstruction and therefore are often boosted. Thus the reconstruction of large radius jets have a minimum transverse momenta of $p_{\mathrm{T}} > 200$ GeV. The reconstruction of large radius jets include taggers to verify how likely the large radius jet originated from a W boson, Z boson or t-quark. Different taggers can also include how likely the mass reconstructed matches the particle origin. The topological clusters are calibrated using a local cell re-weighting (LCW) scheme [72]. It is required to correct the energy scale as the topological clusters are calibrated only to the electromagnetic scale and need to be corrected for the hadronic component. The reweighting of a cell is as follows:

$$w_{\mathrm{cell}}^{\mathrm{cal}} = \mathscr{P}_{\mathrm{clus.}}^{\mathrm{EM}} \cdot w_{\mathrm{cell}}^{\mathrm{EM\text{-}cal}} + (1 - \mathscr{P}_{\mathrm{clus.}}^{\mathrm{EM}}) \cdot w_{\mathrm{cell}}^{\mathrm{HAD\text{-}cal}}. \tag{4.3}$$

The weights $w_{\mathrm{cell}}^{\mathrm{EM\text{-}cal}}$ and $w_{\mathrm{cell}}^{\mathrm{HAD\text{-}cal}}$ represent the factors applied by the EM or HAD calibration to the cell signal. The coefficients of the weights are the probability that a given topological cluster is generated by an electromagnetic shower, $\mathscr{P}_{\mathrm{clus.}}^{\mathrm{EM}}$. More details concerning the LCW can be found in Ref. [72]. The LCW clusters are then reconstructed as jets using the anti-k_t algorithm requiring $R = 1.0$.

Jet Energy & Mass Scale (JES & JMS) Calibration

Figure 4.2 provides a summary of the calibrations performed on large radius jets in order to correct for the true jet energy, as well as further mitigation of the pileup.

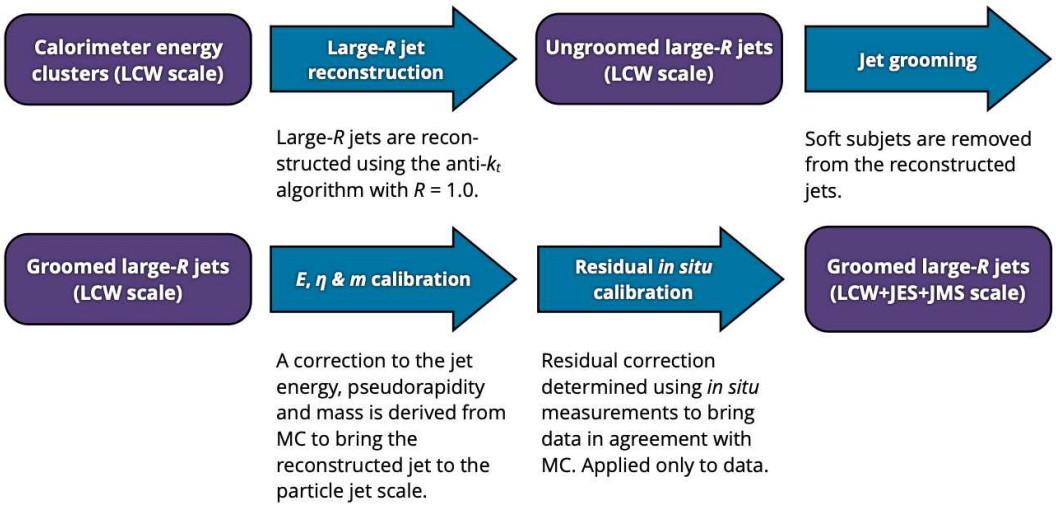

Figure 4.2. Calibration applied to reconstructed jets. For this thesis, this calibration chain is applied to the small radius jets where $R = 1.0$. Diagram taken from Ref. [84]

Jets reconstructed after the LCW reweighting are calibrated to the hadronic scale, also written as the LCW scale. These jets are labelled as *ungroomed jets*. The first stage in the calibration is known as jet grooming where soft subjet structures are removed from the reconstructed jets. The clusters within the jet are reclustered into subjets of radius $R = 0.2$. Subjets which have a small p_{T} with respect to the large radius jet are removed when $p_{\mathrm{T}}^{\mathrm{subjet}}/p_{\mathrm{T}}^{\mathrm{jet}} < 0.05$. This requirement removes contributions within the jet which originate from pileup, soft (low p_{T}) emissions and the underlying event. Following this stage, the groomed jets are calibrated to rescale the reconstructed jets to the particle jet scale. The energy and η response are calibrated using the difference between reconstructed and truth from simulations, similar to that performed for small radius jets. For large radius jets, an additional calibration is performed to correct the mass scale of the jets with the truth mass from simulations. The last stage of the calibration are the residual in-situ calibration to the JES and JMS. The JES follows the same procedure as previously discussed with the small radius jets, using dijet events. The JMS corrections are determined with $t\bar{t}$ events in the fully hadronic channel. The kinematic distributions are fitted to form mass peaks which originate from the high p_{T} decays of the top quarks. The top quark and W boson masses are fitted. A second calibration to the JMS is performed using the inner detector tracks and the calorimeter response. The ratio of $R_{\mathrm{trk}} = p_{\mathrm{T}}^{\mathrm{calo}}/p_{\mathrm{T}}^{\mathrm{track}}$ is compared on the reconstruction level and the truth level in simulations of $t\bar{t}$ events [84].

W Jet Taggers

Taggers are used to evaluate how likely the large radius jets are to originate from the hadronic decay of a W-boson , Z- boson or top quark decay. The taggers are implemented with deep neural networks which are trained individually to distinguish the origin of the jet. The training and testing datasets require various kinematic requirements unique for the W-tagger in order for the DNN to be performed on [85]. The tagger used for this thesis tags jets with a mass likely matching to that of the W boson with an 80% acceptance efficiency.

4.2 Electrons and Photons

Electrons and photons are reconstructed using information from both the ECAL and the inner detector. Electrons are expected to leave a signature in both the ID and ECAL whereas photons are expected to leave a signature in only the ECAL. Photons may be converted into an electron-positron before it reaches the calorimeter. This would produce a pair of tracks with a displaced conversion vertex in the ID. Electrons can lose energy due to bremsstrahlung when interacting with the detector material. The radiated photons can also convert into electron-positron pairs. Such interactions are all taken into consideration in the reconstruction of electrons and photons [86].

Clusters formed within the EM calorimeter aid the identification of electron candidates. The topoclusters are formed in a similar manner to that for the jets. However, as the electrons are typically softer than jets, the noise produced in the calorimeter may be reconstructed as an electron. Therefore, the innermost layer of the ECAL is not used to form clusters. Typically, bremsstrahlung of electrons are collimated in the direction of emission and are included in the same electromagnetic cluster as the electron candidate it originated from. Tracks are reconstructed from the hits in the various inner detector tracking layers. Iterative track fitting algorithms match and reconstruct the hits, taking into consideration the curvature due to the magnetic field.

Electron candidates are reconstructed by matching the clusters to ID tracks. If an electron radiates a photon via bremsstrahlung prior to entering the ID volume, multiple tracks may be matched to the same electromagnetic cluster, originating from the same primary electron. Such cases are resolved when checking which track and cluster are closest in ΔR and also has four hits in the SCT. The electron-track candidate is required to originate from the primary vertex. If a cluster cannot be matched to tracks, it is tagged as an unconverted photon. If a seed cluster is compatible with the production of an electron and positron pair and also is matched to a pair of tracks, the particle is tagged as a converted photon.

The reconstruction algorithms for electrons can still reconstruct hadronic jets which mimic the signatures of an electron. Removal of these contributions are done by applying electron identification requirements. Various quantities related to the electron are inputted into a likelihood discriminant which is used to identify electrons. Such quantities are the electron track, lateral and longitudinal development of the electromagnetic shower and the spatial compatibility of the electron-cluster candidate. More details can be found in Ref. [87]. Three identification working points are defined with increasing background rejection efficiencies: Loose, Medium and Tight. The working point used in this thesis is tight (labelled as TightLH) and is applied to reconstructed electrons.

Additionally, an isolation criteria is also applied in order to further reject backgrounds from heavy-flavour decays of light hadrons which are misidentified as electrons. There are two main isolation variables used, a calorimeter-based isolation ($E_{\mathrm{T}}^{\mathrm{cone20}}/p_{\mathrm{T}}$) and a track-based isolation ($p_{\mathrm{T}}^{\mathrm{varcone20}}/p_{\mathrm{T}}$). The calorimeter-based isolation sums the transverse energy deposited in calorimeter cells in a cone of size $\Delta R = 0.2$ around the electron, excluding the $\Delta\eta \times \Delta\phi = 0.125 \times 0.175$ around the barycentre of the electron [88]. Effects such as energy leakage from the electron shower into the isolation cone are considered, additionally pileup contributions. The track-based isolation similarly is the scalar sum of the transverse momentum of the tracks in a cone of $\Delta R = 0.2$ around the electron, excluding the track of the electron itself. The Tight isolation working point is used in this thesis where $E_{\mathrm{T}}^{\mathrm{cone20}}/p_{\mathrm{T}} < 0.06$ and $p_{\mathrm{T}}^{\mathrm{varcone20}}/p_{\mathrm{T}} < 0.06$ [88].

4.3 Muons

Muons are reconstructed via the matching of tracks between the ID and MS tracks. A simultaneous fit is performed on the track of the ID to the MS taking into account any energy losses in the calorimeter. Three additional requirements are applied to the identification of the muons; the χ^2 of the track fit, the difference in the transverse momentum measurements of the ID and MS, and the q/p significance and the difference in the ratio of charge and momentum in the ID and the MS. The medium identification working point is applied to muons in this thesis. The isolation of the muon is determined by the track- and calorimeter- based isolation variables previously defined where a Loose working point is used in this thesis [89].

4.4 Hadronic Taus

The reconstruction of tau leptons are essential as they have a large branching ratio for hadronic decay where some decays involve charged pions in the final state [90]. The decays have prongs depending on the number of charged pions. Tau candidates are

identified with topological calorimeter clusters reconstructed with the anti-k_t algorithm where $R = 0.4$. The tracks matched to the candidate are included if the track is within $R < 0.2$ of the lepton, once the lepton has already passed quality requirements. The choice of $R < 0.2$ is due to hadronic taus producing narrower jets than quarks or gluons. Therefore it also motivates the choice of discriminating on an isolation ring about the candidate of $0.2 < R < 0.4$ where the number of tracks in this region are considered in the reconstruction [90]. The reconstruction of their energy is considered in the construction of missing transverse momentum, which is a kinematic used in this thesis.

4.5 Overlap Removal

The reconstruction of the objects via calorimeter clusters and tracks are all performed independently. As a result, ambiguities arise from signatures where the same detector signal is used to reconstruct different objects, for example an electron and a hadronic jet. This can be due to a misidentification of one of these objects such that it is duplicated, or due to particles being produced in close vicinity, such that they are not well isolated and bias the reconstruction. Although efforts are made to reduce such mis-reconstruction in the algorithms and via isolation requirements, they are not completely immune. Therefore *overlap removal* of various reconstructed is completed in order to veto cases where such ambiguities cannot be resolved. This is done via the proximity of the different objects to one another in ΔR. These conditions applied for data collected during Run 2 of ATLAS, and therefore this thesis, are described.

Muons may be reconstructed as electrons due to emission of a photon via bremsstrahlung. The photon, or the electron-positron pair produced by the photon, will leave signatures in the electromagnetic calorimeter, in the same direction as the muon. Therefore electrons within $\Delta R(e, \mu) < 0.2$ are removed. Additionally electrons which share an ID track with the muon in the event are also removed. Electrons and muons are produced during heavy flavour decays of the jets can be reconstructed. Therefore electrons and muons within $0.2 < \Delta R(\text{jet}, e/\mu) < 0.4$ are removed.

Jets can be reconstructed when originating from a tau decay or a photon due to the same cluster hits being used. Therefore a jet is removed when $\Delta R(\text{jet}, \tau/\gamma) < 0.2$. Additionally, a jet may be reconstructed when a muon is present, due to the previously mentioned photon radiation of the muon. Therefore jets with fewer than three tracks in the ID and $\Delta R(\text{jet}, \mu) < 0.2$ are removed.

4.6 Missing Transverse Momentum

Weakly interacting particles such as neutrinos cannot be directly measured at the ATLAS experiment as they do not interact with any detector material. The presence of such particles can be inferred indirectly, by using the momentum conservation in the x - y plane. The transverse momentum must be conserved in a given event and therefore this constraint can be used to infer the transverse momentum of the invisible particles produced during the interaction. The negative sum of all particle energy reconstructed should equate to the sum of all invisible or missing particles produced during particle collisions. This is labelled as $E_{\mathrm{T}}^{\mathrm{miss}}$. The $E_{\mathrm{T}}^{\mathrm{miss}}$ is reconstructed from the energy of calibrated detector signals corresponding to muons, electrons, photons, hadronically decaying τ leptons, jets and a soft term [91]. The soft term considers signals which are not associated with reconstructed objects, due to originating from the underlying event or pileup. The missing transverse momentum is summed along the x and y axis such that:

$$E_{x(y)}^{\mathrm{miss}} = E_{x(y)}^{\mathrm{miss},\mu} + E_{x(y)}^{\mathrm{miss},e} + E_{x(y)}^{\mathrm{miss},\gamma} + E_{x(y)}^{\mathrm{miss},\tau} + E_{x(y)}^{\mathrm{miss,jets}} + E_{x(y)}^{\mathrm{miss,soft}}. \tag{4.4}$$

Each term in this equation is calculated as the negative vectorial sum of the transverse momenta of energy deposits or trajectories of charged particles. In order to avoid double counting of energy, only mutually exclusive objects are considered in the calculation of $E_{\mathrm{T}}^{\mathrm{miss}}$. Therefore the reconstructed objects are added into the formula in the order presented, from highest to lowest priority. Objects overlapping are selected based on this priority [91]. It then follows that $E_{\mathrm{T}}^{\mathrm{miss}} = \sqrt{(E_x^{\mathrm{miss}})^2 + (E_y^{\mathrm{miss}})^2}$. The soft term gives rise to the largest uncertainty in the reconstruction of missing transverse momentum as it is sensitive to noise of the detector.

4.7 Neutrino Longitudinal Momentum

One parameter required for this thesis is the mass of the WW system, m_{WW}. The mass of the hadronically decaying W boson can be inferred from the mass of the jets. For the leptonically decaying W boson, the full kinematics of both the lepton and the neutrino are required. The longitudinal component of the neutrino cannot be directly measured as only momentum conservation can be applied to the transverse plane. Therefore an analytical method is applied to infer the neutrino p_z^{ν}, where the methodology originally derived in Ref. [92].

The method applies assumptions on the mass of the leptonic W boson, setting it to the pole mass of $m_W = 80.4$ GeV [93] and additionally assumes the lepton mass to be zero as it is much smaller than the m_W. Starting with the Einstein energy-momentum

relation, $m_W^2 = (E^l + E^\nu)^2 + (p^l + p^\nu)^2$, the equation can be expanding with the two mass assumptions included. Following the full derivation found in Appendix A.1, it can be simplified into a quadratic equation solvable for p_z^ν. It then follows that

$$p_z^\nu = \frac{p_z^l \zeta \pm \sqrt{\Delta}}{{p_T^l}^2} \tag{4.5}$$

$$\text{where} \quad \zeta = \frac{m_W^2}{2} + p_T^l p_T^\nu \quad \text{and} \quad \Delta = {p_z^l}^2 \zeta^2 - {p_\mathrm{T}^l}^2 [{E^l}^2 {p_\mathrm{T}^\nu}^2 - \zeta^2]. \tag{4.6}$$

This provides multiple solutions which also depend on the sign of Δ. If $\Delta > 0$, two physical solutions of p_z^ν are possible. Of the two, the smallest in its absolute value is taken to be the value of p_z^ν. If $\Delta < 0$, the solutions are complex. Therefore the real part of the solution is taken as the value [92]. With this, the full Lorentz vector of the neutrino is constructed. The value of the longitudinal momentum calculated using this methodology is validated against the truth level information for the signal process, with the result shown in Appendix A.2.

4.8 Proton Reconstruction

The reconstruction of forward protons starts from the spatial position of hits (x, y) in the Silicon Tracker of the AFP stations on A or C side. Various algorithms are applied in order to convert the hits into tracks. The track positions are converted into an energy value via a *Transport function* [50, 94]. The greater the track deflection, implies are larger energy loss shown schematically in Figure 4.3. The function simulates the positions of the AFP stations in which the track is reconstructed in and the LHC dipoles it passes by. The protons remain ultra-relativistic, such that $E/m \gg 1$ and are scattered at small angles where $p_\mathrm{T}/p_z \gg 1$. Therefore one can assume $E_\mathrm{proton} = p_z$ for the forward protons.

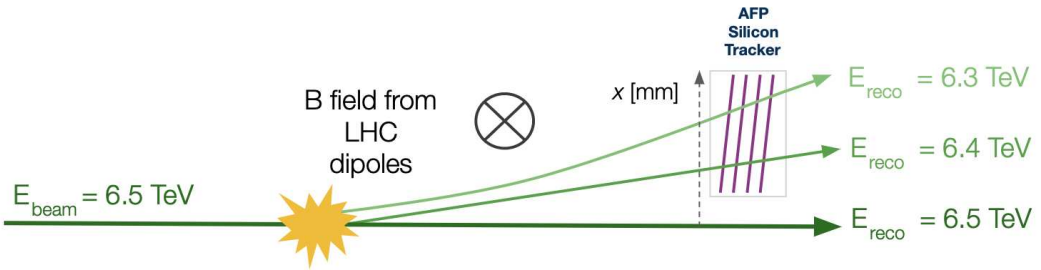

Figure 4.3. Schematic of forward protons deflected into the acceptance of the AFP detector. The energy of the protons can be inferred from the position of the proton track in x-direction.

A schematic describing the reconstruction chain of protons is shown in Figure 4.4. The first stage in the reconstruction is grouping the hits in the SiT planes into clusters. Hits which are adjacent to other hits in a given SiT plane, are grouped into clusters. Clusters

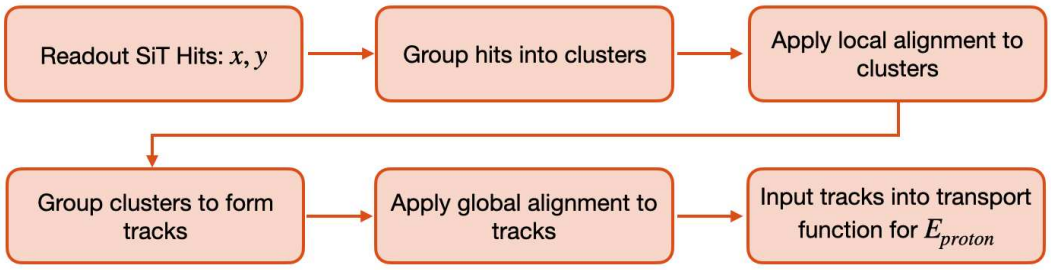

Figure 4.4. Schematic of the reconstruction chain of forward protons starting from the hits recorded in the silicon trackers. The calibration stages of the local and global alignment are applied in the reconstruction.

within a single tracker plane are known as local clusters. The next stage is the local interplane alignment. The planes can have small offsets, both spatial (and rotational) with respect to other planes of the order of $10 - 100$ µm (of the order of a few mrad). The local alignment is applied to the clusters as this impacts which local clusters are grouped to form tracks. This is done by performing iterative algorithms that reconstruct tracks from clusters with no alignment and quantify the residuals when modifying the alignment parameters. More details can be found in Ref. [95].

The distance between two clusters is calculated as

$$\sqrt{(x^1_{\text{clus.}} - x^2_{\text{clus.}}) + (y^1_{\text{clus.}} - y^2_{\text{clus.}})} < r^{\text{clus.}}_{\text{max}}, \tag{4.7}$$

where $r_{\text{max}} = 0.5$ mm. Clusters passing this requirement in a given station are used to construct the track. This is done for clusters in the same tracker plane and also neighbouring planes of the same station. A χ^2 test statistic of the track is used to measure the goodness of fit. It is calculated using the local cluster uncertainties which are driven by the SiT resolution. The minimum number of clusters required in a track is two. Following the track reconstruction, the global alignment of each station is applied to the tracks.

The global alignment of the station quantifies the position of each station with respect to the LHC beam. This shifts the coordinate of reconstructed tracks in x which directly impacts the kinematic reconstruction of E_{Proton}. The global alignment changes with the beam conditions and therefore it is determined for the different running conditions. The main parameters to be measured in the alignment are the tracker position, the nominal beam position and the individual station alignment. The tracker position is the distance between the edge of the tracker and the outer side of the floor of the Roman Pot. This is taken as a fixed value of -0.5 mm. The nominal beam position is determined via Beam Based Alignment, which are special runs in which the collimators are moved towards the beam until a sharp change in the rate is observed in the station. The last parameter is the individual station location dependence. This is quantified by analysis of the photon-

induced $\gamma\gamma \to \mu\mu$ process. A sample of data is taken during high luminosity collisions and filtered using muon triggers. The energy of the muons are reconstructed in the ATLAS detector. The Transport Function is inverted to take as input the energy of the muons and providing the expected proton track positions for producing muons of that energy. The position in x expected is compared to what is reconstructed by the AFP detector in data. If the station is has perfect alignment, the difference between the two values is at zero, once muon systematic uncertainties are considered. The offset of the Gaussian peak fitted to the difference in x is assumed to be due to the misalignment of the stations and is quantified [95].

It is required that the track of a proton is reconstructed in both the NEAR and FAR stations for a given side of the AFP detector. This is done by comparing the x and y position between the stations. The track is reconstructed as a proton if the following condition is satisfied,

$$\sqrt{(x_{\mathrm{FAR}} - x_{\mathrm{NEAR}}) - (y_{\mathrm{FAR}} - y_{\mathrm{NEAR}})} < r_{\mathrm{max}}^{\mathrm{Trk}}, \tag{4.8}$$

where $r_{\mathrm{max}}^{\mathrm{Trk}}$ nominally is set to 2 mm. With the tracking information put into the transport function, the energy of the proton, E_{Proton}, can be determined. The fractional energy loss of the protons on a given side of the AFP detector is then defined as,

$$\xi_{\mathrm{AFP}}^{\mathrm{A/C}} = 1 - \frac{E_{\mathrm{Proton}}}{E_{\mathrm{Beam}}}, \tag{4.9}$$

where $E_{\mathrm{Beam}} = 6.5$ GeV for the Run 2 at the LHC. For a given photon-induced process, $pp \to p(\gamma\gamma \to X)p$, the fractional energy loss can be determined analogously with the ATLAS detector independently where,

$$\xi_{\mathrm{X}}^{\pm} = \frac{m_X}{\sqrt{s}} e^{\pm y_X}. \tag{4.10}$$

It is inferred from the mass m_X and rapidity y_X of the final state objects X, scaled by the centre of mass energy $\sqrt{s}$. The rapidity can be defined as positive or negative in order to match it to the A and C side of the AFP stations. The full derivation of Equation 4.10 can be found in Appendix B. The difference between ξ_{AFP} and $\xi_{\mathrm{X}}^{\pm}$ can be used to constrain the signal from photon-induced processes. The mass transfer of the protons, via the photons to the final state objects X, can be determined from AFP kinematics alone, such that

$$m_{\gamma\gamma} = \sqrt{s \cdot \xi_{\mathrm{AFP}}^{\mathrm{A}} \xi_{\mathrm{AFP}}^{\mathrm{C}}}. \tag{4.11}$$

This mass value should be the same as m_X if X is produced via a photon-induced process. The difference in mass can also be used additionally to constrain the signal. The fractional

energy loss of the AFP detector has an efficiency acceptance range where protons are well reconstructed, starting at $\xi_{\mathrm{AFP}}^{\mathrm{A/C}} = 0.035$. The upper limit of $\xi_{\mathrm{AFP}}^{\mathrm{A/C}} = 0.08$ is due to the position of neighbouring collimators [95].

Sources of Systematic Uncertainties

Systematic uncertainties are determined for various stages of the proton reconstruction and must be considered when using the AFP to reconstruct forward protons. The main systematic uncertainties can be categorised as following:

- Global Alignment: modifies tracker position parameter by ±300 µm, varying how close the tracker is to the beam. The modification to the misalignment in x is recalculated via the Gaussian widths fitted in the $\gamma\gamma \to \mu\mu$ events in data.
- Beam Optics: modifying the nominal horizontal crossing angle by 50 µrad. The nominal crossing angle in the dataset used for this thesis is $\theta_c = -150$ µrad [96].
- Track Reconstruction: Various conditions in the track reconstruction are modified to quantify the systematic uncertainty
  - The maximum distance between clusters $r_{\mathrm{max}}^{\mathrm{clus}}$ is modified from 0.5 mm to 0.4 mm.
  - The minimum number of clusters required to form a track is modified from 2 to 3 clusters.
  - The distance between track candidates in the NEAR and FAR stations, $r_{\mathrm{max}}^{\mathrm{Trk}}$ is modified from 2 mm to 1 mm.
- Local Alignment: modifies rotation of the first plane of all AFP stations around z-axis by 0.004 rad counterclockwise. This is the parameter with the largest uncertainty within the local alignment.

CHAPTER 5

DATA AND SIMULATIONS

Physics searches at the LHC make use of both data collected by the detectors and simulations of different physics processes. The simulations produced in this thesis are essential for three main purposes, first to optimise the kinematic selections applied to the events, understanding what aids the reduction of the different sources of background processes or constrains the signal better. The second is in the modelling of SM backgrounds, providing an estimate for background expected in the signal region. The last is modelling of new physics parameters such as EFTs in the signal region, presented in Chapter 8.

The dataset used for this thesis is presented in Section 5.1 with a description of the triggers used in filter for events of interest in the data. The fundamental stages simulated for a particle interaction are described in Section 5.2. The simulations produced for the process of interest, semileptonic $\gamma\gamma \to WW$ and SM background processes which are expected in the signal region are described in Section 5.3. Developed for this thesis, data driven modelling of pileup protons in the AFP detector is discussed in Section 5.4.

5.1 Dataset for the Analysis

The dataset used in this thesis corresponds to the Run 2 data collected by the ATLAS experiment during proton-proton collisions with a centre-of-mass energy of $\sqrt{s} = 13$ TeV. The *Good Run List* (GRL) [97] is first applied to filter out events when the detectors were not functioning correctly. For this thesis, a specific AFP Run 2 GRL is applied, which filters for data recorded where both the ATLAS and AFP detector are in operation. The main AFP requirements are that it is a data taking period where the Roman Pots are inserted into the physics position and the readout of data is functioning. This provides a dataset with an integrated luminosity of 14.6 fb^{-1}.

As previously discussed in Section 3.2.5, data must be triggered in order to be

recorded. Listed in Table 5.1 are the triggers used for this dataset correspond to unprescaled[1] single lepton triggers that are active during the period of data recording. For the electron channel required p_{T} thresholds of electron are indicated after the "e" in the trigger name. The isolation required is indicated after the "lh" in the trigger name. The lowest p_{T} has the Tight isolation, which is the most stringent of the isolations. This is due to low p_{T} jets, which may easily trigger and fulfill the electron requirements. The trigger therefore allows for soft electrons to be included in the measurement of this thesis.

Channel	Trigger
Electron	HLT_e26_lhtight_nod0_ivarloose
	HLT_e60_lhmedium_nod0
	HLT_e140_lhloose_nod0
Muon	HLT_mu26_ivarmedium
	HLT_mu50

Table 5.1. Triggers required to be fulfilled in the dataset used for this analysis. Listed are the unprescaled lepton triggers required for the electron and muon channels.

Triggers with higher lepton p_{T} thresholds can benefit from the looser isolation requirements, previously defined in Section 4.2. These triggers are used in combination with lower threshold triggers to reduce reconstruction efficiencies at high p_{T}. Figure 5.1a shows the electron p_{T} measured when different triggers are required in the signal simulation. The distributions shown are after the trigger and lepton ID requirements are applied to the event. The simulations have the same kinematic requirements as the trigger in order to reconstruct the behavior of the triggers in data. For a given trigger, the distribution peaks just after the threshold requirement. It shows the different lepton p_{T} regions where a combination of triggers can be used to reduce inefficiencies and benefit from the Tight isolation of the lowest threshold trigger.

Similar to the electron triggers, the muon triggers shown in Table 5.1 are also used in combination. The two triggers indicate the threshold after the "mu" in the muon name. The lower threshold muon trigger, HLT_mu26_ivarmedium, requires medium isolated muons, as indicated in the trigger name. The HLT_mu_50 trigger does not require any online isolation as the higher energy muons are well isolated. Figure 5.1b shows the muon transverse momentum reconstructed when the muon triggers are fulfilled. Simulations include trigger information by requiring the same kinematic requirements as that in data.

[1]Prescales are factors, f, applied to triggers to reduce trigger rates during data recording. A prescale of f indicates that if an event fulfills the trigger requirements, it is record every f-th time it does so.

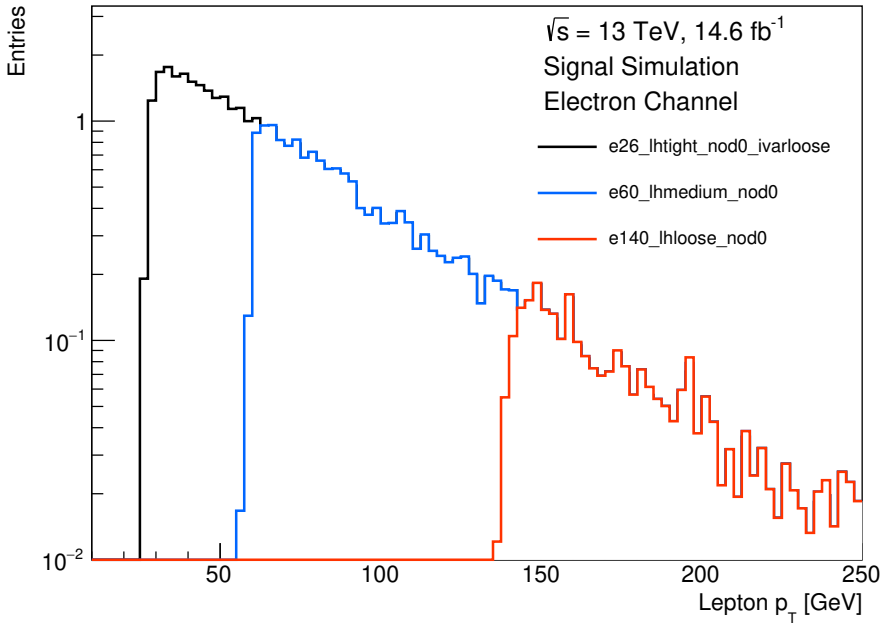

(a)

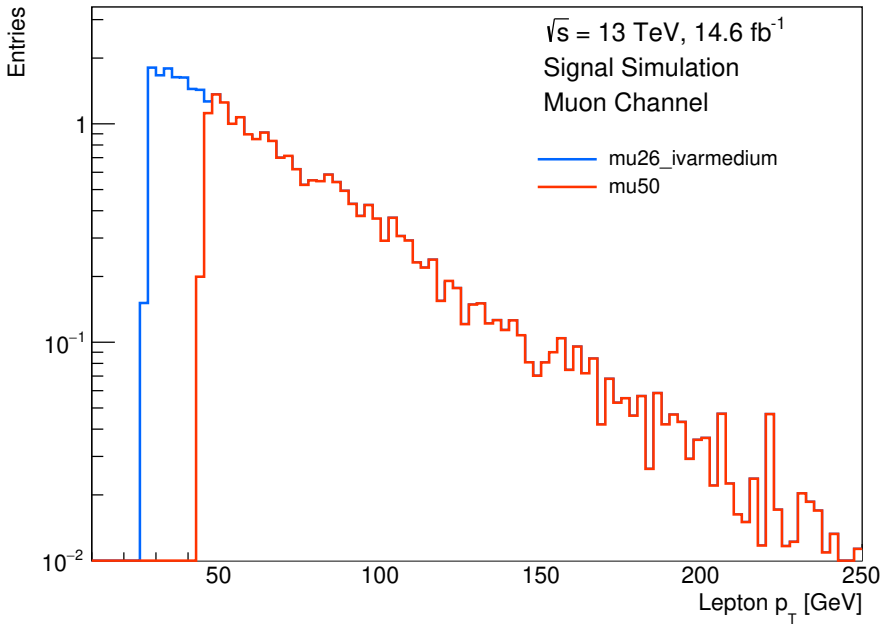

(b)

Figure 5.1. Distribution of lepton p_{T} when single lepton trigger requirements are fulfilled. Shown in Figure 5.1a are triggers for the electron channel and the muon channel is shown in Figure 5.1b.

5.2 Generating Simulations

The main stages in the generation of Monte Carlo (MC) simulations of a given particle interaction are as follows [98]:

1. Calculation of the cross section from first principles,
2. Modelling of parton showers,
3. Overlay of the underlying event,
4. Modelling the hadronisation,
5. Modelling the detector interaction.

The stages are shown schematically in Figure 5.2. The signal process simulated in this thesis is photon-induced whereas the background processes simulated are from inelastic proton-proton collisions. Therefore differences in simulating the signal and background processes will be highlighted in the relevant subsections below.

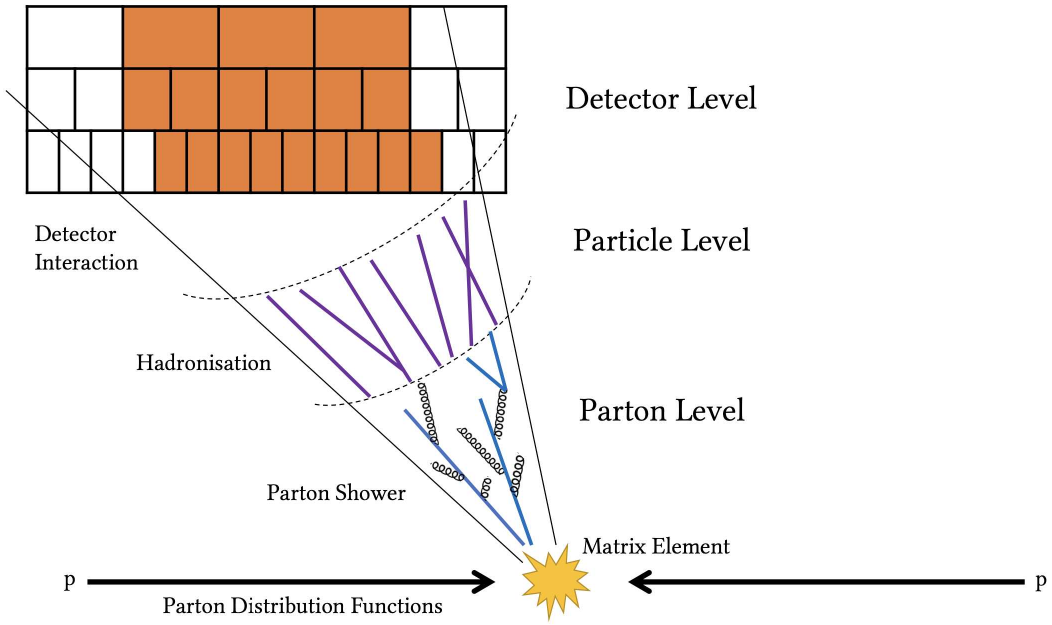

Figure 5.2. Schematic of the particle interaction from collision to detector reconstruction showing the stages which are simulated. Figure taken from Ref. [99].

5.2.1 Cross Section

The cross sections of the signal and background processes are derived differently due to the differences between the photon-induced and hard scatter interaction. Both methodologies are explained below.

Photon-Induced Cross Sections

In photon-induced processes such as the signal of interest, semileptonic $\gamma\gamma \to WW$ process, protons interact without breaking apart, preserving their internal structure. During these collisions, the protons exchange momentum via emitted photons which allow the protons to remain intact. The cross section can be derived from the *Equivalent Photon Approximation* [38] where the cross section of the process $p(\gamma\gamma \to X)p$ is expressed as

$$\sigma_{p(\gamma\gamma)p\to p(\gamma\gamma\to X)p} = \int \mathrm{d}\omega_1\omega_2 \frac{n(\omega_1)}{\omega_1}\frac{n(\omega_2)}{\omega_2}\sigma_{\gamma\gamma\to X}(\omega_1,\omega_2), \tag{5.1}$$

where $n(\omega)$ is the number of equivalent photons of energy ω follows,

$$n(\omega) = \frac{2}{\pi}Z^2\alpha_{\mathrm{EM}}\ln\left(\frac{\gamma}{\omega R}\right). \tag{5.2}$$

The Z is the atomic number of the particle producing the equivalent photons, $Z = 1$ for protons. The electromagnetic coupling is α_{EM}, R is the charge radius, the photon energies are ω_1 and ω_2 and γ is the relativistic Lorentz factor of the proton, defined in more detail in Ref. [100]. The total cross section is therefore obtained by integrating over all possible photon energies accounting for the photon flux from Equation 5.2. Higher momentum-transfer of the photon emission can occur from within a parton of the proton causing the proton to break apart after the emission. This can happen to one or both protons and is referred to as a single or double dissociative process [100]. Such events are not considered in this thesis as they cannot be constrained easily against the SM backgrounds.

Proton Inelastic Cross Sections

The background processes in this thesis originate from inelastic collisions at the LHC. The protons contain gluons which are in continuous fluctuation, producing short-lived virtual quark-antiquark pairs, known as sea quarks, which annihilate. At the high energies achieved at the LHC, gluons carry a significant portion of the total momentum of the proton. Due to this, the quarks and the gluons are in asymptotic freedom, as discussed in Section 2.1. The quarks and gluons can be considered independent particles, known as partons. In an inelastic proton-proton collision, a hard scattering interaction occurs

between two partons, a and b originating from protons A and B. The parton distribution function f_a and f_b represents the probability that the parton carries the momentum fraction of the respective protons. Parton distribution functions are determined from a combination of measurements such as that found in Ref. [101]. The total cross section, σ, of a given process $ab \to n$ can be factorised to

$$\sigma = \sum_{a,b} \int \mathrm{d}x_a \mathrm{d}x_b f_a(x_a, \mu_\mathrm{F}^2) f_b(x_b, \mu_\mathrm{F}^2) \mathrm{d}\hat{\sigma}_{ab\to n}(\mu_\mathrm{R}^2, \mu_\mathrm{F}^2). \tag{5.3}$$

The hard interaction $\mathrm{d}\hat{\sigma}_{ab\to n}$ in QCD allows for a perturbative expansion in orders of the strong coupling constant α_s. It relates to the *matrix element*, $|M_{ab\to n}|^2$, as $\mathrm{d}\hat{\sigma}_{ab\to n}(\mu_\mathrm{R}^2, \mu_\mathrm{F}^2) \sim |M_{ab\to n}(\mu_\mathrm{R}^2, \mu_\mathrm{F}^2)|^2 \mathrm{d}\phi_n$. The matrix element encapsulates the physical details of transitions from initial states a and b to a final state n, incorporating effects such as couplings and spin dynamics. It is derived from the SM Lagrangian using Feynman rules [98, 102]. The matrix element is derived numerically from Monte Carlo integration over the full ϕ_n phase space [98]. The renormalisation scale (μ_R) appears when regularising divergences which occur when including loop diagrams. These are known as *ultraviolet divergences*. The factorisation scale (μ_F) removes collinear divergences associated with initial-state parton emissions, known as *infrared divergences* [103].

5.2.2 Parton Shower

After the initial scattering, partons in both initial and final states typically undergo additional radiation before hadronisation. This cascade of radiation is known as the *Parton Shower*. In the parton shower, QCD and QED corrections are accounted for to model collinear and soft emissions which are typically dominant at the LHC. The emission of quarks and gluons are due to the strong interaction of QCD. This occurs from the splitting of quarks via $q \to qg$ and gluons via $g \to gg$ or $g \to q\bar{q}$ [98]. Colour coherence effects are also included at this level as it changes the angular emission of the gluons and quarks, in turn changing how one may experimentally observe the final state objects. For QED, contributions arise from the photons emitted from charged quarks. In the simulation of parton showers, algorithms perform the splitting as a cascade until a cut-off scale is reached. The cut-off scale prevents divergences which are not infrared or collinear safe. Typically this is at 1 GeV where the interaction strength is too large for perturbation theory to hold. It is at this scale that hadronisation is dominating [102].

5.2.3 Underlying Event

At this stage of the algorithm, the *underlying event* can be considered. It is defined as contributions not originating from hard scatter interaction of an inelastic event. These are known as multiple parton interactions which occur when more than one parton pair interact, typically a softer interaction [98]. These must be considered and are included with the parton shower. It is required in order to accurately predict the interactions at the LHC. For photon-induced processes, there is no underlying event present as the protons remain intact.

5.2.4 Hadronisation

After the parton showering the quarks and antiquarks form colourless states in a process called *hadronisation*. This is due to colour confinement, previously discussed in Section 2.1. It is simulated via phenomenological models such as the Lund-String model [104] or the cluster model [105]. Not all hadrons formed are stable and therefore subsequent decays of the hadrons must also be considered in the algorithms.

5.2.5 Detector Interaction

Specialised and detailed simulations of the ATLAS detector are required to reconstruct how particles interact with the detector. The ATLAS detector is simulated with `GEANT4` [106, 107] where the detector hits are digitised and the objects are reconstructed using algorithms described in Chapter 4. The simulation produced without the detector response and efficiencies included is known as the "truth-level", assuming the reconstruction is fully efficient. The inclusion of the detector response then provides what is known as the "reconstruction-level", which is very close to the response one may observe in data. Pileup is the effect of multiple proton-proton interactions per bunch crossing in the ATLAS detector. The pileup information is overlaid as a reweighting using the profile of the average number of simultaneous interactions per bunch crossing, $\langle\mu\rangle$. This is modelled for the different LHC conditions during data taking.

5.3 Monte Carlo Simulations Produced

Various MC simulations are available to provide models of physics processes in the ATLAS experiment. Two simulations of the signal, semileptonic $\gamma\gamma \to WW$, are used in this thesis. The first using `MADGRAPH5_aMC@NLO 2.6.5` for the matrix element and interfaced with a parton shower modelled with `PYTHIA 8`. The second signal simulation uses `HERWIG 7` for both the matrix element and parton showering. To ensure no bias in the simulation of photon-induced events, especially in the parton showering, the two simulations are compared. Both simulations use a specific showering setting available in the MC generator which model the protons to both be scattered without breaking up. Therefore the signal simulates information of forward protons.

There are five main background processes which are simulated for this thesis from proton-proton inelastic collisions. The three electroweak processes modelled are diboson production, which decay via the semileptonic channel, and W or Z bosons produced in associated with a jet where the bosons decay leptonically, labelled as W/Z + jets. The production of a single top quark decaying leptonically and $t\bar{t}$ production in the fully leptonic decay channel are both simulated. A summary of the background simulations and the respective generators used for the matrix elements and parton showering can be found in Table 5.2. All background simulations are produced with a nominal QCD showering which does not include information about the forward protons. The inclusion of forward protons in the simulated background processes will be discussed in the Section 5.4.

Process	Generator	Parton Shower	References
Semileptonic $\gamma\gamma \to WW$	`MADGRAPH5_aMC@NLO`	`PYTHIA 8`	[108],[109]
	`HERWIG 7`	`HERWIG 7`	[110]
Diboson VV	`SHERPA v2.2.1`	`SHERPA`	[111]
W+ jets	`SHERPA v2.2.11`	`SHERPA`	[111]
Z+ jets	`SHERPA v2.2.11`	`SHERPA`	[111]
Leptonic Single t	`POWHEG BOX v2`	`PYTHIA 8`	[112], [109]
Leptonic $t\bar{t}$	`POWHEG BOX v2`	`PYTHIA 8`	[112], [109]

Table 5.2. Summary of simulated processes used in this thesis. Included for each process are the generators used to produce the matrix element and parton showering, along with relevant references.

5.4 Modelling Background Pileup Protons

To complete the simulation of background events, kinematic information of the forward protons need to be included. In the data, information from the AFP detectors is included as it is read out with the L1Accept signal in the ATLAS trigger system. However in MC simulations of inelastic, hard scattering processes, information concerning the forward detector is not included.

The signal simulation of semileptonic $\gamma\gamma \to WW$ use parton showering settings which model the photon-induced process and reconstructs the forward scattered proton. Additionally, in the pileup overlay during simulations of the detector interaction, the photon-induced simulations request modelling of forward protons. For background processes, pileup protons are not simulated at the detector interaction level. Therefore the simulated background events are overlaid with forward protons which are simulated using a data-driven method. On an event-by-event basis, the protons are added to the event in order to simulate background pileup protons in the AFP detector.

As there is low signal expectation in this analysis, the background protons are modelled with the AFP 2017 data set with loose kinematic requirements applied. Table 5.3 summarises the lepton requirements applied. The requirements are focused on the lepton kinematics as the triggers applied are also lepton based. The data set provides a large number of protons such that modelling of the proton kinematics will not be subject to statistical fluctuations. Protons in the AFP detector in background processes originate from pileup and single diffractive processes at the ATLAS interaction point, which are the dominant contributions. There are also contributions from beam halo and scatterings within the beam however these are very small [95]. Protons from the beam are typically absorbed by the collimators before reaching the AFP detectors. Therefore the forward protons in background processes are considered as *pileup protons*.

Cuts Applied
$p_{\mathrm{T}}^{lep} > 30$ GeV
$\lvert\eta^{lep}\rvert < 2.5$
Electron ID: TightLH
Muon ID: Medium

Table 5.3. Fiducial cuts and identification requirements applied to the data set to provide a sample of forward proton kinematics.

Two methodologies are used to overlay pileup protons on the simulations of background processes. The first is a *Sampling Method* which will be discussed in Section 5.4.1 and the second is the *Event Overlay Method* discussed in Section 5.4.2. Both methods

are compared to understand which is better suited for this thesis, and to cross check the consistency of the modelling.

5.4.1 Sampling Method

The *Sampling Method* uses distributions of the proton information as probability distributions which can be randomly sampled to construct proton information for the event. The distributions used are the proton multiplicity ($n^{\mathrm{A}}_{\mathrm{AFP}}$ and $n^{\mathrm{C}}_{\mathrm{AFP}}$) and proton fractional energy loss distributions ($\xi^{\mathrm{A}}_{\mathrm{AFP}}$ and $\xi^{\mathrm{C}}_{\mathrm{AFP}}$) which are constructed using the data with the cuts previously discussed. Figure 5.3 shows a schematic of how this method works. The distributions which are sampled are presented in Figure 5.4, showing the proton multiplicity per event, and the $\xi^{\mathrm{A/C}}_{\mathrm{AFP}}$ distribution for all protons in an event reconstructed.

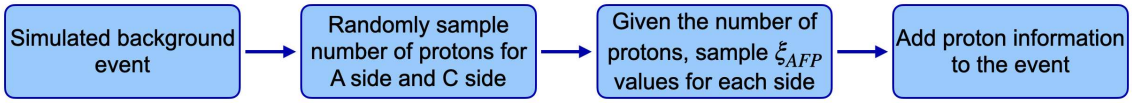

Figure 5.3. Summary of the stages of constructing pileup protons via the Sampling Method.

The proton multiplicity on the A side of the AFP detector, $n^{\mathrm{A}}_{\mathrm{AFP}}$, is sampled using Figure 5.4a as a weighted probability. If the number of protons sampled is i, the distribution of the $\xi^{\mathrm{A}}_{\mathrm{AFP}}$ (Figure 5.4b) is sampled i times such that each proton has an associated value. Similarly, this is done for the C side of the AFP detector for every event. This information is then saved with the simulated background event. The full event selection can be applied to the proton kinematics.

The distribution of proton multiplicity has the 0^{th} bin removed. This forces the background event to always have protons on the A and C side of the AFP detector. The 0^{th} bin has the most events and removing it increase the number of background events which pass the event selection requirements of reconstructing at least one proton at both A and C side. This choice is motivated due to its large reduction in the statistical uncertainty of the total number of background events. This aids the modelling of the pileup protons in the background as it will not be subject to statistical fluctuations. After the requirement of reconstructing protons on both sides of the AFP detector, the number of background events are then rescaled to reflect the true probability of the event passing this requirement. The factor for rescaling is determined with the dataset. It is verified in the data, how many events had protons reconstructed out of the total number of events for a given side. A rescaling factor of 0.23 is found, as seen in Table 5.4. The table presents the probability found in data that the event would have protons on a given side and both sides of the AFP detector.

To confirm the methodology models the protons correctly in the background simulation, the obtained pileup proton kinematics are compared to data. It must be considered

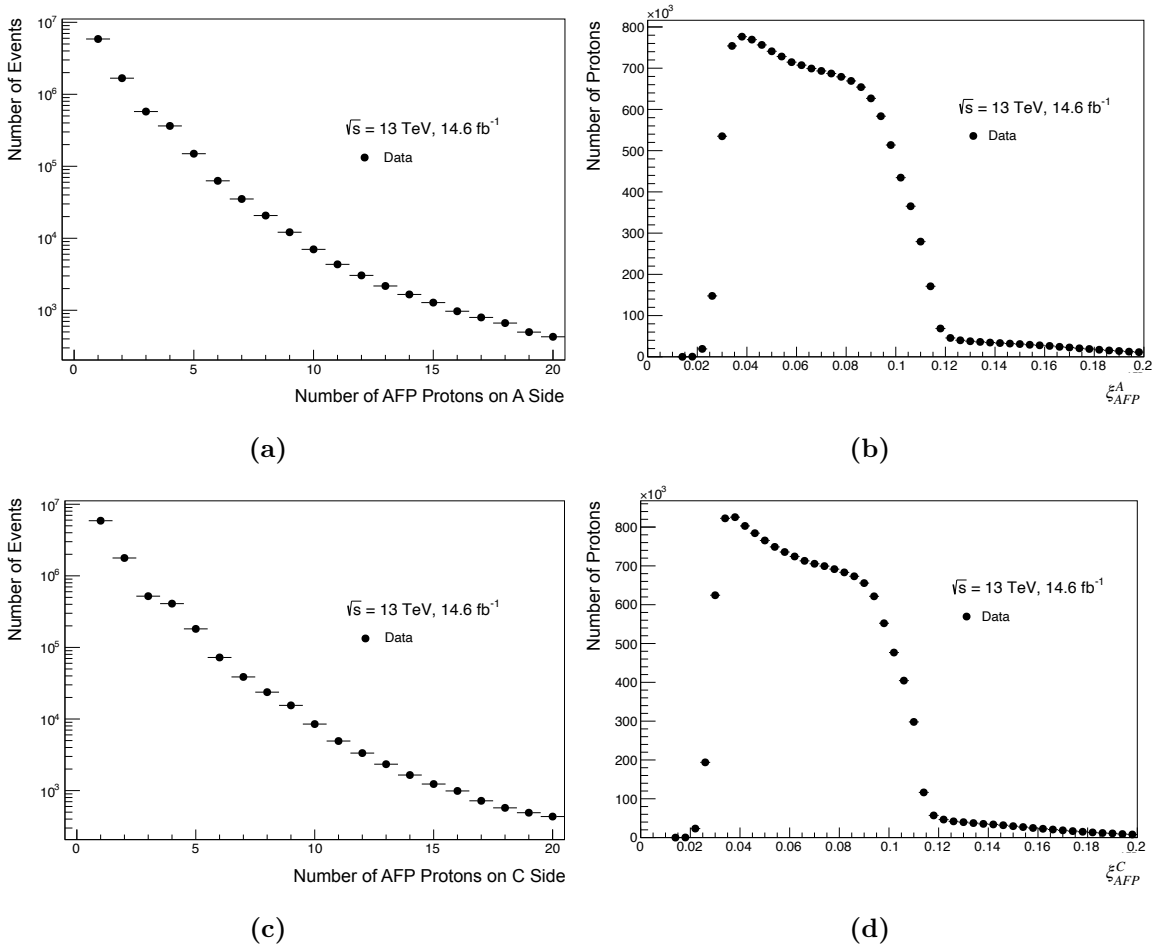

Figure 5.4. The data distributions used in the sampling method are shown above. Figures 5.4a and 5.4c show the proton multiplicity on A and C side respectively. The ξ_{AFP} values are shown in Figure 5.4b and 5.4d showing the distributions for all protons in the event.

Number of Protons	Probability
$n^{\mathrm{A}}_{\mathrm{AFP}} > 0$	0.48
$n^{\mathrm{C}}_{\mathrm{AFP}} > 0$	0.49
$n^{\mathrm{A}}_{\mathrm{AFP}} > 0 \cap n^{\mathrm{C}}_{\mathrm{AFP}} > 0$	0.23

Table 5.4. Probability of protons not being reconstructed for a given or both sides of the AFP detector. The probabilities are propagated through the event rates after the AFP event selection requirements. This is required to compensate for the additional events included in the analysis due to the removal of the 0^{th} bin in the proton multiplicity distribution.

that the measurement of this thesis is completed with the data initially blinded. Therefore a kinematic cut of $|\xi^{+/-}_{WW} - \xi^{\mathrm{A/C}}_{\mathrm{AFP}}| > 0.01$ is applied to the data and the simulated background. This cut ensures that the phase space where the validations are performed are orthogonal to the signal region. The complete fiducial cuts defining the signal region are discussed in Chapter 6. In addition to this cut, the other requirements previously

stated in Table 5.3 are also applied, together constructing a *Loose Control Region*. As the proton overlay is independent of the background process, the simulated backgrounds are shown as a *Total Background* simulation which is the sum of all background processes indicated in Section 5.3.

This Loose Control Region is not subject to statistical fluctuations, which allows for the shape of the kinematics verified when comparing to data. The disadvantage is that not all backgrounds which are present in the data with the loose event are considered in the total background. Only the background processes simulated are those which are most likely to be present in the signal region after the event selection is applied. For example, Z boson production will be removed once the mass of the jets are constrained to the W boson mass, or the missing b-tagged jets veto will remove large contributions from fully hadronic top-antitop quark production. Therefore it is expected that a systematic offset will be present between the data and total background simulated.

Figure 5.5 shows the distribution for the A and C side of the AFP detector, with the kinematic acceptance of the AFP detector indicated. This is the region in which protons are reconstructed with full efficiency and will be considered in the measurement of this thesis, as previously discussed in Section 4.8. For both distributions shown in Figure 5.5, the shape of the proton ξ_{AFP} is well modelled as the ratio of Data/Background simulated is consistent in the proton acceptance regions indicated. Due to only using simulated background processes which are expected in the signal region, it can be seen in the ratio of the data over total background that there is a systematic offset.

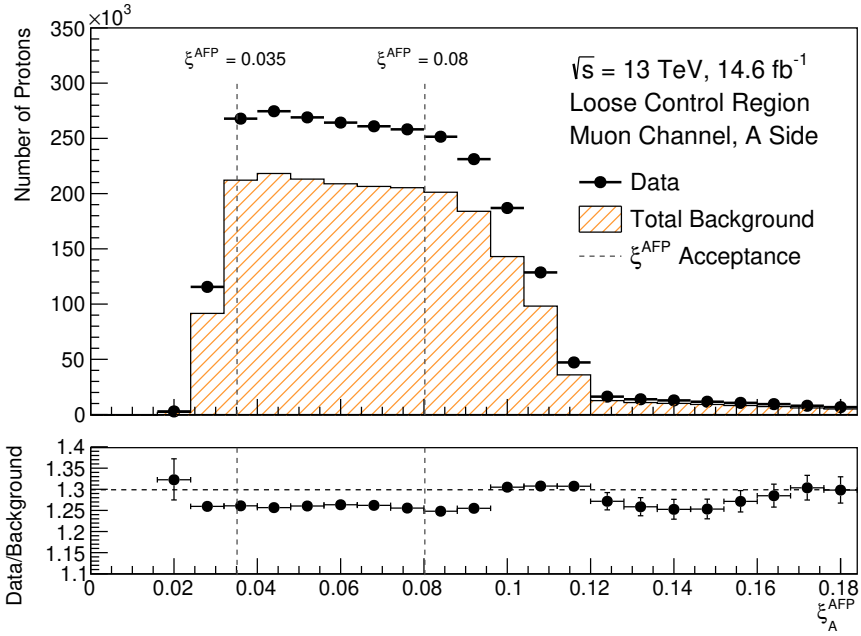

(a)

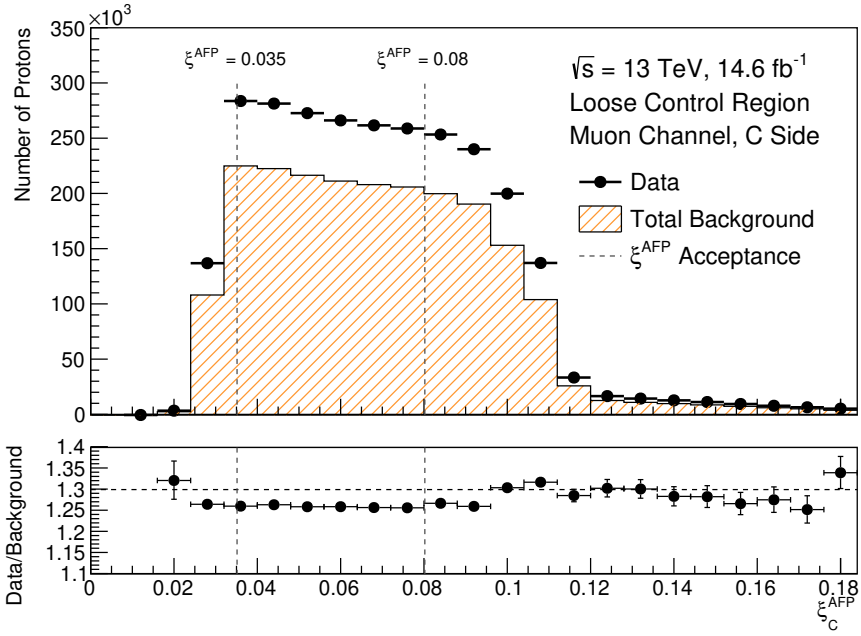

(b)

Figure 5.5. Distribution of the proton fractional energy loss modelled in background simulations using the *sampling method*. Distributions shown are for the muon channel, for both A Side (Figure 5.5a) and C Side (Figure 5.5b) of the AFP detector. Lower panels show the ratio of Data/Total Background simulated.

5.4.2 Event Overlay

The second method to add proton kinematics to the background simulations is via the *Event Overlay* method. The same dataset from the previous method is used. The steps of the Event Overlay method are summarised in Figure 5.6. For a given simulated background event, a random event is chosen from the dataset. All the proton information from this event is then added to the background event, which is the number of protons tagged on A side and C side, and their respective values of the fractional energy loss. This method considers proton information from both sides of the AFP detector, rather than independently as done in the sampling method. If there are strong kinematic correlations between the A and C side of the detector, it is expected to be shown when comparing the two methodologies. Once the proton information is duplicated from this data event, the same loose event selection is applied. The number of events in the dataset is of the order 10^7, thus unlikely that the same event is randomly sampled twice.

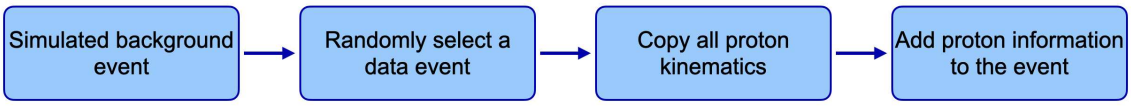

Figure 5.6. Summary of the stages of constructing pileup protons which are added to the simulated background events using the Event Overlay Method.

The same Loose Control Region is defined and applied to the dataset and the background simulated in the Event Overlay method. Figure 5.7 shows the distributions of the proton ξ_{AFP} for the muon channel. In the regions marked as the AFP detector acceptance, the shape is well modelled as the ratio of the data against total background is consistent. Similarly to the sampling method, there is a systematic offset present between the simulation and data, shown in the ratio. This is due to background processes present in the data which are not included in the total background simulated. Similar results for both methodologies are obtained when looking at the electron channel.

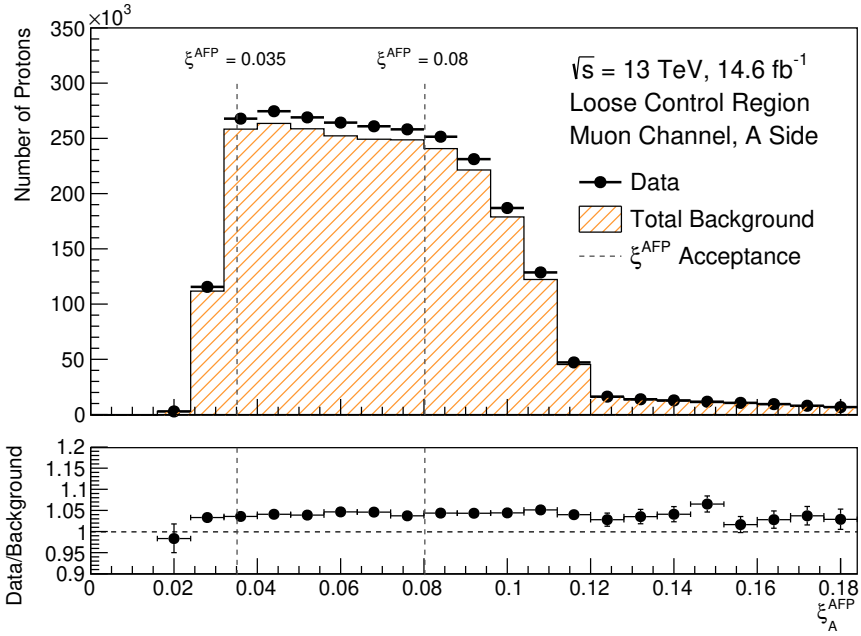

(a)

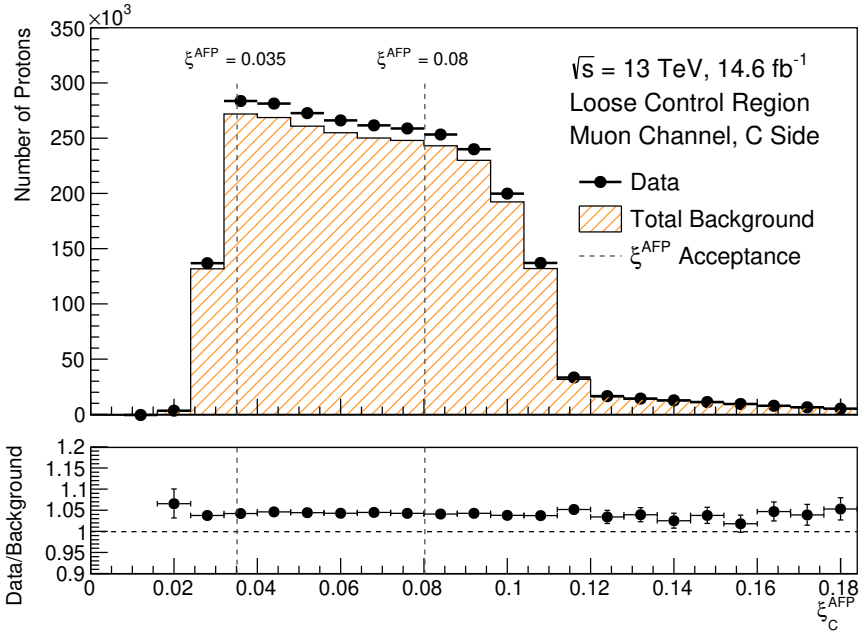

(b)

Figure 5.7. Distribution of proton fractional energy loss modelled in background simulations using the *Event Overlay* Method. Shown for the A side (Figure 5.7a) and C side (Figure 5.7b) side of the AFP detector in the muon channel. Lower panels show the ratio of Data/Total Background simulated.

5.4.3 Comparison of Methods

Both methods are confirmed to model the data well. This is shown in Figures 5.5 and 5.7 when comparing the background distributions of the proton fractional energy loss ξ_{AFP} to data. To confirm that the choice of a given method does not bias the modelling of background pileup protons in this thesis, the complete event selection later discussed in Chapter 6 are applied to the distributions. Later in this thesis Control Regions will be defined, however one can simply consider the control region as phase spaces orthogonal to the signal region of interest. The distributions of the protons ξ_{AFP} for the two methods are compared for the CR2 Muon channel in Figure 5.8. The statistics in this region is smaller than the loose control regions previously defined, however within the uncertainties, one can see that the Data/Background ratios within the marked acceptance of the AFP detectors are in agreement between the sampling method and the event overlay method. This demonstrates that the two methods are consistent in the modelling of the forward protons due to pileup. Similar results are obtained for the electron channel and can be found in Appendix C. The sampling method is favoured over the event overlay as it is computationally more efficient only requiring kinematic proton histograms at run time rather than full data set. The sampling method is therefore taken as the nominal method and used in this thesis to perform measurements of the background protons for the rest of this thesis.

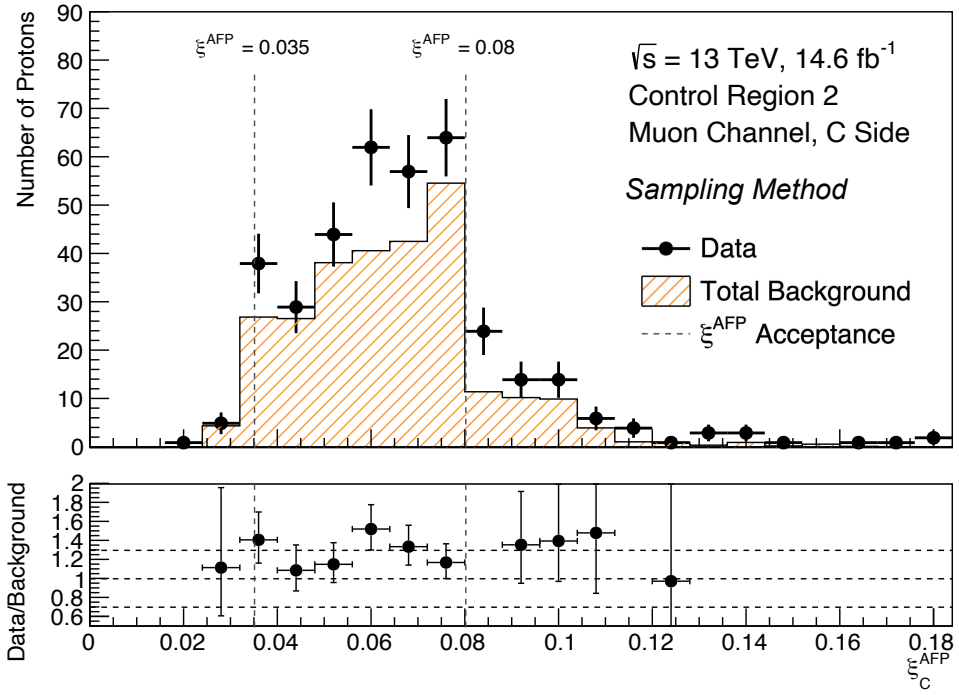

(a)

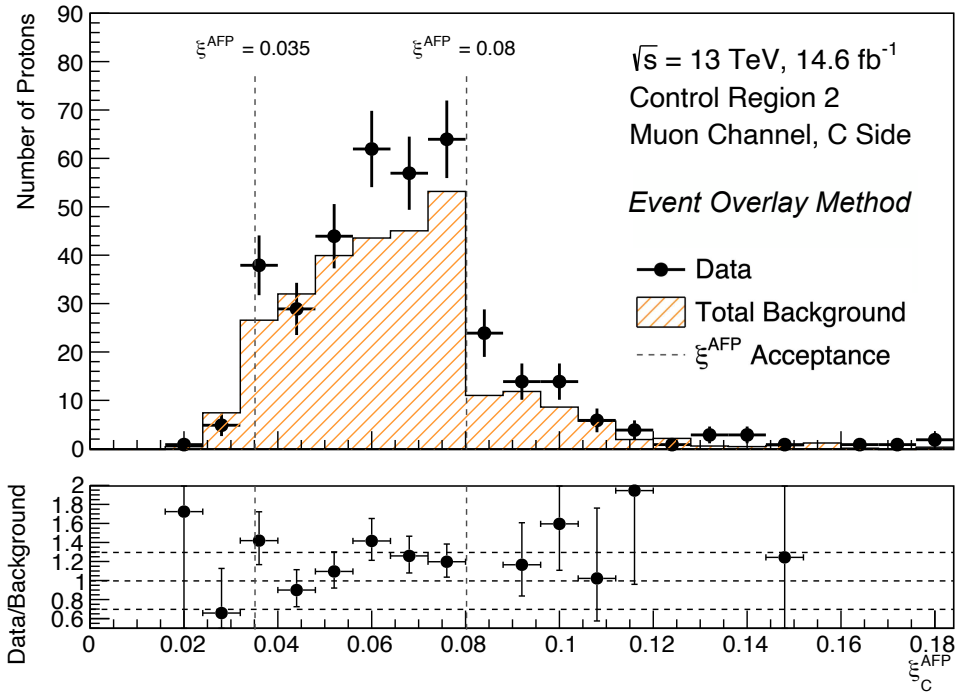

(b)

Figure 5.8. Distribution proton fractional energy loss modelled in background simulations in the CR2 muon channel. Compared is the Sampling method in Figure 5.8a with the Event Overlay Method in Figure 5.8b. Lower panels show the ratio of Data/Total Background simulated.

CHAPTER 6

THE $\gamma\gamma \to WW$ ANALYSIS

This chapter will present the process of interest for this thesis, the semileptonic $\gamma\gamma \to WW$ production. This photon-induced process can occur in the Standard Model via the t- and u-channel which give rise to a triple γWW vertex, or via the quartic $\gamma\gamma WW$ coupling, as shown in Figure 6.1. The AFP detector is used to reconstruct the scattered forward protons and the ATLAS central detector to reconstruct the decay products of the WW bosons. Using kinematic information from both detectors, the signal can be constrained.

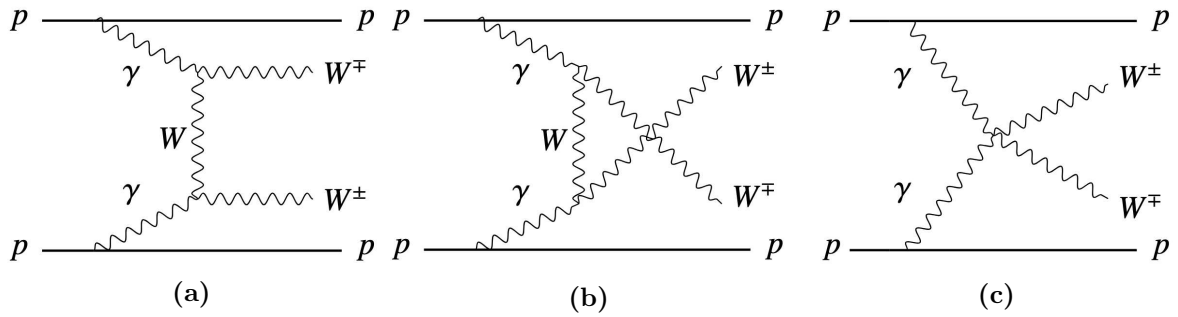

Figure 6.1. Feynman diagrams of Standard Model $pp \to p(\gamma\gamma \to W^{\pm}W^{\mp})p$ process at leading order. The t- and u- channels are shown in Figures 6.1a and 6.1b respectively, giving rise to the γWW vertex. Figure 6.1c shows the diagram of the quartic $\gamma\gamma WW$ coupling of this process.

Details of the signal process will be discussed in Section 6.1 explaining the essential kinematics taken advantage of to define the different resolved and boosted signal regions. The two channels will require different object and event selection requirements, which are presented in Section 6.2. With the kinematic selections and requirements applied, the simulated SM expectations of the signal and background processes in the respective signal regions are discussed in Section 6.3. The section will also define the aim and strategy taken in this thesis.

6.1 Signal Process and Regions

The semileptonic $\gamma\gamma \to WW$ signal process is defined by the decay products reconstructed in the ATLAS detector and AFP detector. Figure 6.2 shows the complete Feynman diagram of the process with the final state objects for the semileptonic channel. Signatures of this process are the forward protons, a lepton (electron or muon), a neutrino and jets from the quarks of the hadronic decay of the W boson. This thesis reconstructs the full Lorentz vector of the neutrino, using missing transverse momentum and inferring the longitudinal momentum using the methodology presented in Section 4.7. In this section, the definition of the different signal regions will be presented.

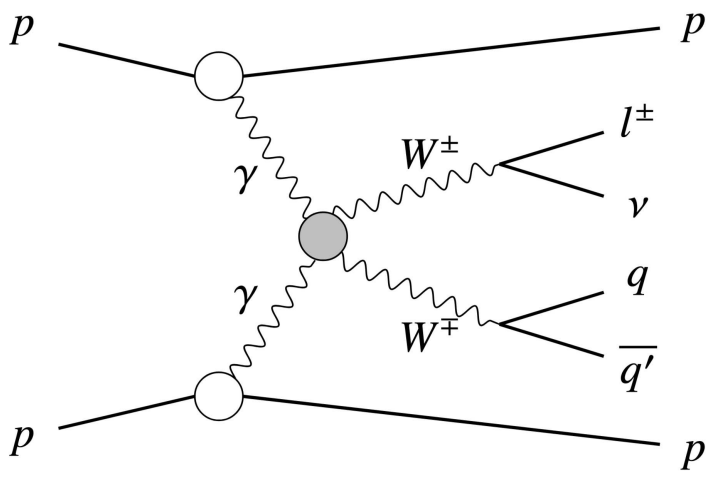

Figure 6.2. Feynman diagram of the semileptonic $\gamma\gamma \to WW$ process. Shown also in this diagram are the forward protons which emit peripherally colliding photons.

Signal Regions

The difference in the fractional energy loss of the protons, $\xi_{\mathrm{AFP}}^{\mathrm{A/C}}$ and the central WW system is the key kinematic requirement to constrain the signal process. Analogously to $\xi_{\mathrm{AFP}}^{\mathrm{A/C}}$, the fractional energy loss of the WW system with respect to the beam energy can be expressed as

$$\xi_{WW}^{\pm} = \frac{m_{WW}}{\sqrt{s}} e^{\pm y_{WW}}, \tag{6.1}$$

where m_{WW} is the mass and y_{WW} is the rapidity of the WW bosons in the final state (previously defined in Equation 4.10). The rapidity and the mass are inferred from the final state objects. The fractional energy loss of the WW system, $\xi_{WW}^{\pm}$, in the direction of the positive (negative) rapidity corresponds to the A (C) side of the detector. This variable is constructed using only information from the central ATLAS detector and is therefore independent from the AFP detector.

The $\xi^{\pm}_{WW}$ provides information about the energy required from the protons to produce the WW decay products. For the signal process, this value is the same as the energy loss of the protons, $\xi^{\mathrm{A/C}}_{\mathrm{AFP}}$. Assuming perfect reconstruction of the final state objects, the difference should be zero for this process such that $|\xi^{\mathrm{A/C}}_{\mathrm{AFP}} - \xi^{\pm}_{WW}| = 0$. The $|\xi^{\mathrm{A/C}}_{\mathrm{AFP}} - \xi^{\pm}_{WW}|$ requirement defines the two signal regions after the other object and event selection are applied to the data and simulation where

- Signal Region A: requiring $|\xi^{\mathrm{A}}_{\mathrm{AFP}} - \xi^{+}_{WW}| < 0.01$
- Signal Region C: requiring $|\xi^{\mathrm{C}}_{\mathrm{AFP}} - \xi^{-}_{WW}| < 0.01$.

The two regions are not independent as events can enter both regions when the fractional energy difference is small on both sides. Therefore, the thesis will perform measurements of the background estimation and EFT limits in both signal regions, providing two measurements which can verify each other.

Resolved and Boosted Channels

Photon-induced processes produce the decay products back-to-back due to no transverse momentum transfer from the emission of photons from the scattered protons. The W bosons are produced at $\Delta\phi = \pi$ in the detector and therefore can have a large boost.

The decay of the hadronic W boson in this process can be defined in two ways concerning the boost of the W boson. They are categorised based on the decay products of the hadronic W boson where it can be:

- Resolved: the two quarks produced are reconstructed as two resolved jets with radius $R = 0.4$
- Boosted: the two quarks are radiated collinear and this is reconstructed as one large jet of radius $R = 1.0$

The choice of studying both channels allows for measurements of the sensitivity in two settings as a channel may favour better background reduction, while the other favours the topology of the signal. The choice is non-trivial, thus in this thesis both resolved and boosted channels are studied to understand how the measurements can be constrained in the different channels. The event selection of the resolved and boosted channels differ as the construction of the respective jets have varying kinematic requirements in the construction. Therefore, event selections are defined independently for the resolved and boosted channels. In total, four signal regions are used to test the sensitivity of this process to new physics: Resolved A side, Resolved C side, Boosted A side and Boosted C side.

6.2 Object and Event Selection

The object and event selection of the resolved channel and boosted channels are defined in this section. The same event selection is applied to the signal regions on A and C side for a given channel with the exception of the $|\xi_{\mathrm{AFP}}^{\mathrm{A/C}} - \xi_{WW}^{\pm}|$ requirement. As the lepton in the final state can be an electron or muon, the various channels are further divided into the electron and muon channel. Therefore, for the lepton channel of interest, the electron or muon kinematics are applied. The event selection for all other objects are applied identically for the respective lepton channels.

6.2.1 Resolved Channel

The event and object selection of the resolved channel is optimised to increase signal to background ratio in the region. The selection criteria is chosen such that it favours the signal topology or reduces background contributions. All jets in this channel are reconstructed only using the small radius jet algorithms discussed previously in Section 4.1.1. The full event selection is summarised in Table 6.1.

The electrons and muons have similar requirements. Both are required to have a transverse momentum of $p_{\mathrm{T}} > 30$ GeV and pseudorapidity of $|\eta| < 2.5$, which is within the phase space covered by the calorimeters system. The number of electrons or muons required in the event is strictly one, which favours the signal topology where also only one lepton is expected. It is required that the electron passes the Loose isolation requirement and the Tight identification requirement. For the muon, Medium identification is required along with a Loose isolation. The isolation requirements reduce contributions from events where the lepton may have been produced in the decay of heavy flavour jets.

Kinematics relating to the primary vertex and the lepton track can be used to further reduce contributions from additional vertices originating from additional inelastic collisions due to pileup. The distance between the primary vertex and lepton track in the transverse plane is defined as the transverse impact parameter, d_0. Similarly, the distance along the beam line, i.e z-axis, is defined as the longitudinal impact parameter, z_0. To ensure the electron (muon) is originating from the primary vertex, the impact parameters must satisfy $|d_0/\sigma_{d_0}| < 5(3)$ and $|z_0 \sin\theta| < 0.5$ mm.

The resolved jets concern jets in the event reconstructed with a radius of $R < 0.4$. Both the leading (j_0) and subleading (j_1) jet require a minimum transverse momentum of $p_{\mathrm{T}} > 25$ GeV and a pseudorapidity of $|\eta| < 2.5$. In order to reduce background processes involving jets originating from b-hadrons, a veto is applied on jets which are "b-tagged", discussed previously in Section 4.1.1. Such events are dominantly due to production of top quarks. The event is required to have no additional jets with $p_{\mathrm{T}} > 10$ GeV to reduce contributions from processes where more than three jets may be produced. Noise in the

calorimeter may be reconstructed as jets with very low p_{T}. This is expected given the high pileup conditions of the LHC and can occur during events which may still be from the signal. Thus a minimum transverse momentum requirement is applied to veto the additional jets.

Kinematic criteria are additionally applied when considering both the leading and subleading jet with respect to each other. The jets produced in the signal process are expected to decay in a similar direction and therefore a fiducial cut of $\Delta\eta(j_0, j_1) < 1.5$ is applied. The dijet system is constructed by the Lorentz sum of the two jets, where various kinematic requirements can be applied to this system. Motivated by the W bosons recoiling off one another in the signal process, the dijet system requires a $p_{\mathrm{T}}(j_0, j_1) > 100$ GeV cut in order to reduce backgrounds from softer background processes. The mass of the dijet system is constrained around the W mass such that $m(j_0, j_1) \in [50, 100]$ GeV. This is applied in order to reduce contributions from QCD events with heavy dijet systems.

The missing transverse momentum reconstructed in an event is required to be greater than $p_{\mathrm{T}} > 40$ GeV. As the signal process will produce the W bosons such that they recoil against each other, it is expected that the leading jet from the hadronic W boson and the neutrino are well separated in the transverse plane. Therefore a cut of $\Delta\phi(j_0, \text{Missing } p_{\mathrm{T}}) > 0.8$ is applied.

The kinematics of the lepton and neutrino are combined in order to optimise the selection of the leptonically decaying W boson. A transverse momentum cut is applied of $p_{\mathrm{T}}(l, \nu) > 30$ GeV. The transverse mass of the system is calculated from the lepton and missing transverse momentum, as $m_{\mathrm{T}} = \sqrt{2p_{\mathrm{T}}^{l} p_{\mathrm{T}}^{\mathrm{miss}}(1 - \cos(\phi_l - \phi_\nu))}$. A requirement of $m_{\mathrm{T}}(l, \nu) > 40$ GeV is applied. Both kinematic requirements reduce contributions from background processes.

In this thesis, the signal includes both protons to scatter into the forward region and remain intact without disintegrating. Therefore to constrain the signal, the proton multiplicity in both AFP stations, A and C side, are required to be greater than zero. This requirement is applied as background processes are less likely to have pileup protons at both stations simultaneously. The forward protons are required to have $\xi_{\mathrm{AFP}}^{\mathrm{A/C}} \in [0.035, 0.08]$, matching the fully efficient reconstruction acceptance of $\xi_{\mathrm{AFP}}^{\mathrm{A/C}}$. Two protons must be selected in the event, one from each AFP station in order to determine which protons are to be matched with the WW kinematics in the central detector. For cases where the proton multiplicity is greater than one on A side (C side), the proton $\xi_{\mathrm{AFP}}^{\mathrm{A}}$ ($\xi_{\mathrm{AFP}}^{\mathrm{C}}$) closest to the value ξ_{WW}^{+} (ξ_{WW}^{-}) is chosen and other protons are omitted for the A (C) side. The last requirement on the forward protons is then applied to the selected A and C side protons, such that the mass is in the range of $m_{\gamma\gamma} \in [455, 1040]$ GeV. This is driven by the $\xi_{\mathrm{AFP}}^{\mathrm{A/C}}$ acceptance as $m_{\gamma\gamma} = \sqrt{\mathrm{s} \cdot \xi_{\mathrm{AFP}}^{\mathrm{A}} \xi_{\mathrm{AFP}}^{\mathrm{C}}}$, discussed previously in Section 4.8.

Given the kinematic constraints applied to the forward protons, the signal is expected

to have the same energy loss as there is a direct correlation between $\xi_{\text{AFP}}^{\text{A/C}}$ and $\xi_{WW}^{\pm}$ for photon-induced processes. Therefore the $\xi_{WW}^{\pm}$ is constrained in the range of [0.035, 0.08] and the mass is similarly cut as $m_{WW} \in [455, 1040]$ GeV.

The last requirement applied are the difference between the fractional energy loss of the protons and the relative energy required to produce the WW final state where for the A side signal regions, $|\xi_{WW}^{+} - \xi_{\text{AFP}}^{\text{A}}| \leq 0.01$. Similarly for the C side, requiring $|\xi_{WW}^{-} - \xi_{\text{AFP}}^{\text{C}}| \leq 0.01$.

6.2.2 Boosted Channel

The event and object selection for the boosted channel takes advantage of the high energy nature of boosted jets. For this channel, all jets are reconstructed with the large radius jet algorithms only, previously discussed in Section 4.1.2. The full event selection is summarised in Table 6.2.

The electrons and muons have a higher cut on the transverse momentum in this channel, of $p_{\text{T}} > 100$ GeV. For the signal, it is expected that the lepton is also boosted as it recoils against the hadronic W boson decay product. The other requirements for the leptons follow the same as the resolved channel.

The boosted jet reconstructed in the event requires a minimum transverse momentum of 200 GeV. This is due to the calibration algorithms of the boosted jets starting at this value. The same pseudorapidity cut of $|\eta| < 2.5$ is applied. The large radius jets have taggers which help constrain the origin of the jet. The W mass tagger is required to be passed. This ensures the jet is more likely to originate from the decay of a hadronic W boson than a boosted QCD jet. With this tagger, a tighter cut can also be applied on the mass, requiring $m_{\text{jet}} \in [60, 90]$ GeV. There are no heavy quark taggers for large radius jets, such as the b-jet tagger in the resolved channel. Therefore, in order to reduce contributions from top quark production, and its subsequent hadronic decays, it is required that $n_{\text{jets}} = 1$.

The missing transverse momentum has a higher cut than that in the resolved channel of $p_{\text{T}} > 50$ GeV. With the higher p_{T} cut on the leptons, the signal process also has a higher missing transverse momentum. The kinematic requirements applied to the forward protons and the WW system are identical to that of the resolved channel.

A cut is applied on the ratio of the mass of the WW system and the mass loss of the protons. The values are directly correlated for the photon-induced process and therefore a $m_{\gamma\gamma}/m_{WW} \in [0.7,1.3]$ is applied. This is done for the boosted channel as the mass resolution of a boosted jet is better and therefore can be used to reduce background contributions. Similarly to the resolved channel, the $|\xi_{WW}^{\pm} - \xi_{\text{AFP}}^{\text{A/C}}|$ cut defines the signal region for A and C side.

	Requirements
Electron	$p_T > 30$ GeV
	$\|\eta\| < 2.5$
	$n_{\text{Electrons}} = 1$
	$\|d_0/\sigma_{d_0}\| < 5$ and $\|z_0 \sin\theta\| < 0.5$ mm
	Tight Identification and Loose Isolation
Muon	$p_T > 30$ GeV
	$\|\eta\| < 2.5$
	$n_{\text{Muons}} = 1$
	$\|d_0/\sigma_{d_0}\| < 3$ and $\|z_0 \sin\theta\| < 0.5$ mm
	Medium Identification and Loose Isolation
Resolved Jets	For both jets $p_{\text{T}} > 25$ GeV
	For both jets $\|\eta\| < 2.5$
	No b-tagged jets in the event
	No other jets with $p_{\text{T}} > 10$ GeV
Dijet	$\Delta\eta(j_0 j_1) < 1.5$
	$p_{\text{T}}(j_0, j_1) > 100$ GeV
	$m(j_0, j_1) \in$ [50, 100] GeV
Missing Transverse Momentum	$p_{\text{T}} > 40$ GeV
	$\Delta\phi$(Leading Jet, Missing p_{T}) > 0.8
Forward Protons	$n^{\text{A}}_{\text{AFP}} > 0$ and $n^{\text{C}}_{\text{AFP}} > 0$
	$\xi^{\text{A/C}}_{\text{AFP}} \in$ [0.035, 0.08]
	For the protons selected, $m_{\gamma\gamma} \in$ [455, 1040] GeV
Lepton and Neutrino	$p_{\text{T}}(l, \nu) > 30$ GeV
	$m_{\text{T}}(l, \nu) > 40$ GeV
WW System	$\xi^{\pm}_{WW} \in$ [0.035, 0.08]
	$m_{WW} \in$ [455, 1040]
ATLAS & AFP	For A side Signal Region $\|\xi^{+}_{WW} - \xi^{\text{A}}_{\text{AFP}}\| \leq 0.01$
	For C side Signal Region $\|\xi^{-}_{WW} - \xi^{\text{C}}_{\text{AFP}}\| \leq 0.01$

Table 6.1. Event selection for the signal regions in the resolved channel.

	Requirements
Electron	$p_T > 100$ GeV
	$\lvert\eta\rvert < 2.5$
	$n_{\text{Electrons}} = 1$
	$\lvert d_0/\sigma_{d_0}\rvert < 5$ and $\lvert z_0 \sin\theta\rvert < 0.5$ mm
	Tight Identification and Loose Isolation
Muon	$p_T > 100$ GeV
	$\lvert\eta\rvert < 2.5$
	$n_{\text{Muons}} = 1$
	$\lvert d_0/\sigma_{d_0}\rvert < 3$ and $\lvert z_0 \sin\theta\rvert < 0.5$ mm
	Medium Identification and Loose Isolation
Boosted Jets	$p_{\text{T}} > 200$ GeV
	$\lvert\eta\rvert < 2.5$
	$m_{\text{jet}} \in$ [60, 90] GeV
	$n_{\text{jets}} = 1$
	W mass tagger passed
Missing Transverse Momentum	$p_{\text{T}} > 50$ GeV
Forward Protons	$n^{\text{A}}_{\text{AFP}} > 0$ and $n^{\text{C}}_{\text{AFP}} > 0$
	$\xi^{\text{A/C}}_{\text{AFP}} \in [0.035, 0.08]$
	For the protons selected, $m_{\gamma\gamma} \in [455, 1040]$ GeV
WW System	$\xi^{\pm}_{WW} \in [0.035, 0.08]$
	$m_{WW} \in [455, 1040]$
ATLAS & AFP	For A side SRs $\lvert\xi^{+}_{WW} - \xi^{\text{A}}_{\text{AFP}}\rvert \leq 0.01$
	For C side SRs $\lvert\xi^{-}_{WW} - \xi^{\text{C}}_{\text{AFP}}\rvert \leq 0.01$
	$m_{\gamma\gamma}/m_{WW} \in [0.7, 1.3]$

Table 6.2. Event selection for the signal regions in the boosted channel.

6.3 Event Expectations and Analysis Strategy

The event selection is applied to the simulated processes to understand the expected amount of signal and background in the respective signal regions. The simulations are scaled to the luminosity of the dataset used in this thesis, $L_{\text{int.}} = 14.6$ fb^{-1}. Listed in Table 5.2 are the MC simulations for which the event selection is applied to in this thesis.

Shown in Table 6.3 are the contributions of the signal semileptonic $\gamma\gamma \to WW$ from simulation. Two MC generators are used to ensure consistent results between the different modelling algorithms for photon-induced processes. The `MADGRAPH5_aMC@NLO` and `HERWIG 7` estimate the same signal contribution within the statistical uncertainties. The A and C side are also consistent, which is expected as the signal simulation contains both protons reconstructed. The values of the `MADGRAPH5_aMC@NLO` generator is taken as the nominal values for the signal expectation as the EFT simulations discussed later will also be produced with the same generator.

Signal Simulation	Resolved A Side	Resolved C Side	Boosted A Side	Boosted C Side
`MADGRAPH5_aMC@NLO`	0.38 ± 0.04	0.41 ± 0.04	0.10 ± 0.02	0.12 ± 0.02
`HERWIG 7`	0.39 ± 0.05	0.34 ± 0.05	0.10 ± 0.03	0.08 ± 0.02

Table 6.3. Expected signal contributions from two simulations of the semileptonic $\gamma\gamma \to WW$ processes for each signal region. Uncertainties are statistical only.

The event selections are applied to the various background processes to understand the background contribution in the signal regions. Shown in Table 6.4 are the number of events from different background processes in the signal region and the total background. For both resolved and boosted channels, the background processes dominate over the signal. This can be seen in Table 6.4 where, for example, the diboson backgrounds which are relatively small, still have a much larger contribution with respect to the signal due to the process cross sections. Therefore it is expected that the signal regions observe background events only, on assumption that the SM holds true.

The event selection for both channels successfully removes many background processes. However, the W + jets process dominates the signal region. For the boosted channels, there is also a significant contribution from $t\bar{t}$ events. The two processes are present after the event selection due to the topologies being similar to the signal.

The W + jets process includes all productions of the W boson such as vector-boson-fusion, bremsstrahlung and in association with jets. Typically, vector boson fusion production of the W boson are easily removed as the jets produced are well separated in their rapidity. Therefore they are unlikely to pass the dijet requirement of $\Delta\eta(j_0, j_1)$ and the mass requirement. The production of W bosons with jets via bremsstrahlung via

Background Process	Resolved A Side	Resolved C Side	Boosted A Side	Boosted C Side
W+jets	92.2 ± 2.7	92.2 ± 2.1	70.6 ± 1.4	75.5 ± 3.3
$t\bar{t}$	6.7 ± 0.3	6.7 ± 0.3	56.4 ± 0.8	56.6 ± 0.8
Diboson	4.1 ± 0.2	4.2 ± 0.3	5.2 ± 0.2	5.2 ± 0.2
Z+jets	1.7 ± 0.2	2.00 ± 0.2	4.2 ± 0.2	4.4 ± 0.2
Single t	0.2 ± 0.0	0.2 ± 0.0	1.3 ± 0.1	1.3 ± 0.1
Total Background	104.7 ± 2.8	105.2 ± 2.1	137.7 ± 1.6	142.9 ± 3.4

Table 6.4. Contributions of various background processes simulated with the event and object selections applied for the respective signal regions. Uncertainties shown are statistical only.

EW or QCD interactions can contribute into the signal region. This is due to low p_{T} jets which are close in ΔR where it may mimic that of a hadronically decaying W boson. The lower p_{T} also increases the likelihood to pass the $m(j_0, j_1) \in [50, 100]$ GeV cut (for the boosted channel [60, 90] GeV).

For W + jets process with more than two jets present due to higher order contributions, it can occur that the leading order jet is not reconstructed due to being out of the detector acceptance or due to reconstruction inefficiencies. This can result in a softer jet produced in association with the leading order harder jet- which then passes the event selections.

The production of top quark pairs is subdominant and small in the resolved channel, with respect to the W + jets processes. This is due to the success of the veto on b-jet tagged events. However, the contribution in the boosted channel is much larger. It passes the event selection when one of the b-quarks produces a jet which is successfully reconstructed as a large radius jet while the second b-jet is not within the acceptance of the detector and therefore not reconstructed. This rate is much higher in top pair production than single top production due to its topology. The back-to-back nature of the top pair production will lead to the jets produced in the final state being highly boosted, thus more likely to be reconstructed as a boosted jet.

Both the W + jets and $t\bar{t}$ processes will include a W boson which decays in the leptonic channel, and therefore pass many of the lepton and missing transverse momentum requirements. The forward proton requirements are passed due to the presence of pileup protons in the AFP detector.

As discussed previously in Section 5.4, pileup protons in the background simulation are modelled via a data-driven method where the proton multiplicity is always greater than zero. Therefore all simulated background events pass the multiplicity requirements. It is only after this cut is applied when the number of background events are rescaled.

The backgrounds events passing the $|\xi^{\pm}_{WW} - \xi^{\mathrm{A/C}}_{\mathrm{AFP}}|$ is due to the combinatorial nature of the background, discussed later in Chapter 7.

A large background contribution is expected in the signal region. The analysis presented in this thesis will provide a robust estimation of the background expected in the respective signal regions. The signal regions are blinded for the estimation of the background. This will be the basis of the null hypothesis that only SM backgrounds are present in the signal region. Upon unblinding the signal regions with the observed number of events observed in the data, the level of agreement can be used to constrain new physics predictions. The framework tested in this thesis will be the SM Effective Field Theory. The tests will be performed in the different signal regions in order to understand how the sensitivity may vary between the resolved and boosted event selections.

CHAPTER 7

BACKGROUND ESTIMATION

The event selection applied to the data selects a phase space which favours the kinematic properties of the semileptonic $\gamma\gamma \to WW$ process. However, in the signal region, there is a significant contribution from background processes which also satisfy the event selection. It is essential to have a reliable estimation of the background processes in the four different signal regions. With the null-hypothesis of only background processes contributing to the signal region, any deviations to the background-only prediction could be an indication of new physics. Such deviations will be parametrised using the EFT framework to constrain anomalous gauge couplings.

The MC simulations of the various background processes provides a preliminary estimate for the background contributions, however it is not complete. Background processes originating from falsely identified or non-promptly produced particles are not well estimated in current simulations. Therefore the simulation is utilised in conjunction with data-driven methods to provide a robust estimation of the background and reducing the uncertainties. The resolved and boosted channels will estimate background contributions from the electron and muon channels separately as the rate of triggers and detector efficiencies, and sources of misidentified particles differ between the lepton channels.

All background processes in the signal region will be modelled as a single combinatorial background. This is inclusive of backgrounds from the different processes as well as contributions not simulated. Description of the combinatorial background will be presented in Section 7.1. Section 7.2 describes the combinatorial background estimated in the resolved channel. Different data-driven methods are implemented to verify the estimations made. Additionally, validation regions are constructed to determine the accuracy of the background estimation methods. The estimation for the boosted channel is completed in Section 7.3 where similar methods are deployed. Additional validation checks are performed to verify that the method provides a successful description of the

background. Systematic uncertainties originating from the modelling of the background are derived for both channels. Discussion of other systematic uncertainties originating from theoretical and experimental sources are discussed in Section 7.4 along with their impact on the final estimations of the background.

7.1 Combinatorial Background

An event is defined as a *combinatorial background* event when a background process passes the event selection criteria which concerns the ATLAS detector and, simultaneously pileup protons are detected at the A and C side of the AFP detector, passing the AFP kinematic requirements. Figure 7.1 shows schematically how the signal and combinatorial background process differs in the experimental setup. The signal event is shown in Figure 7.1a, where the protons tagged in the forward detector originate from the same vertex as the interaction of the photon-induced process. The combinatorial background event, shown in Figure 7.1b, occurs when protons tagged in the forward detector do not originate from the same interaction vertex reconstructed in the ATLAS detector.

The combinatorial background event includes pileup protons which, coincidentally, match the momentum transfer of the event in the main ATLAS detector. As a result it passes the event selection requirement of $|\xi^{\pm}_{WW} - \xi^{\mathrm{A/C}}_{\mathrm{AFP}}| \leq 0.01$. To verify that this combinatoric relation between the process in the ATLAS detector and the pileup protons in the forward detectors is independent of the background processes, the $\xi^{\mathrm{A/C}}_{\mathrm{AFP}}$ distribution can be compared. Figure 7.2 shows the normalised $\xi^{\mathrm{A}}_{\mathrm{AFP}}$ and $\xi^{\mathrm{C}}_{\mathrm{AFP}}$ distributions after the event selection is applied without the m_{jj} and $|\xi^{\pm}_{WW} - \xi^{\mathrm{A/C}}_{\mathrm{AFP}}|$ requirement. It is shown in this phase space as it is inclusive of the signal region and the later defined control regions. The different simulated background processes have similar distributions, verify that pileup protons are not kinematically correlated to the kinematic process observed in the central detector. Similar distributions are obtained for the muon channel found in Appendix D.1 showing the similarity of the distributions is also independent of the lepton flavour. Therefore, it is assumed that the background in all of these regions can be modelled as one combinatorial background.

As the different background process are independent of the pileup protons, it is assumed that backgrounds originating from misidentified particles will also be independent. Therefore, the estimation of the total background in the signal region, the background can be considered as one total combinatorial background. It is to be determined for the resolved and boosted channels independently.

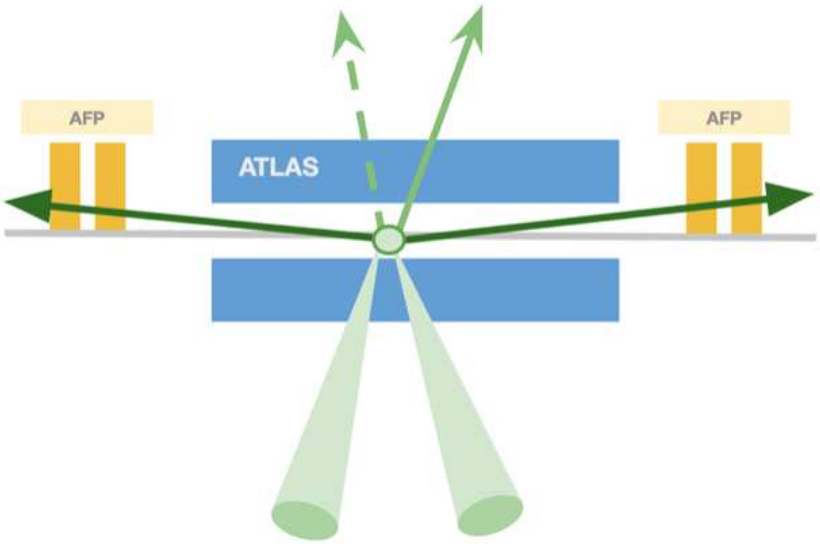

(a) Signal Event

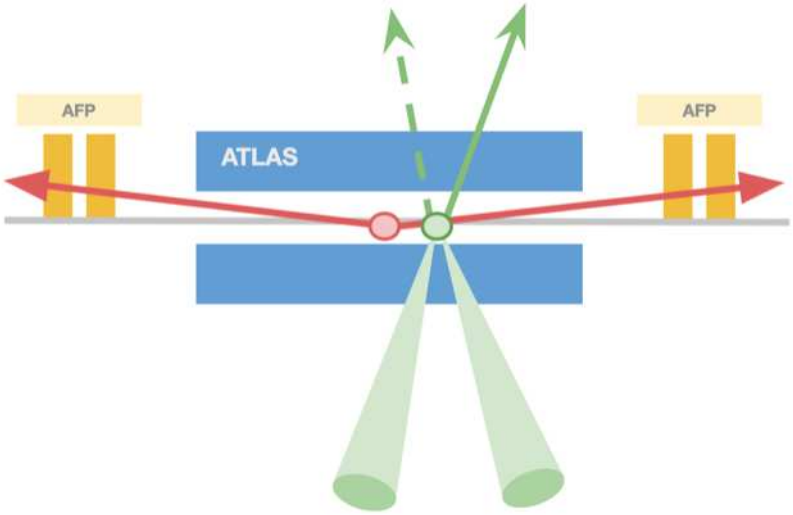

(b) Combinatorial Background Event

Figure 7.1. Schematic of the coincidence of ATLAS detector and tagged protons. A signal event is shown in Figure 7.1a where protons and ATLAS central objects all originate from the same vertex. An example of a combinatorial event shown in Figure 7.1b where the tagged protons do not originate from the same vertex as the central objects.

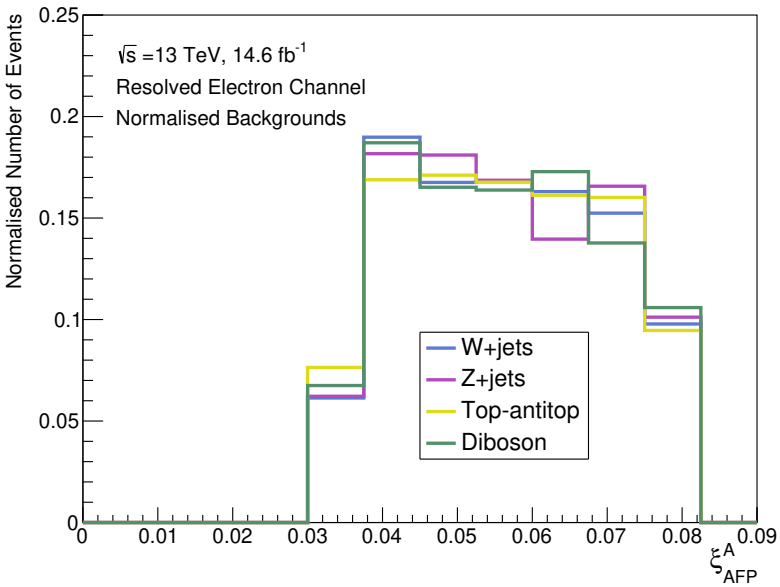

(a)

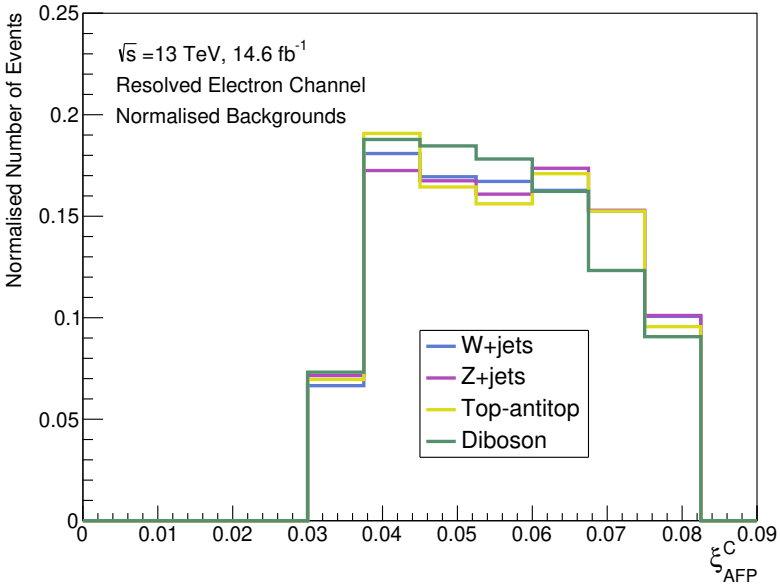

(b)

Figure 7.2. Normalised $\xi_{\mathrm{AFP}}^{\mathrm{A/C}}$ distributions of simulated background processes in the inclusive region where the background estimation is determined. Shown are the distributions for the electron channel on A side (Figure 7.2a) and C side (Figure 7.2b).

7.2 Resolved Channel

The estimation of the combinatorial background in the Signal Region is calculated with the use of control regions. Two kinematic cuts from the event selection presented in Table 6.1 are inverted to define the control regions. Inverting, either one or both of the cuts, the three kinematic control regions are defined. The signal process has negligible contribution in these regions. The control regions are orthogonal to the signal region therefore are not blinded. Both the MC simulations and data in these control regions are taken advantage of to extrapolate the background into the signal region. For the resolved channel, the dijet mass, m_{jj}, and the absolute difference in the fractional energy loss of the WW system and of the forward tagged protons, $|\xi^{\pm}_{WW} - \xi^{\mathrm{A/C}}_{\mathrm{AFP}}|$, are used to construct the regions. The regions are defined as following:

- Signal Region (SR): $m_{jj} \in [50, 100]$ GeV and $|\xi^{\pm}_{WW} - \xi^{\mathrm{A/C}}_{\mathrm{AFP}}| \leq 0.01$
- Control Region 1 (CR1): $m_{jj} \geq 100$ GeV and $|\xi^{\pm}_{WW} - \xi^{\mathrm{A/C}}_{\mathrm{AFP}}| \leq 0.01$
- Control Region 2 (CR2): $m_{jj} \geq 100$ GeV and $|\xi^{\pm}_{WW} - \xi^{\mathrm{A/C}}_{\mathrm{AFP}}| > 0.01$
- Control Region 3 (CR3): $m_{jj} \in [50, 100]$ GeV and $|\xi^{\pm}_{WW} - \xi^{\mathrm{A/C}}_{\mathrm{AFP}}| > 0.01$

which is also illustrated in Figure 7.3. As discussed in Chapter 6, the resolved channel has two signal regions defined as Signal Region A and Signal Region C. The control regions are analogously defined for A and C side and the background estimations are performed independently for each signal region. Constructing the regions in this way ensures that the majority of the signal events enter the signal region than the control regions. Of the three control regions, CR3 has the largest signal contribution, where the signal is less than 5% of the that in the signal region. This is crucial irrespective of the background-dominated nature of this process in the SR with respect to the SM signal, as this region represents a potential vicinity for contributions from SMEFT to arise.

Initially, the control regions are used to validate that the MC simulations describe the SM backgrounds well, by comparing them to the observed data in these regions. This is shown in Figure 7.4 which shows the kinematic distributions in CR1, A side for the electron channel. In Figure 7.4a, the dijet mass distribution is shown with the ratio of the data to simulation which is constant within the uncertainties. For completeness the distribution below 50 GeV is shown, but this region is not included in CR1. Additionally one can see the range where the dijet mass cut is blinded. Similarly in Figure 7.4b the $|\xi^{\pm}_{WW} - \xi^{\mathrm{A/C}}_{\mathrm{AFP}}|$ distribution is shown, with a ratio which is also constant across the kinematic range. As the ratio is similar in values in both distributions, it can be said that the MC simulation in CR1 describes the shape of the data well at the given uncertainty

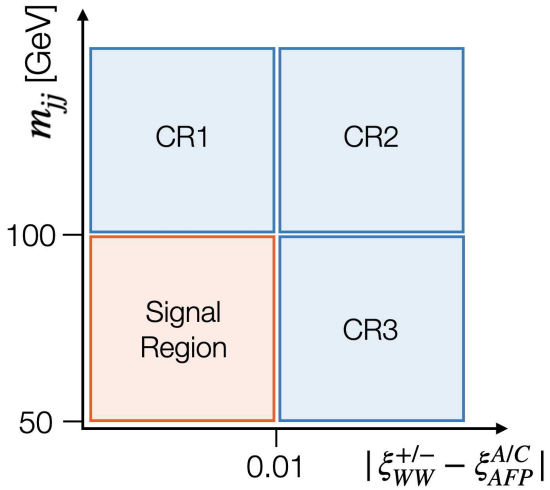

Figure 7.3. Signal region and control regions constructed for the resolved channel. Regions are defined in the kinematic plane of m_{jj} and $|\xi^{\pm}_{WW} - \xi^{\mathrm{A/C}}_{\mathrm{AFP}}|$.

level. However, it does underestimates the data. The offset is due to backgrounds not included in simulations such as misidentified particles.

This level of agreement between the simulations and data is observed for both the electron and muon channels. Distributions of the muon channel for the same control region as that in Figure 7.4b are presented in Appendix D.2. Additionally, the level of agreement is consistent when comparing the three control regions. Presented in Appendix D.3 are the distributions of CR2 and CR3 of the electron channel A side, where a similar constant offset is seen in the ratio of data over MC simulation for the m_{jj} distribution. The differences in the control regions constructed on the A side and C side are very small. An example of this in Appendix D.4 shows CR3 in the electron channel, for A and C side. This is the control region which the largest difference between the two sides but still remains consistent with one another.

With the signal and control regions modelled, the estimation can be make for the background in the signal regions. Two methods are used to estimate the background in this channel, the "ABCD" method and the "Scale Factor" method. The approaches are used to validate each other as well quantify a systematic uncertainty for the modelling.

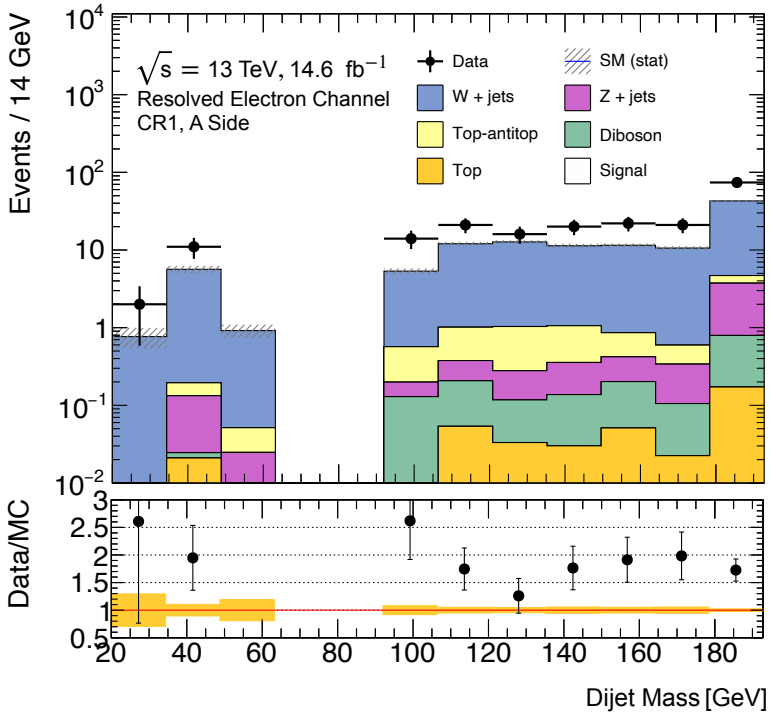

(a)

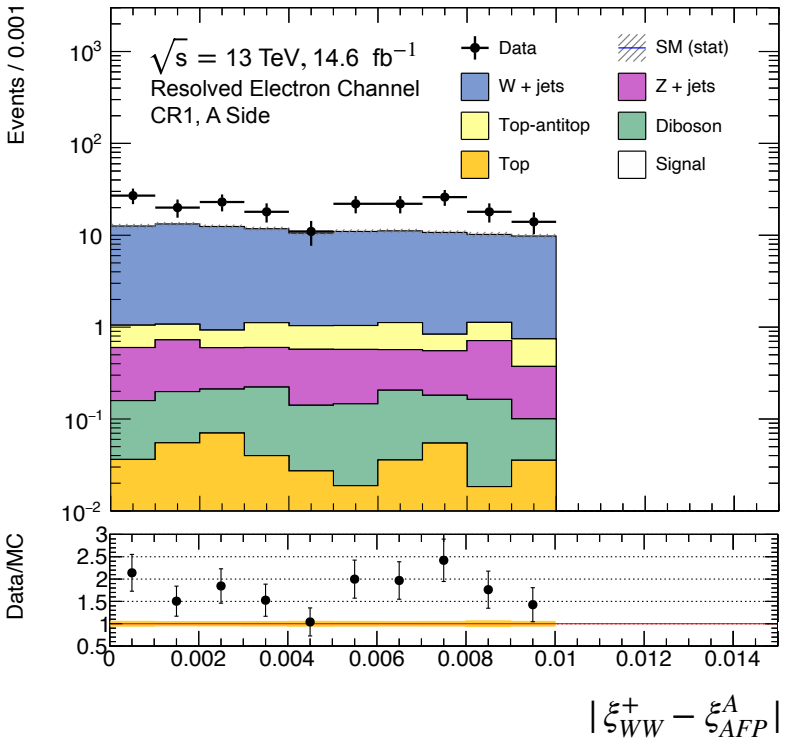

(b)

Figure 7.4. Kinematic distributions of the dijet mass and $|\xi^{\pm}_{WW} - \xi^{\mathrm{A/C}}_{\mathrm{AFP}}|$ in electron channel of CR1 on the A side. The lower panels show the ratio of data and MC simulations. Uncertainties shown are statistical only.

7.2.1 Estimation using ABCD Method

The estimation of the total combinatorial event in the signal region can be performed using the so called "ABCD" Method. This data-driven method uses the data in the control regions to infer the number of background events in the signal region. The underlying assumption of this method is that the following equations holds true for the number of background events

$$\frac{N(\mathrm{SR})}{N(\mathrm{CR1})} = \frac{N(\mathrm{CR3})}{N(\mathrm{CR2})}. \tag{7.1}$$

For this equation to be valid, the two kinematics chosen to define the various regions, m_{jj} and $|\xi^{\pm}_{WW} - \xi^{\mathrm{A/C}}_{\mathrm{AFP}}|$ must be sufficiently uncorrelated. A weak correlation is expected as the ξ_{WW} variable depends on the m_{WW}, as seen in Equation 6.1, and this encapsules the m_{jj} mass term. Consequently, this correlation must be quantified and corrected for in Equation 7.1. This is done with the correction factor R such that,

$$N(\mathrm{SR})^{\mathrm{Bkg}} = R^{\mathrm{MC}} \cdot N(\mathrm{SR})^{\mathrm{Data}}_{\mathrm{ABCD}}, \tag{7.2}$$

$$\text{where} \quad N(\mathrm{SR})^{\mathrm{Data}}_{\mathrm{ABCD}} = \frac{N(\mathrm{CR1})^{\mathrm{Data}} \cdot N(\mathrm{CR3})^{\mathrm{Data}}}{N(\mathrm{CR2})^{\mathrm{Data}}}. \tag{7.3}$$

The R factor is derived from the MC simulations of the background processes as it also requires kinematic information from the blinded signal region. The correlation between m_{jj} and $|\xi^{\pm}_{WW} - \xi^{\mathrm{A/C}}_{\mathrm{AFP}}|$ can be quantified as

$$R^{\mathrm{MC}} = \frac{N(\mathrm{SR})^{\mathrm{MC}} \cdot N(\mathrm{CR2})^{\mathrm{MC}}}{N(\mathrm{CR1})^{\mathrm{MC}} \cdot N(\mathrm{CR3})^{\mathrm{MC}}}. \tag{7.4}$$

An alternative approach is developed to calculate R without use of Equation 7.4. This is because the value of R calculated is subject to fluctuations when the background simulation is repeated. The source of this is due to the random overlaying of pileup protons discussed in Section 5.4. The background event randomly assigns the value of ξ_{AFP} randomly each time the simulation is ran, and this will differ. As a result, there is an ambiguity which arises as to the value of $|\xi^{\pm}_{WW} - \xi^{\mathrm{A/C}}_{\mathrm{AFP}}|$ leading to the same background event being assigned to different control regions. This value can be above or below 0.01, the boundary condition of $|\xi^{\pm}_{WW} - \xi^{\mathrm{A/C}}_{\mathrm{AFP}}|$. This leads to the fluctuation of the value R calculated. Predicting this value iteratively, one can find the value of R which the background simulations converges to. However this is not computationally efficient. To circumvent this, the correlation factor is inferred for the m_{jj} and $\xi^{\pm}_{WW}$ phase space rather than the $|\xi^{\pm}_{WW} - \xi^{\mathrm{A/C}}_{\mathrm{AFP}}|$. Due to the random nature of the pileup protons modelling for backgrounds, and its independence to the central particles reconstructed in the ATLAS

detector, it can be assumed that m_{jj} and $\xi_{\mathrm{AFP}}^{\mathrm{A/C}}$ are not kinematically correlated.

A new phase space is defined in the plane of m_{jj} and $\xi_{WW}^{+/-}$ where the correction factor is calculated. It can be split into new *alternative regions (AR)* used to calculate the level of correlation between the two kinematic variables, as shown in Figure 7.5. The m_{jj} is defined in regions from [50,100) GeV, matching that of the Signal Region and CR3. Then additionally it is split into two regions from [100,170) GeV and greater than 170 GeV. The $\xi_{WW}^{+/-}$ is defined in the range [0.035,0.08], matching that of the event selection. It is split once at $\xi_{WW}^{+/-} = 0.05$, giving in total 6 regions. Theses regions are then used to calculate the correction factor independent of the $\xi_{\mathrm{AFP}}^{\mathrm{A/C}}$. When using information from regions AR3 and AR4, no data is used as this phase space is inclusive of the SR. The choice of splitting the kinematic plane of $m_{jj} > 100$ GeV into four regions, Regions AR1a, AR1b, AR2a and AR2b, provides a kinematic phase space where one can validate the correction factors calculated from MC simulations and those calculated from data.

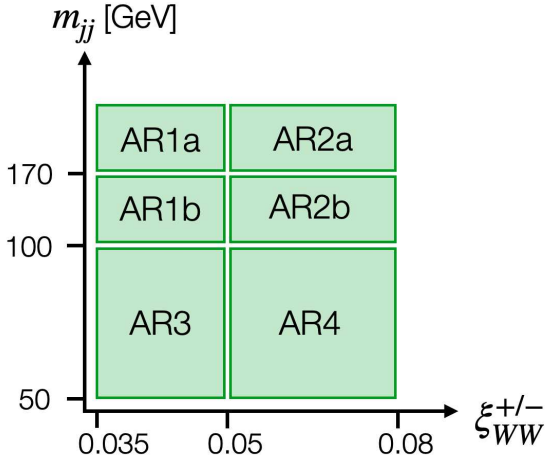

Figure 7.5. Alternative regions defined in the plane of m_{jj} and $\xi_{WW}^{+/-}$ which are utilised for the calculation of correction factors R^{MC}.

The correction factor R^{MC}, which will be used in Equation 7.2, is calculated from the full phase-space shown in Figure 7.5 where regions AR1a+AR1b, similarly AR2a+AR2b, are considered as one region. This is shown in Equation 7.5 where the number of background events inputted is taken from the MC simulation.

$$R^{\mathrm{MC}} = \frac{\Big(N(\mathrm{AR1a})^{\mathrm{MC}} + N(\mathrm{AR1b})^{\mathrm{MC}}\Big) \cdot N(\mathrm{AR4})^{\mathrm{MC}}}{N(\mathrm{AR3})^{\mathrm{MC}} \cdot \Big(N(\mathrm{AR2a})^{\mathrm{MC}} + N(\mathrm{AR2b})^{\mathrm{MC}}\Big)} \tag{7.5}$$

To validate the correction factors calculated, a second correction factor, R' is determined using the region of $m_{jj} > 100$ GeV, defined in Equation 7.6. The R' value can be calculated for both Data and MC as it is orthogonal to the signal region. Equations 7.5

and 7.6 are equivalent and therefore can be used to validate each other.

$$R' = \frac{N(\text{AR1a}) \cdot N(\text{AR2b})}{N(\text{AR1b}) \cdot N(\text{AR2a})} \tag{7.6}$$

Figure 7.6 shows the correction values R and R' calculated using Equations 7.5 and 7.6. It is calculated for the electron and muon channel for both the A and C side regions. The values calculated with MC simulations are shown in the green bands, labeled as the expected values. In black are the values calculated with the number of events observed in the various control regions in data. For all channels, R and R' are consistent with each other, within the uncertainties. For the electron channel, C side, the expected values agree within two standard deviations and consequently considered as reasonable agreement. For the R' values, the expected values from simulation can be compared to the data calculations. They are in agreement within the uncertainty of the data. The correction values derived from data have larger uncertainties due to statistical limitations than that from the MC simulations. The values obtained are close to one which indicates that the m_{jj} and $\xi^{+/-}_{WW}$ only has a small correlation which is corrected for.

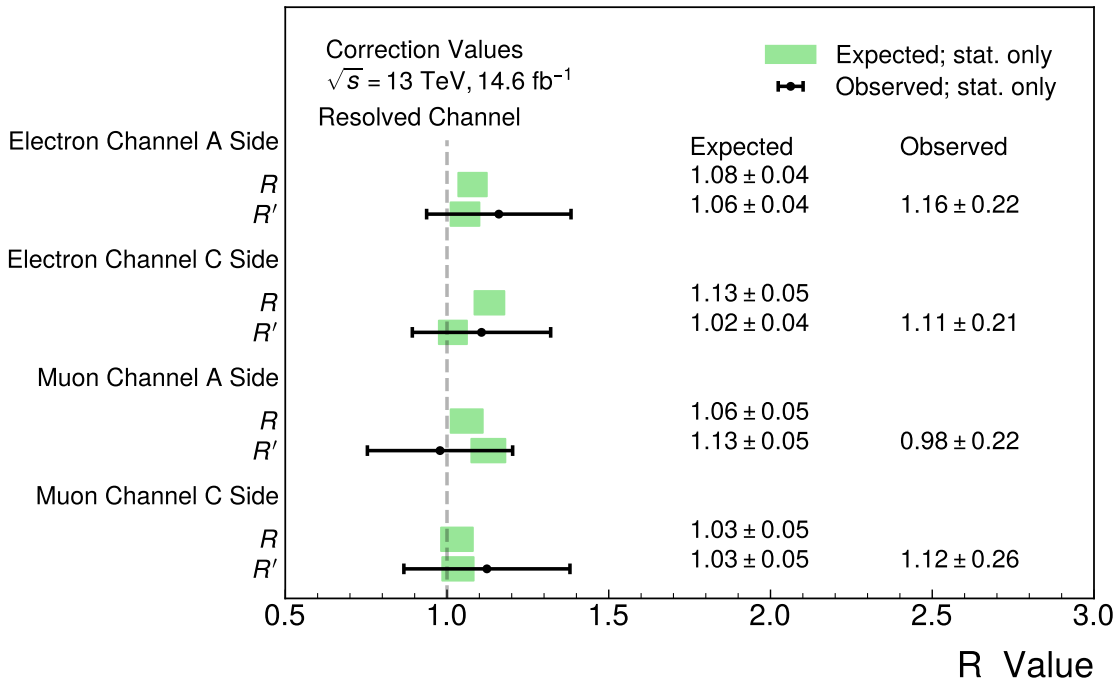

Figure 7.6. Comparison of correction values R obtained for the various channels. Both the values used for the background estimation and the validation are shown. In green are the expected bands calculated using MC simulations. For R' the value derived from data are also shown in the black points, for verification.

The correlation values R^{MC} calculated with Equation 7.5 are used in Equation 7.2. Using the number of events in the data which satisfy the kinematic conditions of the control regions, the total combinatorial background events for the signal regions, for each

lepton flavour channel is calculated. The results are shown in Table 7.1 below. It can be seen that the electron channels have a larger background contribution which is as expected as contributions due to misidentified particles in the detector is larger for electrons than muons. For a given lepton channel, the values are in agreement between A and C side, which is also expected as the rate of background does not systematically favour a side. This prediction has minimal dependence on the MC simulation as this is only used in the constructed of the correction values, R.

Channel	$N(\mathrm{SR})^{\mathrm{Bkg}}$
e, A Side	99.6 ± 13.2
μ, A Side	59.5 ± 9.4
e, C Side	85.0 ± 11.3
μ, C Side	65.0 ± 10.2

Table 7.1. Estimation for number of combinatorial background events using the ABCD Method. Values are provided for electron and muon channels separately. Uncertainties quoted are statistical only.

7.2.2 Estimation using Scale Factors

A second method is used to validate the estimation of the background events shown in Table 7.1. This method constructs *scale factors* which quantify the rescaling of the MC simulation required in order to agree with data. The scale factors account for potential mismodelling or systematic biases in the estimate of simulated background processes. They are constructed independently in each of the control regions, previously defined in Figure 7.3. The scale factors are then used to rescale the MC predictions in the signal region. This is done for each control region providing multiple predictions for the combinatorial background estimation. For CR1, the equation would follow as

$$N(\mathrm{SR})^{\mathrm{Bkg\ Est.}}_{f_{\mathrm{CR1}}} = f_{\mathrm{CR1}} \cdot N(\mathrm{SR})^{\mathrm{MC}} \tag{7.7}$$

where f_{CR1} is the scale factor constructed using CR1. The scale factor is defined as

$$f_{\mathrm{CR1}} = \frac{N(\mathrm{CR1})^{\mathrm{Data}}}{N(\mathrm{CR1})^{\mathrm{MC}}}. \tag{7.8}$$

The same follows for CR2 and CR3. The scale factors are expected to be consistent across the different regions. The values obtained for the three control regions are shown in Table 7.2 below. For the electron channels, the different scale factors are consistent within

the uncertainties. The muon channels are consistent within two standard deviations of the uncertainties.

Channel	f_{CR1}	f_{CR2}	f_{CR3}
e, A Side	1.70 ± 0.13	1.53 ± 0.10	1.74 ± 0.15
μ, A Side	1.23 ± 0.12	1.37 ± 0.10	1.47 ± 0.15
e, C Side	1.62 ± 0.12	1.58 ± 0.10	1.74 ± 0.15
μ, C Side	1.25 ± 0.12	1.35 ± 0.10	1.45 ± 0.15

Table 7.2. Scale factors obtained for each control region for a given channel. Uncertainties quoted are statistical only.

The CR1 and CR3 are closer to the Signal Region, with only one kinematic cut inverted in each region. Therefore, scale factors from these regions are used to predict the background of the signal region using Equation 7.7. Shown in Figure 7.7 are the estimated background obtained for the different channels using f_{CR1} or f_{CR3}. The values obtained from both scale factors are in good agreement, demonstrating the consistency of the scale factor method over different control regions. Also shown are the values obtained with the ABCD method, shown previously in Table 7.1. All three values are consistent with each other over the different channels. The ABCD method is predominantly data driven in its estimation, however has a larger uncertainty as it includes uncertainties from the correction factors, R.

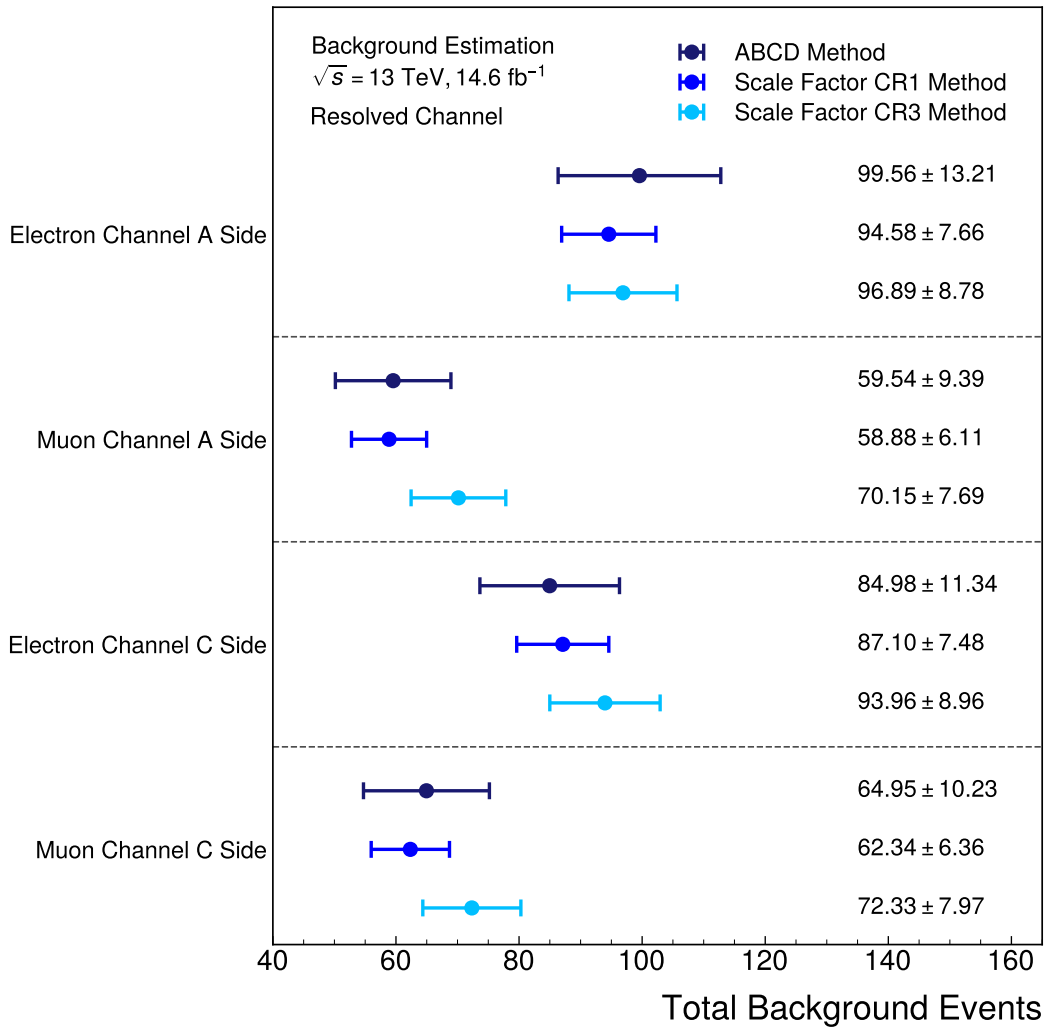

Figure 7.7. Estimations of the total combinatorial background events in the signal region for different channels. Shown are results calculated with the ABCD Method and Scale Factor Method. Results show good agreement between methods. Uncertainties shown are statistical only.

7.2.3 Validation of Estimation

Validation regions (VR) are defined in regions of the phase space that are similar to the nominal control and signal regions in their background composition. These VRs are used to test the robustness of the background estimation method and identify potential systematic biases in the methodology. This in turn provides the opportunity to also quantify a systematic uncertainty on the background estimate, associated to the methodology.

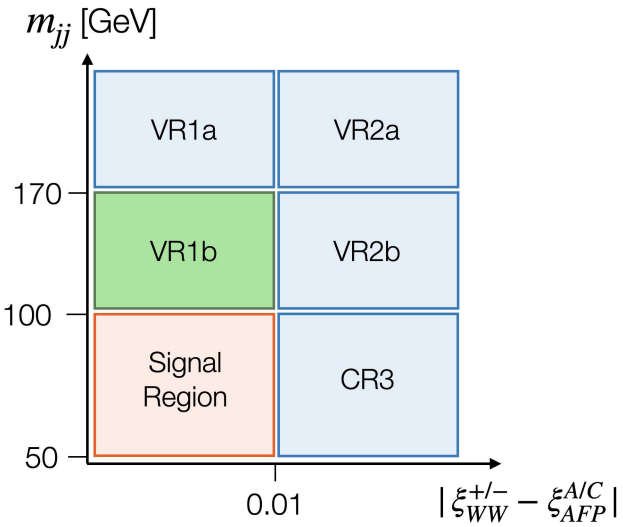

Figure 7.8. Construction of Validation Region in the previously defined CR1 and CR2.

The first validation regions are defined in the direction of the m_{jj} phase space. Figure 7.8 shows the construction of the validation regions from Control Regions 1 and 2 where are split into four regions where CR1 = VR1a + VR1b and CR2 = VR2a + VR2b. The new regions are defined with an m_{jj} cut of 170 GeV. This value is chosen as it ensures sufficient statistics in all validation regions. In Figure 7.8, the VR1b is highlighted in green as this is the region kinematically closest to the signal region. Therefore the neighbouring validation regions are used to estimate VR1b. Using the ABCD method, it is calculated as

$$N(\text{VR1b})^{\text{Bkg}}_{\text{ABCD}} = R^{\text{MC}} \cdot \frac{N(\text{VR1a})^{\text{Data}} \cdot N(\text{VR2b})^{\text{Data}}}{N(\text{VR2a})^{\text{Data}}}, \tag{7.9}$$

where the R^{MC} is taken from Figure 7.6. The event counts in data are used for the neighbouring validation regions, similar to what was done for the nominal estimation.

The second set of validation regions are constructed by further splitting CR2 and CR3 along the $|\xi_{WW}^{\pm} - \xi_{\text{AFP}}^{\text{A/C}}|$ axis where CR2 = VR2c + VR2d and CR3 = VR3a + VR3b. Figure 7.9 shows the how it is defined schematically. The cut of $|\xi_{WW}^{\pm} - \xi_{\text{AFP}}^{\text{A/C}}| < 0.012$ is chosen to ensure the regions are populated with enough events. Highlighted again in green is the VR3a which is the validation region kinematically closest to the signal region

and therefore is the region where the validation is performed. The estimation is then calculated as

$$N(\text{VR3a})^{\text{Bkg}}_{\text{ABCD}} = R^{\text{MC}} \cdot \frac{N(\text{VR3b})^{\text{Data}} \cdot N(\text{VR2c})^{\text{Data}}}{N(\text{VR2d})^{\text{Data}}}. \tag{7.10}$$

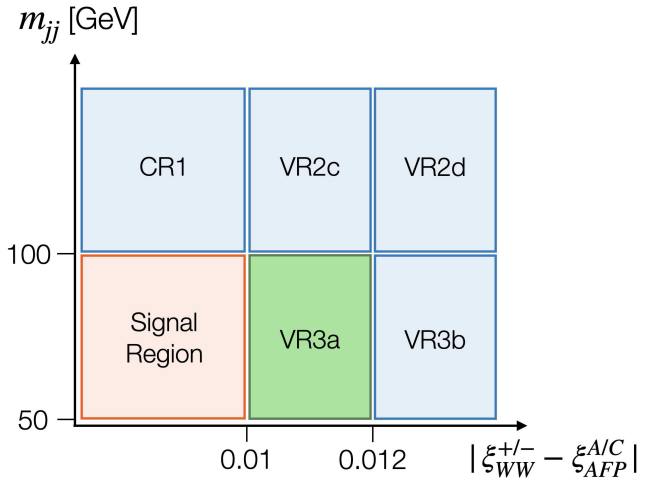

Figure 7.9. Construction of Validation Region in the previously defined CR2 and CR3.

Using Equations 7.9 and 7.10, the validation regions are estimated and compared to the observed event counts. The results are shown in Figure 7.10 which shows the estimation for the number of background events in VR1b and VR3a for each lepton channel separately and also for the A and C side. It can be seen that the N(VR1b) expected from the background estimate is consistent with that of the observed value in the electron channels, both A and C side, and in the Muon A side. For the Muon C side, the agreement is within two standard deviations. It has a larger discrepancy due to a downward fluctuation in the data. For VR3a it is similarly seen that the estimation of the background is in good agreement with the observed data for the electron channel. Both muon channels have a larger discrepancy but still are in agreement within the uncertainties. As the Muon A side expectation underestimates what is observed, and the Muon C side overestimates the observed data, it indicates that this is not a systematic bias but rather a result of statistical fluctuations in the muon channels for VR3a.

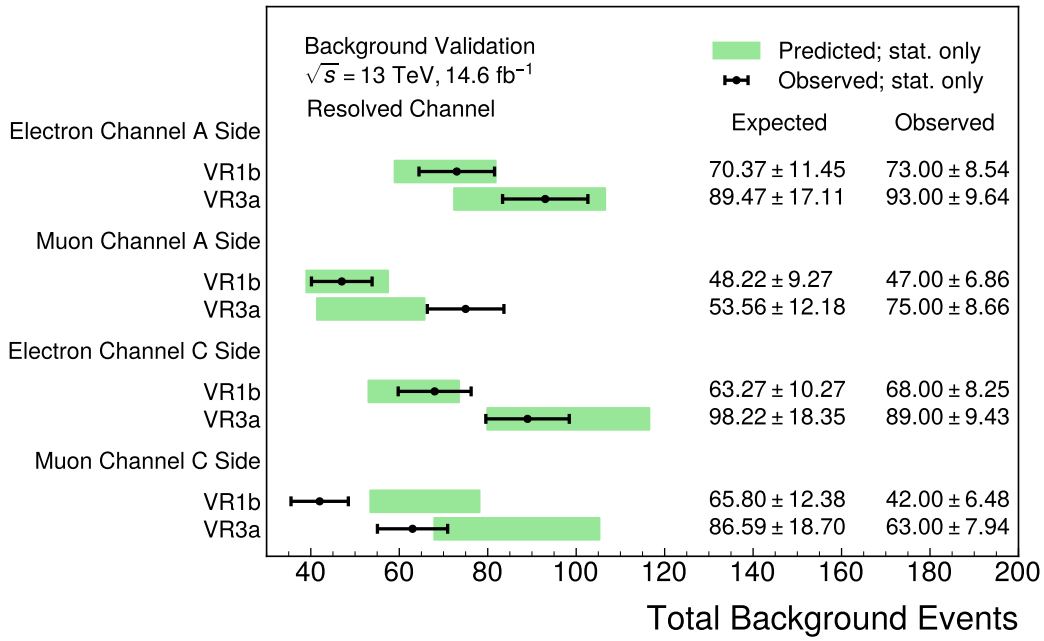

Figure 7.10. Results of validation tests performed in VR1a and VR3a to predict combinatorial background events. In green are the values predicted using the ABCD method, compared to the observed values in data for a given validation region.

7.2.4 Results with Modelling Systematic Uncertainties

Figure 7.10 shows that the background estimation is better modelled in VR1b than VR3a. Therefore the CR1, which only inverts the m_{jj} kinematic requirement, will be a more accurate model of the background estimation in the signal region. The deviation of the ABCD method from the results of the Scale Factor method using CR1 is therefore assigned as a systematic uncertainty. Quoted in Table 7.3 are the systematic uncertainties derived, with the nominal and statistical uncertainties.

Channel	$N(\mathrm{SR})^{\mathrm{Bkg}}$
e, A Side	$99.6 \pm 13.2 \pm 5.0$
μ, A Side	$59.5 \pm 9.4 \pm 0.7$
e, C Side	$85.0 \pm 11.3 \pm 2.1$
μ, C Side	$65.0 \pm 10.2 \pm 2.6$

Table 7.3. Estimation for number of combinatorial background events using the ABCD Method. Values are provided for electron and muon channels separately. Uncertainties quoted are first statistical and second systematic.

With the estimations made for the electron and muon channels, they can now be added to arrive at the total combinatorial background in the Signal Region on the A side and C side. The total number of combinatorial background events estimated in the Signal region A side and C side with statistical and systematic uncertainties are quoted

below with the electron and muon channels summed in quadrature.

$$\text{A Side:} \quad 159.11 \pm 16.21 \text{ (stat.)} \pm 5.03 \text{ (sys.)} \tag{7.11}$$

$$\text{C Side:} \quad 149.93 \pm 15.27 \text{ (stat.)} \pm 3.37 \text{ (sys.)} \tag{7.12}$$

7.3 Boosted Channel

Both the scale factor method and ABCD method models the background in the resolved channel well and are compatible with one another. For the boosted channel, the scale factor method is used to estimate the total combinatorial background in the boosted channel as it is previously provided estimates with smaller statistical uncertainties. Once again, one must define control regions by inverting kinematic cuts. Previously the mass of the dijet system was used, however in this channel, the event selection is such that the majority of events are in the mass range of the boosted jet. Consequently, inverting this cut leads to control regions with low statistics as it does not reject many events. Another kinematic variable chosen, the p_{T} of the leading lepton. This is used with the absolute difference in the energy loss of the WW system and energy loss of the forward tagged protons, $|\xi^{\pm}_{WW} - \xi^{\mathrm{A/C}}_{\mathrm{AFP}}|$. The regions constructed in the boosted channel are defined as the following:

- Signal Region (SR): Leading lepton $p_{\mathrm{T}} > 100$ GeV and $|\xi^{\pm}_{WW} - \xi^{\mathrm{A/C}}_{\mathrm{AFP}}| \leq 0.01$
- Control Region 1 (CR1): Leading lepton $p_{\mathrm{T}} > 100$ GeV and $|\xi^{\pm}_{WW} - \xi^{\mathrm{A/C}}_{\mathrm{AFP}}| > 0.01$
- Control Region 2 (CR2): Leading lepton $p_{\mathrm{T}} \leq 100$ GeV and $|\xi^{\pm}_{WW} - \xi^{\mathrm{A/C}}_{\mathrm{AFP}}| > 0.01$
- Control Region 3 (CR3): Leading lepton $p_{\mathrm{T}} \leq 100$ GeV and $|\xi^{\pm}_{WW} - \xi^{\mathrm{A/C}}_{\mathrm{AFP}}| \leq 0.01$,

also shown schematically in Figure 7.11. The control regions have very low signal contributions hence one can verify that the data follows the background-only model. Figure 7.12a shows CR1 for the leading lepton p_{T} distribution and Figure 7.12b shows the $|\xi^{\pm}_{WW} - \xi^{\mathrm{A/C}}_{\mathrm{AFP}}|$ for electron channel A side. The lower panels show the ratio of data over simulation. The values are approximately constant over both kinematic observables, further motivating the use of the scale factor method. Again the offset in the ratio from unity is understood as the simulation not accurately modelling events originating from misidentified particles not included in the simulation which are present in the data. For the boosted channel, the estimation of the combinatorial background is completed using only the Scale Factor method only. The resolved channel is a proof of concept that this method is in good agreement with the ABCD method which is more extensive.

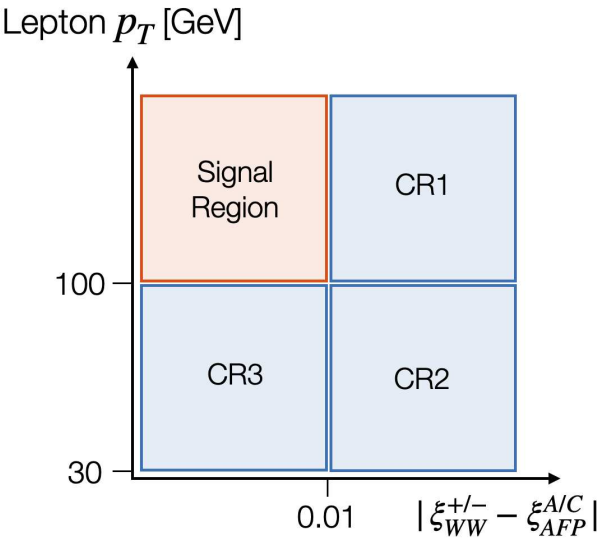

Figure 7.11. Signal region and control regions defined for the boosted channel. Regions are defined in the kinematic place of leading lepton p_{T} and $|\xi^{\pm}_{WW} - \xi^{\mathrm{A/C}}_{\mathrm{AFP}}|$.

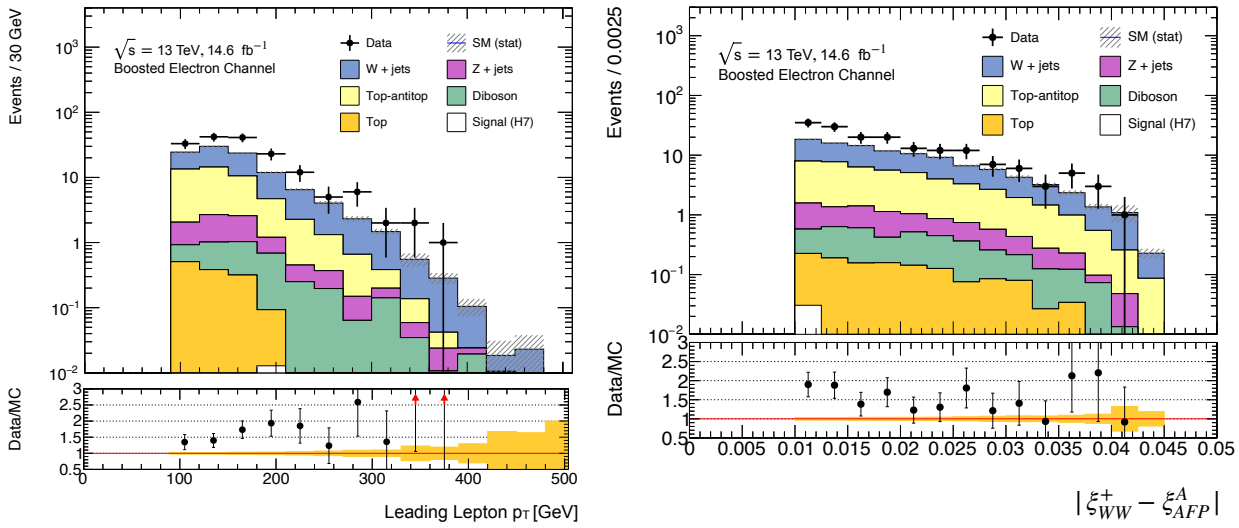

(a) (b)

Figure 7.12. Distributions of the leading lepton p_{T} and $|\xi^{\pm}_{WW} - \xi^{\mathrm{A/C}}_{\mathrm{AFP}}|$ in electron channel of CR1 on the A side. Shown in the lower panels are the ratio of Data over MC simulations. Uncertainties shown are statistical only.

7.3.1 Estimation using Scale Factors

The scale factors are calculated using Equation 7.8 for each control region. It is done in all three control regions to ensure the background modelling is consistent with the different combinations of kinematic cuts being satisfied. The scale factors for the boosted control regions are shown in Table 7.4. The values are consistent with one another for a given channel, and additionally between channels of the same lepton type. As expected, the scale factors are larger for electron channels than muon channels.

These scale factors are then applied to the MC simulation prediction of the background

Channel	f_{CR1}	f_{CR2}	f_{CR3}
e, A Side	1.59 ± 0.12	1.50 ± 0.10	1.48 ± 0.10
μ, A Side	1.29 ± 0.14	1.31 ± 0.11	1.37 ± 0.11
e, C Side	1.55 ± 0.12	1.44 ± 0.10	1.55 ± 0.10
μ, C Side	1.24 ± 0.14	1.35 ± 0.11	1.32 ± 0.11

Table 7.4. Scale factors obtained for each boosted control region for a given lepton channel. Uncertainties quoted are statistical only.

events in the signal region, as shown in Equation 7.7. The results are shown in Figure 7.13 where all three scale factors are tested to predict the number of background events in the signal region. As the scale factors were consistent, by design the background prediction are also consistent with each other. This indicates that the prediction is robust over all control regions.

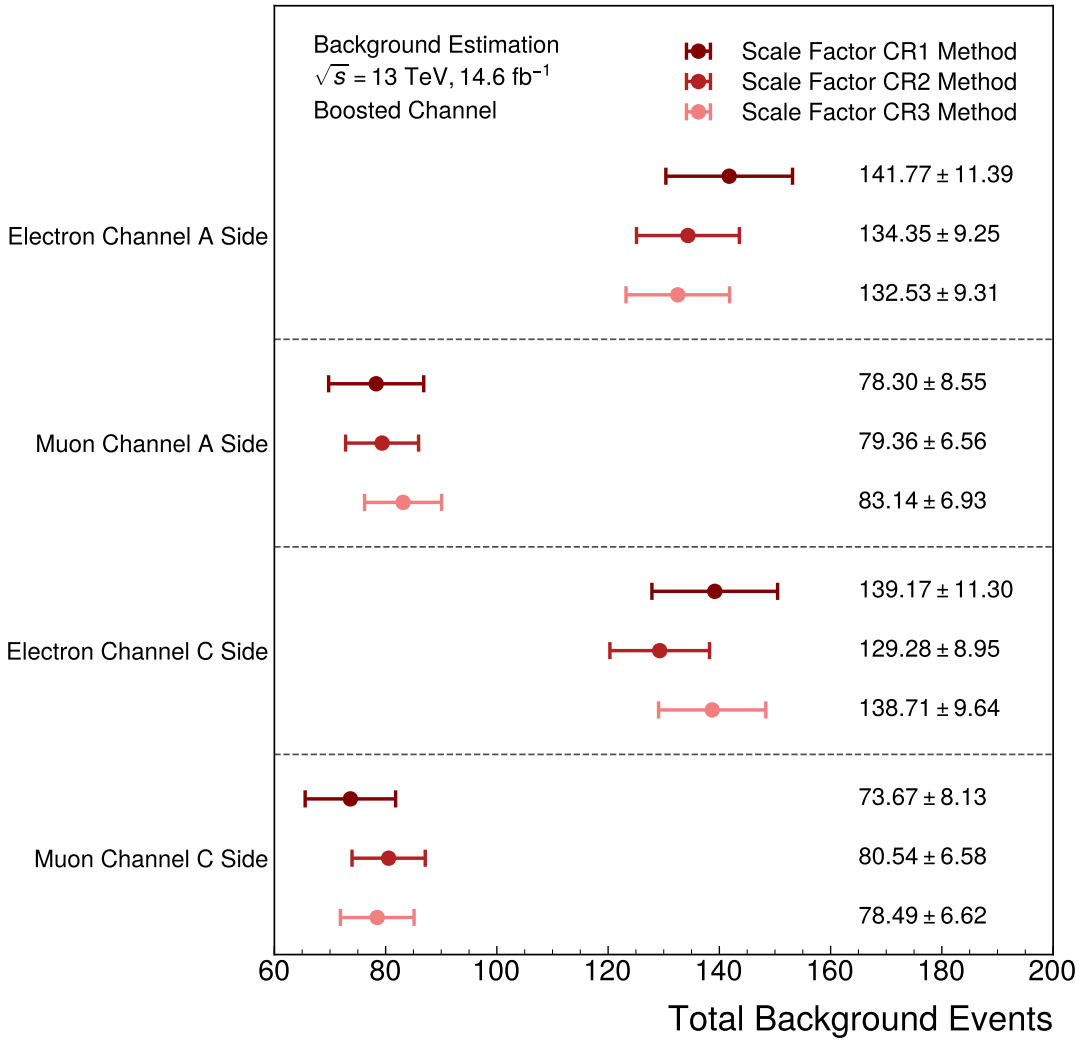

Figure 7.13. Comparison background estimated in the signal region using scale factors from different control regions. Uncertainties shown are statistical only.

7.3.2 Validation of Scale Factor Method

Validation of the estimations with the scale factor method can be done by constructing validation regions in the control regions. The scale factors are calculated in one validation region and then extrapolated to the other. Figure 7.14a shows how the validation regions are constructed within CR1 and CR3. The kinematic cut of leading lepton p_{T} at 80 GeV and $|\xi^{\pm}_{WW} - \xi^{\mathrm{A/C}}_{\mathrm{AFP}}|$ at 0.012 is chosen such that the number of events in the respective regions have sufficient statistics. Validation regions within CR2 are equidistant from the signal region if split by the leading lepton p_{T} or the $|\xi^{\pm}_{WW} - \xi^{\mathrm{A/C}}_{\mathrm{AFP}}|$. The validation is performed with both possible splittings in this region to ensure the validation is unbiased by this choice, as shown in Figure 7.14b and 7.14c. For a given control region, the validation region in blue is used to construct the scale factor, and is applied to the simulated prediction of the neighbouring region. The regions tested are chosen as they are kinematically closer to the signal region, highlighted in yellow.

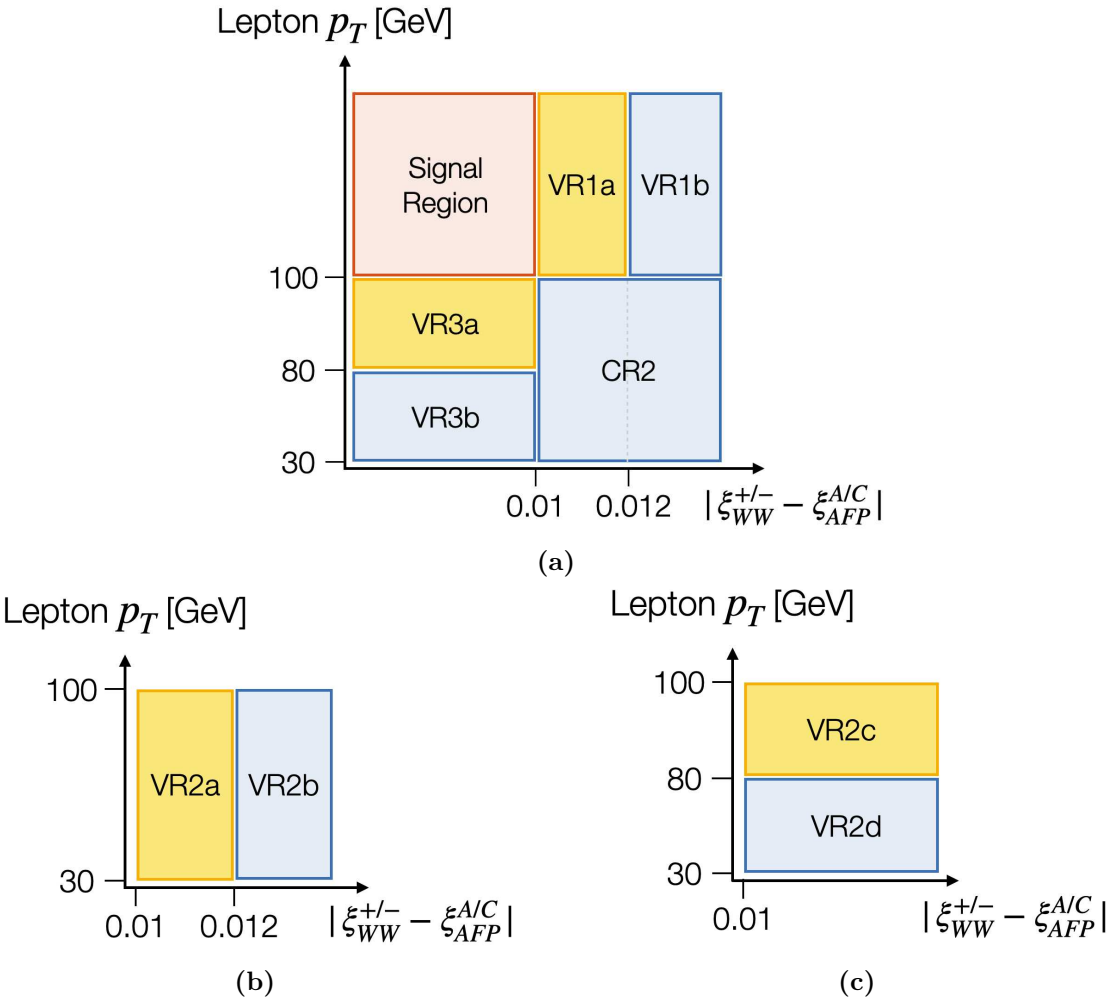

Figure 7.14. Validation regions defined for the boosted channel. Regions are constructed within each of the control regions, for CR1 and CR3 shown in Figure 7.14a. The CR2 has two configurations for validation shown in Figure 7.14b and Figure 7.14c.

The estimation of the validation regions highlighted in Figure 7.14 and the observed values in data for these regions are shown in Figure 7.15. The results for all channels are shown. For the majority of the channels, agreement within one standard deviation between the data and the estimation of the backgrounds found. The electron and muon channel on the A side both see a weaker agreement of the VR1a where the prediction under predicts the data. This is only observed on the A side hence is not a systematic which needs to be accounted for.

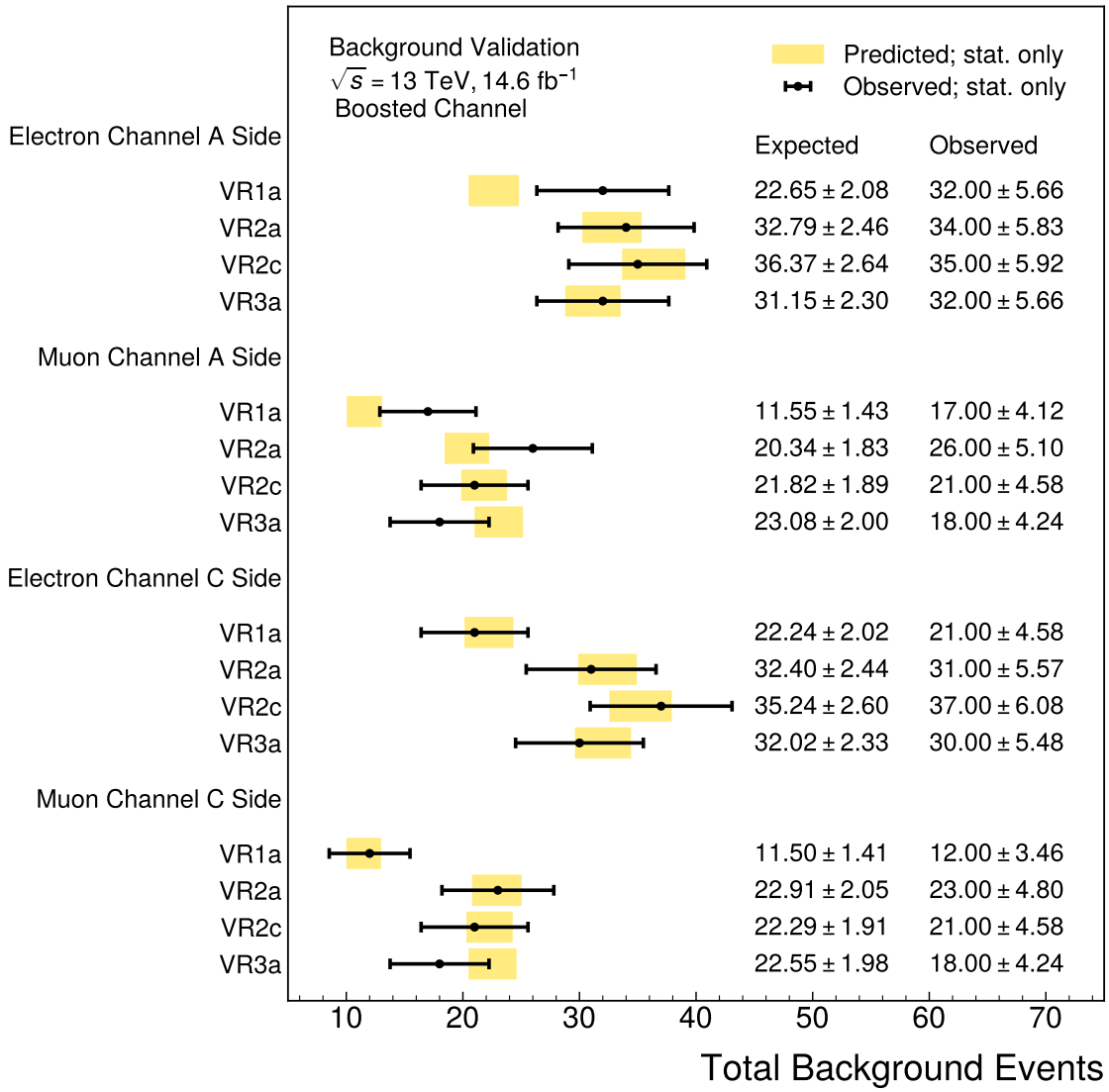

Figure 7.15. Results of the validation of the boosted channel in various validation regions. Estimations are shown in the yellow bands, with the data in black points. Uncertainties quoted are statistical only.

7.3.3 Results with Modelling Systematic Uncertainties

To quantify the systematic uncertainty originating from the modelling used to estimate the total combinatorial background. The validation results presented in Figure 7.15 are used to determine the uncertainty. The estimation using scale factors of CR3 are used as the nominal value.

Estimations made with scale factors from CR2 are used as the systematic variation. The difference between the estimates determined with CR2 and CR3 scale factors is quantified as the systematic uncertainty. The CR2 is used as the validation shown in Figure 7.15 shows good agreement across all channels. This is not the case for CR1 as the validations performed using VR1a show weaker agreement and is not consistent across all the channels. Combining the results of the electron and muon channels, the total combinatorial background for the A side and C side signal region can be calculated for the boosted channel. The values with the statistical and systematic uncertainties are quoted below.

$$\text{A Side:} \quad 215.67 \pm 9.49 \text{ (stat.)} \pm 4.20 \text{ (sys.)} \tag{7.13}$$

$$\text{C Side:} \quad 217.20 \pm 11.69 \text{ (stat.)} \pm 9.65 \text{ (sys.)} \tag{7.14}$$

7.4 Systematic Uncertainties

The systematic uncertainties considered for the estimation of the combinatorial background concern the modelling. Additional systematic uncertainties can be associated with the estimation, both experimental and theoretical in their origin. These uncertainties impact the event yields obtained from MC simulations of the background processes used in the estimations. Therefore the impact of varying the MC yields must be considered. This section will briefly discuss the level of impact of these additional uncertainties and why they can be omitted from the estimation.

Resolved Channel

In the estimation of the background for the resolved channel, the ABCD method uses simulations to estimate the correction factor R. This value accounts for kinematic correlations between the m_{jj} and $\xi^{\pm}_{WW}$, defined in Equation 7.5. This is the only stage in the nominal estimation where MC simulations are used. The uncertainties will impact the full m_{jj}, $\xi^{\pm}_{WW}$ phase space and therefore vary the event yields in the previously defined Alternative Regions. On assumption that this variation is independent of the two kine-

matic variables, it is expected that the uncertainties will cancel out, thus having minimal impact on the estimation of R. Moreover, the main parameter which impacts the value of the estimation in the ABCD method is Equation 7.3. This which is determined from data and therefore when accounting for potential deviations to R impacting Equation 7.2, it is not expected that systematic uncertainties have a large impact on the value estimated.

The dominant background process in the resolved channel is the production of W bosons in association with jets. Taken from the analysis of this process at the ATLAS experiment, found in Ref. [113], the largest experimental uncertainty originates from the JES. This has an impact of 9% on the event yields for events where the jet multiplicity is more than one. This uncertainty does not have more than 2% variation over the range of the jet p_{T}, up to 800 GeV. Given the dijet mass range in which the regions are defined in, it is expected this uncertainty varies uniformly across the regions. Therefore has neglibible impact on varying the value of R. The main theoretical uncertainty comes from the choice of generator used to model the matrix element and the hadronisation. The studies presented in Ref. [113] show this uncertainty is only significant at high jet multiplicities as one becomes more sensitive to which hadronisation model is used account for initial and final state radiation and the higher order corrections. As only two high energy jets are required for the resolved channel, this uncertainty can be omitted. Therefore the estimation of the background in the resolved channel has a neglibible impact from experimental and theoretical uncertainties.

Boosted Channel

The nominal method used for the estimation of the combinatorial background for the boosted channel is the Scale Factor method. The MC simulations of the background processes are used in constructing the scale factors and providing the estimate of simulated event yields in the signal regions. Once again, one can take advantage of the simulations being in a ratio where the relative contributions from theoretical and experimental systematic uncertainties can potential cancel out. This is apparent when looking at Equations 7.7 and 7.8, the simulation of the event yields $N(\mathrm{SR})^{\mathrm{MC}}$ and $N(\mathrm{CR1})^{\mathrm{MC}}$ will both vary due to the additional uncertainties considered.

The two processes in the background simulation of the boosted channel are the production of W+jets and top pair production. As discussed for the resolved channel, the experimental and theoretical uncertainties of the W+jets process are not expected to impact the estimation of the background. Similar to W+jets, the largest experimental uncertainty in top pair production originates from the JES. Taken from Ref. [114], the JES has an impact of 4% to the event yields. This uncertainty would impact both the signal and control region similarly and therefore is expected to have a negligible impact

on the estimation of the background. The dominant theoretical background in top pair production also originates from the modelling and the variations in the event yields estimated by different hadronisation models. The theoretical uncertainty as an impact of 3% to the event yields [115]. Therefore it is not expected that the experimental and theoretical variations will have a large impact on the estimation of the background in the boosted channel.

CHAPTER 8

RESULTS AND EFFECTIVE FIELD THEORY INTERPRETATION

The semileptonic $\gamma\gamma \to WW$ process can be tested against the null hypothesis of predicting only SM background events in the signal regions. It is tested against the observed number of events to quantify the level of agreement with the SM in Section 8.1. The results of this study are then further tested to understand the sensitivity that may arise due to New Physics models. In Section 8.2, limits on the SMEFT Wilson coefficients [116] are derived and provide an insight into how successfully the $\gamma\gamma \to WW$ process can be used to constrain New Physics parameters. Alternative approach to constraining the parameters are explored in order to further optimise the limits set on the Wilson coefficients, in Section 8.3.

8.1 Results

The analysis provides an estimate for the total combinatorial background in the various signal regions. Under the assumption that the SM holds true and hence no new physics arises in the data, it is expected that the data observed in the SR is in agreement with the background estimation. Table 8.1 presents the estimate of the background found in Chapter 7 along with the observed number of events in the SRs. The observation is well described by the background-only model with agreement within one standard deviation, in each SR. It is consistent with the SM and no significant excess or anomaly is present in the data for the SRs. Given that no significant deviation from the SM prediction is observed, the result can be used to constrain new physics predictions. A well-motivated framework to test for new physics which arise via modifications to the SM couplings is the Standard Model Effective Field Theory (SMEFT). Sensitivity to the SMEFT can be interpreted from models and its prediction for the SR.

Signal Region	Background Estimate	Observed Data
Resolved A Side	159.11 ± 16.97	164
Resolved C Side	149.93 ± 15.64	165
Boosted A Side	215.67 ± 10.38	216
Boosted C Side	217.20 ± 15.16	222

Table 8.1. Estimation of background in signal regions and observed number of events in data for the respective regions. Uncertainties on the background estimate are the statistical and systematic uncertainties combined.

8.2 EFT Interpretation

The $\mathrm{SU(2)_L \times U(1)_Y}$ symmetry of the SM electroweak sector, being non-Abelian, leads to self-interactions among gauge bosons in both triple and quartic forms. The $\gamma\gamma \to WW$ process is sensitive to both the SM triple (γWW) and quartic ($\gamma\gamma WW$) coupling. Therefore deviations to the interactions via potential New Physics (NP) modifying the couplings can be measured via this process. Parametrisation of these deviations can be defined using the SMEFT formalism, which is used in this thesis. The SMEFT adds higher dimensional operators to the SM Lagrangian modifying it as:

$$\mathscr{L}_{\mathrm{EFT}} = \mathscr{L}_{\mathrm{SM}} + \mathscr{L}^{(6)} + \mathscr{L}^{(8)} + \ldots \quad . \tag{8.1}$$

The $\gamma\gamma \to WW$ process has sensitivity to both the dimension 6 and dimension 8 modifications to the SM. The additional dimensions are defined as:

$$\mathscr{L}^{(6)} = \sum_{i=1} \frac{c_i^6}{\Lambda^2} \mathscr{O}_i^6 \quad \text{and} \quad \mathscr{L}^{(8)} = \sum_{i=1} \frac{c_i^8}{\Lambda^4} \mathscr{O}_i^8, \tag{8.2}$$

where c_i are the Wilson coefficients which are scaled by the energy scale, Λ. The energy scale defines an upper limit for which the SMEFT holds without violation of unitarity and of which beyond defines a phase space where NP can be present. For dimension 6, the process is sensitive to 9 operators: $\mathscr{O}_W^6$, $\mathscr{O}_{HW}^6$, $\mathscr{O}_{HB}^6$, $\mathscr{O}_{HWB}^6$, $\mathscr{O}_{Hq3}^6$, $\mathscr{O}_{Hl3}^6$, $\mathscr{O}_{ll1}^6$, $\mathscr{O}_{H\Box}^6$, $\mathscr{O}_{HDD}^6$, which are all CP even [36]. In dimension 8, there are mixed and transverse operators of which the semileptonic $\gamma\gamma \to WW$ process has sensitivity to 15 of these operators. The mixed fields are constructed from two field strength tensors and two Higgs derivatives. The process has sensitivity to 7 mixed operators, $\mathscr{O}_{M,i}^8$ where $i \in \{0, 1, 2, 3, 4, 5, 7\}$. The $\mathscr{O}_{M,6}$ is omitted from the list as $\mathscr{O}_{M,6} = \frac{1}{2} \cdot \mathscr{O}_{M,0}$. The transverse fields are constructed from four fields strength tensors [37]. There are 8 transverse operators, $\mathscr{O}_{T,j}^8$ where $j \in \{0, 1, 2, 3, 4, 5, 6, 7\}$ which the process has sensitivity to. The operators are constructed as functions of SM fields and are defined in Appendix E.1 for both dimensions.

8.2.1 Decomposition Method & Sensitivity Scans

To study the sensitivity to SMEFT operators, a *decomposition method* is used. It splits the matrix elements of the SMEFT model into three components, the SM contributions, purely SMEFT contributions and an interference term of the SM with SMEFT contributions. The amplitudes are expanded for a given SMEFT operator as:

$$|A|^2 = |A_{\text{SM}} + c_i A_i|^2 = |A_{\text{SM}}|^2 + \underbrace{2c_i \cdot \text{Re}(A_{\text{SM}} A_i)}_{\text{Linear}} + \underbrace{c_i^2 |A_i|^2}_{\text{Quadratic}} + \underbrace{2c_i c_j \cdot \text{Re}(A_i A_j)}_{\text{Cross term}}, \quad (8.3)$$

for a given Wilson coefficient c_i. The interference term is known as the *linear* term. The SMEFT contribution is labelled as the *quadratic* term. The *cross term* accounts for interference effects between two different operators. For the SMEFT interpretation made in this thesis, the sensitivity of each operator is studied independently. Therefore this term is set to zero. This method is utilised as the computational requirements to simulate the linear and quadratic terms is much smaller than computing the sum of the amplitudes. The SMEFT simulations are generated in `Madgraph5_aMC@NLO2.8.1` [108] at LO in QCD. The underlying event is modelled with `Pythia8` [109] and the parton showering with the `CT14QED` PDF set [117]. The NP effects from dimension 6 are included with the Warsaw basis using the model found in Ref. [116] and the dimension 8 effects are incorporated with the Eboli model [118]. For each operator studied, the linear and quadratic simulations are produced. The energy scale is set $\Lambda = 1$ TeV and the coefficients of the SMEFT operators are set to unity.

To understand the level of sensitivity of the semileptonic $\gamma\gamma \to WW$ process to the SMEFT operators, the generator-level cross sections for the operators are presented in Table 8.2, prior to the full event selection. For comparison, the SM process has a generator cross section of 0.03 pb. For dimension 6, only $\mathcal{O}_W^6$ is quoted as it is the operator which the process is most sensitive to. The cross section of this operator is orders of magnitude smaller than that in dimension 8. This is due to the dimension 8 operators impacting the quartic coupling only which modifies the complete scattering amplitude. The dimension 6 only modifies one of the γWW vertex which suppresses the contribution. This motivates the choice of focusing on constraining the Wilson coefficients of the dimension 8 operators in this thesis. The cross sections of the other dimension 6 operators can be found in Appendix E.2. The quadratic terms have larger cross sections than the linear terms. This is expected as the quadratic term is a purely SMEFT contribution and is not suppressed by the smaller SM cross section term.

Operator	Linear Cross Section [pb]	Quadratic Cross Section [pb]
Dimension 6 Operators		
$\mathcal{O}_W^6$	-1.1×10^{-1}	1.2×10^{0}
Dimension 8 Operators		
$\mathcal{O}_{M,0}^8$	-6.7×10^{-2}	$+3.5 \times 10^{3}$
$\mathcal{O}_{M,1}^8$	-2.1×10^{-2}	$+2.3 \times 10^{2}$
$\mathcal{O}_{M,2}^8$	-4.4×10^{-1}	$+1.5 \times 10^{5}$
$\mathcal{O}_{M,3}^8$	$+3.6 \times 10^{-1}$	$+9.8 \times 10^{3}$
$\mathcal{O}_{M,4}^8$	-6.0×10^{-2}	$+1.1 \times 10^{4}$
$\mathcal{O}_{M,5}^8$	-2.0×10^{-1}	$+3.0 \times 10^{3}$
$\mathcal{O}_{M,7}^8$	$+1.0 \times 10^{-1}$	$+5.7 \times 10^{1}$
$\mathcal{O}_{T,0}^8$	$+5.6 \times 10^{0}$	$+1.9 \times 10^{5}$
$\mathcal{O}_{T,1}^8$	$+1.8 \times 10^{0}$	$+2.7 \times 10^{4}$
$\mathcal{O}_{T,2}^8$	$+2.6 \times 10^{0}$	$+1.5 \times 10^{4}$
$\mathcal{O}_{T,3}^8$	$+2.5 \times 10^{0}$	$+9.5 \times 10^{3}$
$\mathcal{O}_{T,4}^8$	$+8.1 \times 10^{0}$	$+1.0 \times 10^{5}$
$\mathcal{O}_{T,5}^8$	$+1.8 \times 10^{1}$	$+2.0 \times 10^{6}$
$\mathcal{O}_{T,6}^8$	$+5.8 \times 10^{0}$	$+2.9 \times 10^{5}$
$\mathcal{O}_{T,7}^8$	$+8.4 \times 10^{0}$	$+1.6 \times 10^{5}$

Table 8.2. Total generator cross section for dimension 8 mixed and transverse operators to which can be probed with the $\gamma\gamma \to WW$ process. The dimension 6 operator which the $\gamma\gamma \to WW$ process has the largest sensitivity is also quoted. The Wilson coefficients are set to unity and the NP scale is chosen as $\Lambda = 1$ TeV.

A *Rivet* routine [119] is implemented to understand the sensitivity of the SMEFT processes when loose kinematic cuts are applied. Kinematic distributions of the linear and quadratic components produced using the $\mathcal{O}_{T,5}^8$ operator are shown in Figure 8.1 with the SM term overlaid. This operator has the largest total generator cross section and therefore differences between the SM, linear and quadratic terms will be most prominent. The transverse momentum of the leading jet is shown in Figure 8.1a. The SM term drops at high transverse momentum of the leading jet. Above 300 GeV, the linear term dominates over the SM. However after 600 GeV the quadratic contributions also dominate over the linear components. This is expected as the cross sections of the SMEFT components are larger and therefore predict a harder transverse momentum distribution. For other operators the same kinematic behavior towards high energies is found.

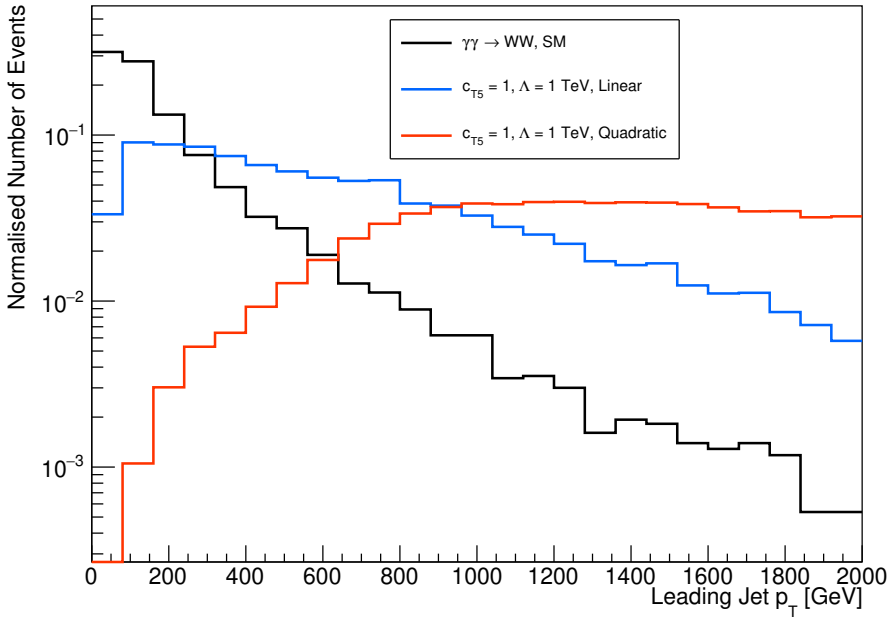

(a)

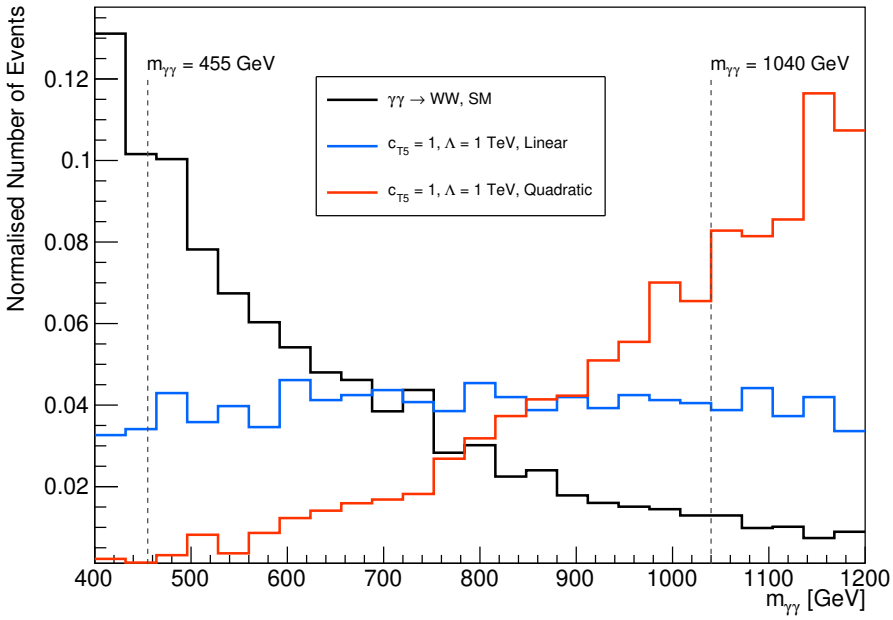

(b)

Figure 8.1. Normalised generator level distributions of the leading jet p_{T} and mass of protons m_{pp}. Shown are the SM, linear and quadratic distributions obtained with $\mathcal{O}_{T,5}$ operator with the coupling coefficient $c_{\mathrm{T},5}$ and energy scale Λ set to unity.

Figure 8.1b shows the mass of the protons transferred to the WW system. This is inferred from the fractional energy loss of the protons where $m_{\gamma\gamma} = \sqrt{s \cdot \xi^{\mathrm{A}}_{\mathrm{AFP}} \cdot \xi^{\mathrm{C}}_{\mathrm{AFP}}}$. Marked on the figure is the mass acceptance of the AFP detector from 455 GeV to 1040 GeV. This mass acceptance comes from the experimental acceptance of the frac-

tional energy loss $\xi_{\text{AFP}}^{\text{A/C}}$ of the AFP detector, as discussed in Chapter 4. Within this mass range, both the linear and quadratic terms dominate over the SM distribution at high mass values. This especially highlights that within the experimental acceptance of the forward detectors, the sensitivity to contributions from EFT operators is achieved with the forward detectors. The distributions of the forward proton fractional energy loss, ξ_{AFP} for the SM, linear and quadratic terms can be found in Appendix E.3.

8.2.2 Statistical Methodology

Constraints on the *coupling coefficients* of the dimension 8 operators are calculated using a statistical fitting procedure. The coupling coefficients are c_i/Λ^4 where c_i are the Wilson coefficients, scaled by the NP energy scale chosen, Λ. The energy scale is fixed when constraining the coupling coefficients and can be translated to different energy scales with this scaling. Predictions of the operators are determined for each operator independently. This is because new physics may only modify a subset of the operators or even just one operator, not all simultaneously. As the SMEFT does not assume a specific NP model beyond the energy scale, the treatment of the operators independently provides limits which conservatively cover different potential NP models. Thus the exclusion limits are determined for one coupling coefficient at a time while the others are assumed to be zero.

A profile likelihood ratio scan is used to construct the confidence intervals making use of the predictions and measured cross sections while also considering the respective uncertainties. The predictions for cross section can be calculated as the sum of the SM expectation and the reconstructed EFT contributions in terms of the linear and quadratic components. The prediction $\boldsymbol{x}_{c_i}^{\text{pred}}$ for a given operator i is

$$\begin{aligned}\boldsymbol{x}_{c_i}^{\text{pred}} &= \sigma_{\text{SM}} \times \prod_j (1 + \boldsymbol{\theta}_j^{\text{SM}}) \\ &+ \sigma_i^{\text{linear}} \frac{c_i}{\Lambda^4} \times \prod_j (1 + \boldsymbol{\theta}_j^{\text{lin}}) \\ &+ \sigma_i^{\text{quad}} \left(\frac{c_i}{\Lambda^4}\right)^2 \times \prod_j (1 + \boldsymbol{\theta}_j^{\text{quad}}),\end{aligned} \tag{8.4}$$

where $\boldsymbol{\theta}_n \in \{\theta_0,\ \theta_1, ...,\ \theta_n\}$ contains the n relative uncertainties on the cross sections predicted. The cross sections of the linear (σ_i^{linear}) and quadratic (σ_i^{quad}) components of the EFT contributions are determined from applying the same event selection as that discussed in Chapter 6 to the EFT simulations. The prediction is constructed for the signal regions, once in a frequentist manner, however in Section 8.3, the prediction is made for each bin of a kinematic distribution.

With the prediction $\boldsymbol{x}_{c_i}^{\text{pred}}$ the likelihood function can be constructed as the following:

$$\mathscr{L}(\boldsymbol{x}_{c_i}^{\text{meas.}}|c_i,\boldsymbol{\theta}) = \text{Poisson}(\boldsymbol{x}_{c_i}^{\text{meas.}}|\boldsymbol{x}_{c_i}^{\text{pred.}}) \times \prod_j \prod_k (G(\boldsymbol{\theta}_{\boldsymbol{j}}^{\boldsymbol{k}})). \tag{8.5}$$

Gaussian fluctuations are included as nuisance parameters which quantify variations due to the different systematic uncertainties, $\boldsymbol{\theta}_{\boldsymbol{n}}^{\boldsymbol{k}}$ of each component of the prediction, where $k \in \{\text{SM, lin, quad}\}$. Sources of systematic uncertainties are only taken into account if their impact is at least 10%. The profile likelihood ratio [120] is constructed for the confidence interval estimation. It is defined as

$$\lambda(c_i) = \frac{\mathscr{L}(c_i, \hat{\hat{\theta}})}{\mathscr{L}(\hat{c}_i, \hat{\theta})}. \tag{8.6}$$

It is constructed from the maximum of the likelihood, obtained at fixed value of c_i, with $\hat{\hat{\theta}}$ and the absolute maximum of the likelihood, determined at $\hat{c}_i$ and $\hat{\theta}$. The test statistic, q, is then determined from the negative log of the likelihood ratio [121] shown in Equation 8.6 where

$$q = -2\ \ln(\lambda(c_i)). \tag{8.7}$$

The confidence intervals are determined using Wilk's theorem [122], assuming that the profile likelihood test statistic is χ^2 distributed. All values of c_i which satisfy the requirement of $q \leq \Delta_\alpha$ constructs the confidence interval. For values of c_i which satisfy the condition with $\Delta_\alpha = 1.00$ construct the range of values which satisfy a 68% confidence interval. Similarly, values of c_i which satisfy the condition for $\Delta_\alpha = 3.84$ satisfy the 95% confidence interval. Having both an upper and lower limit for the coefficients is essential as the SMEFT predicts both positive and negative cross sections and therefore can have both positive or negative coefficients.

8.2.3 Systematic Uncertainties

The relative systematic uncertainties included in the likelihood fit are determined separately for the SM and EFT components. The uncertainties considered in the SM term, $\boldsymbol{\theta}_{\boldsymbol{n}_{\text{SM}}}^{\text{SM}}$, are only from the methodology of the background estimation. As discussed in Chapter 7, the systematic uncertainties from experimental sources can be neglected as the method is predominantly data driven The experimental uncertainties are considered for the linear and quadratic EFT predictions ($\boldsymbol{\theta}_{\boldsymbol{n}_{\text{lin}}}^{\text{lin}}$ and $\boldsymbol{\theta}_{\boldsymbol{n}_{\text{quad}}}^{\text{quad}}$) on reconstruction level. The theoretical uncertainties of the EFT simulations are neglected as the interaction is photon-induced and therefore uncertainties from items such as α_s and PDFs do not impact the EFT signal simulation.

A brief description of the different experimental uncertainties are discussed in this section with the relative uncertainties on the event yields quoted in Table 8.3. Only

uncertainties quoted in Table 8.3 above 10% are considered in the likelihood fit for the EFT event yields. The same relative uncertainties are applied for the event yields of both the linear and quadratic terms.

Systematic	**Uncertainty (%)**
Luminosity	1.1
Pileup	3.0
Forward Proton	8.0
Electrons	1.0
Muons	< 1.0
MET	1.7
Resolved Small-R Jets	21.0
Boosted Large-R Jets	10.0

Table 8.3. Summary of relative experimental systematic uncertainties on the event yields of the linear and quadratic EFT simulated signal simulations.

Luminosity: The luminosity uncertainty, taken from Ref [123], is determined using van der Meer beam separation scans during dedicated running periods in each year. It is then extrapolated to the physics data-taking periods in conjunction to measurements taken with the LUCID detector which is sensitive to the luminosity.

Pileup: The MC simulations are reweighted to match the number of average interactions per bunch crossing and the number of reconstructed primary vertices in an event. The residual difference between what is simulated and the pileup observed in the data quantifies the systematic of the pileup. The relative uncertainty of 3% is taken as a conservative estimate from the ATLAS $V\gamma$ measurement where $V = W^{\pm}, Z$ which decays via the hadronic channel [124]. The decay of the hadronic boson is analysed as a boosted jet, similarly to that performed in this thesis.

Forward Protons: The relative forward proton systematic uncertainties are taken from the ATLAS $\gamma\gamma \to ll$ analysis using AFP [125]. Each AFP systematic, previously defined in Section 4.8, was derived independently on the signal simulation without any variation on the central lepton objects for the same dataset used in this thesis. Therefore similar values of the systematic uncertainties are expected for the EFT simulations of the $\gamma\gamma WW$ process as these uncertainties are independent of the objects produced in the photon-induced process. The largest uncertainty of 6%, on the forward protons originates from the global alignment of the Roman Pot stations, accounting for the position of the detector with respect to the beam. The beam optics provides the subdominant systematic on forward protons of 5%. The track reconstruction uncertainties are derived individually when varying the cluster and track requirements. This contribution is less than a percent

and therefore has a negligible impact. The uncertainty quoted in Table 8.3 is the global alignment, beam optic and track reconstruction uncertainties summed in quadrature.

Small Radius Jets ($R = 0.4$): The main systematic uncertainty which impact the jets originate from the jet energy scale (JES) and jet energy resolution (JER). The JES and JER are derived using both MC simulations and in-situ methods to determine the jet response [126], explained in more detail in Chapter 4. The JES systematic uncertainties are determined by applying nuisance parameters in the calculation of the jet response. The nuisance parameters consider the detector, modelling, statistical and mixed components in the calculation. Additionally uncertainties are applied to quantify how the flavour (quark and gluon) of jets, pileup mitigating step of the JES calibration and η intercalibration impact the response. Typically, each source of uncertainty is varied independently and the summed quadrature of the various uncertainties provides the JES systematic uncertainty. For this analysis the JES is taken from Ref. [126], of 5% for jets of $p_{\mathrm{T}} > 20$ GeV. The $\gamma\gamma \to WW$ requires the jets of $p_{\mathrm{T}} > 25$ GeV for the resolved channel and therefore is a conservative estimate of the JES. The largest component which contributes to this uncertainty comes from the flavour of jets which covers the different calorimeter response for quark and gluon initiated jets. The JER systematic uncertainty is derived from the differences in data and simulation of the dijet events in the determination of the JER with nuisance parameters applied to vary the detector response. The value of this systematic uncertainty is taken from Ref. [124] as 20% for jets of $p_{\mathrm{T}} = 20$ GeV. The uncertainty quoted in Table 8.3 contains both the JES and JER.

Large Radius Jets ($R = 1.0$): The large radius jets also have an associated JES and JER uncertainty which are determined by adding nuissance paramters to vary different stages of the calibration. Jets in the boosted channel require a $p_{\mathrm{T}} > 200$ GeV and therefore the higher energy requirement helps reduce uncertainties on JES and JER as the calorimeter has better performance at high energies [126]. The JES is taken as 2% and JER as 1.5%, taken from Ref. [84] where the jet has the same requirements as that of the boosted event selection, $p_{\mathrm{T}} > 200$ GeV and $|\eta| < 2.5$. In the reconstruction and calibration of large radius jets, the mass is also used. Therefore an associated uncertainty of the jet mass scale (JMS) is also used. The JMS uncertainty is between 2-10%, increasing for higher p_{T} jets [84]. A conservative estimate of 10% for the JMS is considered in this analysis. The total uncertainty is quoted in Table 8.3.

Leptons: In the particle reconstruction of leptons, the reconstruction, identification and isolation components have associated uncertainties. The impact on the lepton kinematics when varying these components provides the systematic uncertainty on the leptons measured [127, 128]. The energy, momentum scale and resolution uncertainties originate from the lepton calibrations, impacting the p_{T} of the lepton. Charge identification is neglibible for the muon channel as the muons are constructed with the muon

detectors in addition to the tracker and calorimeters. Misidentified electrons occur due to early bremsstrahlung upon interaction with the detector material. The photon produced may later decay into an electron-positron pair. It spreads the energy of the cluster and therefore can change which track, and therefore the charge associated to the topocluster is associated with [127]. All the uncertainties discussed are included in the total lepton uncertainties. Values are taken from the measurement of WZ and WW [129, 130] where both searches have a leptonically decaying W boson, similar to this thesis. The uncertainty due to the leptons impacting the event yield correspond to 1% due electron uncertainties and 0.7% for muons.

MET: The systematic uncertainties associated to missing transverse energy originates from the soft track component in the construction of the MET [131]. This component has uncertainties associated to the scale and resolution of the soft track term. Taken from the WW [130] measurement, the MET uncertainty is taken as 1.7%. This is a more conservative estimate to that estimated in the WZ search where 0.2% is found.

8.2.4 Expected and Observed Limits

Using the methodology described in Section 8.2.2, non-unitarised limits on the different EFT operators are calculated for the expected and observed number of events. For each signal region a single-bin analysis is performed to set the limits. Figure 8.2 shows the distribution of the test statistic defined in Equation 8.7 scanned over a range of values for the coupling coefficient $c_{T,5}/\Lambda^4$. The test statistic corresponding to the confidence levels for a 68% and 95% are marked, showing the confidence interval where it intersects with the distribution. The obtained confidence interval for the coefficient of the $\mathcal{O}_{T,5}$ operator is $[-159.2, 151.0] \times \Lambda^4$.

Similar distributions are obtained for the expected and observed intervals in all signal regions, providing the confidence intervals of each coefficient tested. For all operators, the results of the confidence intervals can be found in Appendix E.4. Highlighted in this section are the coefficients best constrained via the $\gamma\gamma \to WW$ process, which are $c_{M,2}/\Lambda^4$, $c_{M,4}/\Lambda^4$ and $c_{T,5}/\Lambda^4$. Expected confidence interval are derived by replacing the observed datasets with Asimov dataset which correspond to the nominal background prediction. Values for signal regions on both A and C side are shown for the resolved and boosted channel. The exception is the $c_{M,4}/\Lambda^4$, where for the resolved channel, only the A side limits are shown, and for the boosted channel only the C side limits. These two limits are omitted from the discussion as the limits are very large with respect to the other side. This is due to large statistical uncertainties in the contributions of the EFT components which leads to the Gaussian nuisance parameters being pulled significantly.

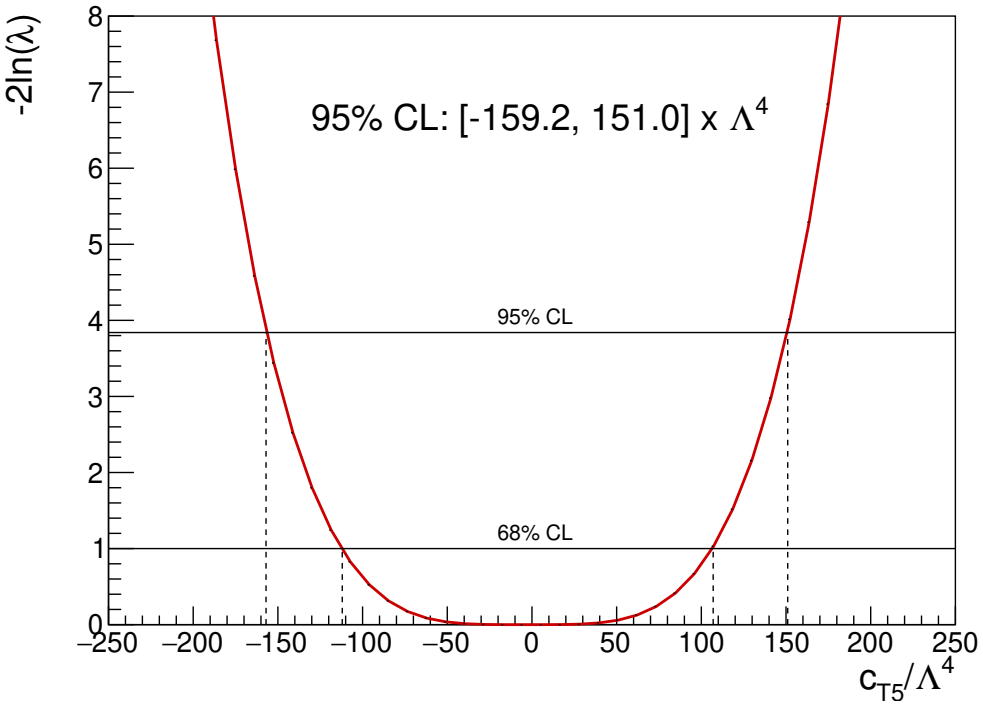

Figure 8.2. Test statistic q as a function of the $c_{T,5}/\Lambda^4$ coefficient. The horizontal lines indicate the value of the test statistic for which values of the coefficient below this are in the confidence interval. Both the 68% and 95% confidence levels are shown.

Figure 8.3 shows the limits set in the resolved channel. The confidence intervals observed are generally in good agreement with the expected limits, however it can be seen that they are not symmetric between the lower and upper limits. This is due to the statistical limitation of this channel. This becomes more apparent when looking at the confidence interval of the $c_{M,4}/\Lambda^4$ operator as the limits are more asymmetric. For the $c_{M,2}/\Lambda^4$ and $c_{T,5}/\Lambda^4$ the A side sets more stringent limits. This is due to the expected background in the SR being closer to that observed in data.

Figure 8.4 shows the confidence intervals obtained for the boosted channel. The aforementioned issues with the asymmetric intervals are no longer present as the statistical uncertainties are lower when in the boosted channel. For this channel, it is seen that the A side also observes more stringent limits for the $c_{M,2}/\Lambda^4$ and $c_{T,5}/\Lambda^4$ operators. Again this is due to the data observed and the SM prediction having better agreement on the A side than the C side. The advantage of the higher statistics in the boosted channel can also be noted as the confidence intervals found are more symmetric. For all the limits set on coefficients in the boosted channel, they are weaker than that in the resolved channel. This is due to a larger background contribution in the signal region, and additionally a closer agreement of the data to the background model in the boosted channel compared to the resolved, which in turn, weakens the limits one can set.

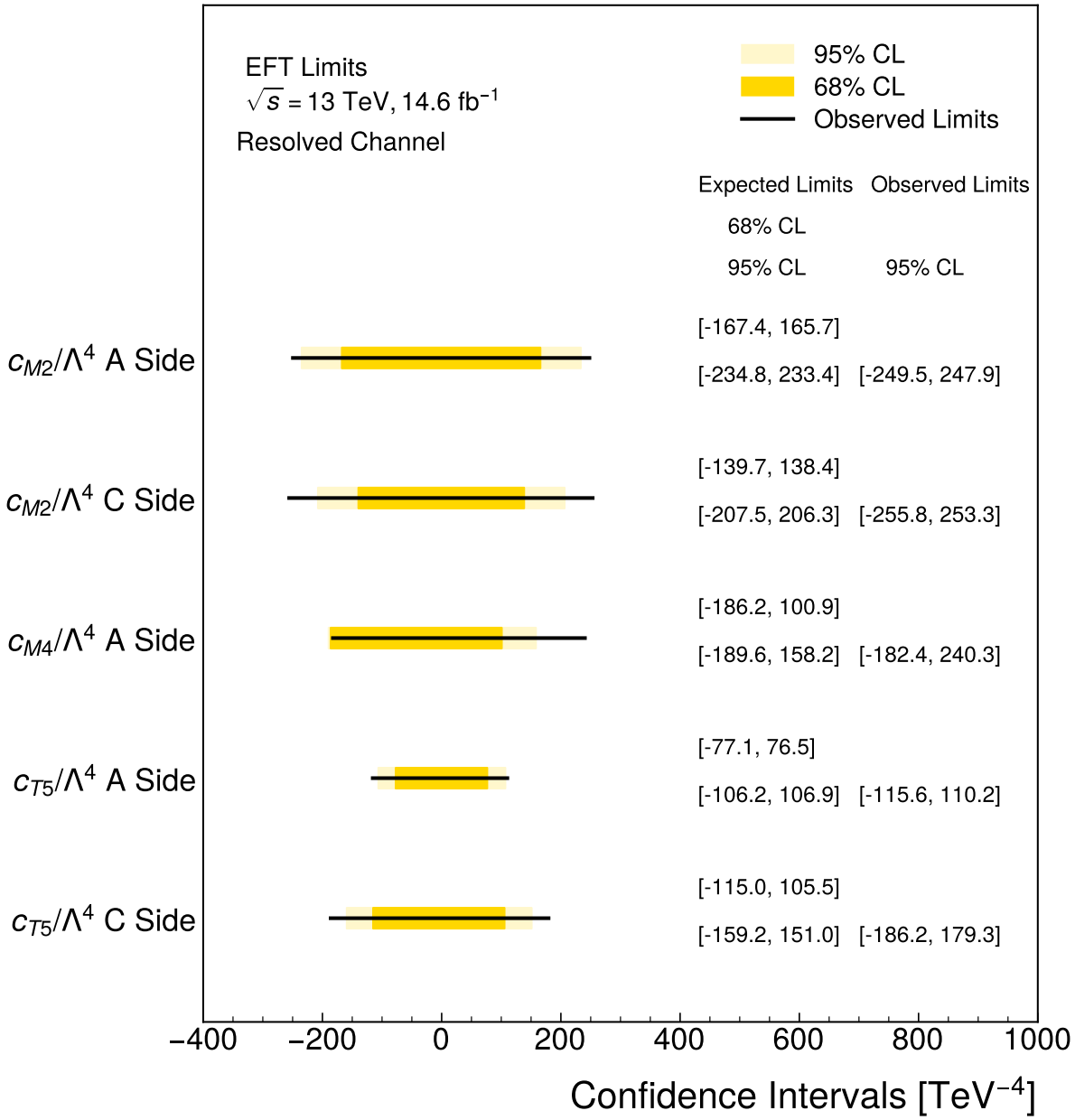

Figure 8.3. The expected and observed limits in the *resolved channels* on the anomalous coupling coefficients of dimension 8 operators. Shown are the $c_{M,2}/\Lambda^4$, $c_{M,4}/\Lambda^4$ and $c_{T,5}/\Lambda^4$ coefficients for the signal regions on the A and C side. Indicated in dark yellow are the expected limits at a 68% confidence level and in light yellow the 95% confidence level. The observed limits at a 95% confidence level are shown as a solid black line.

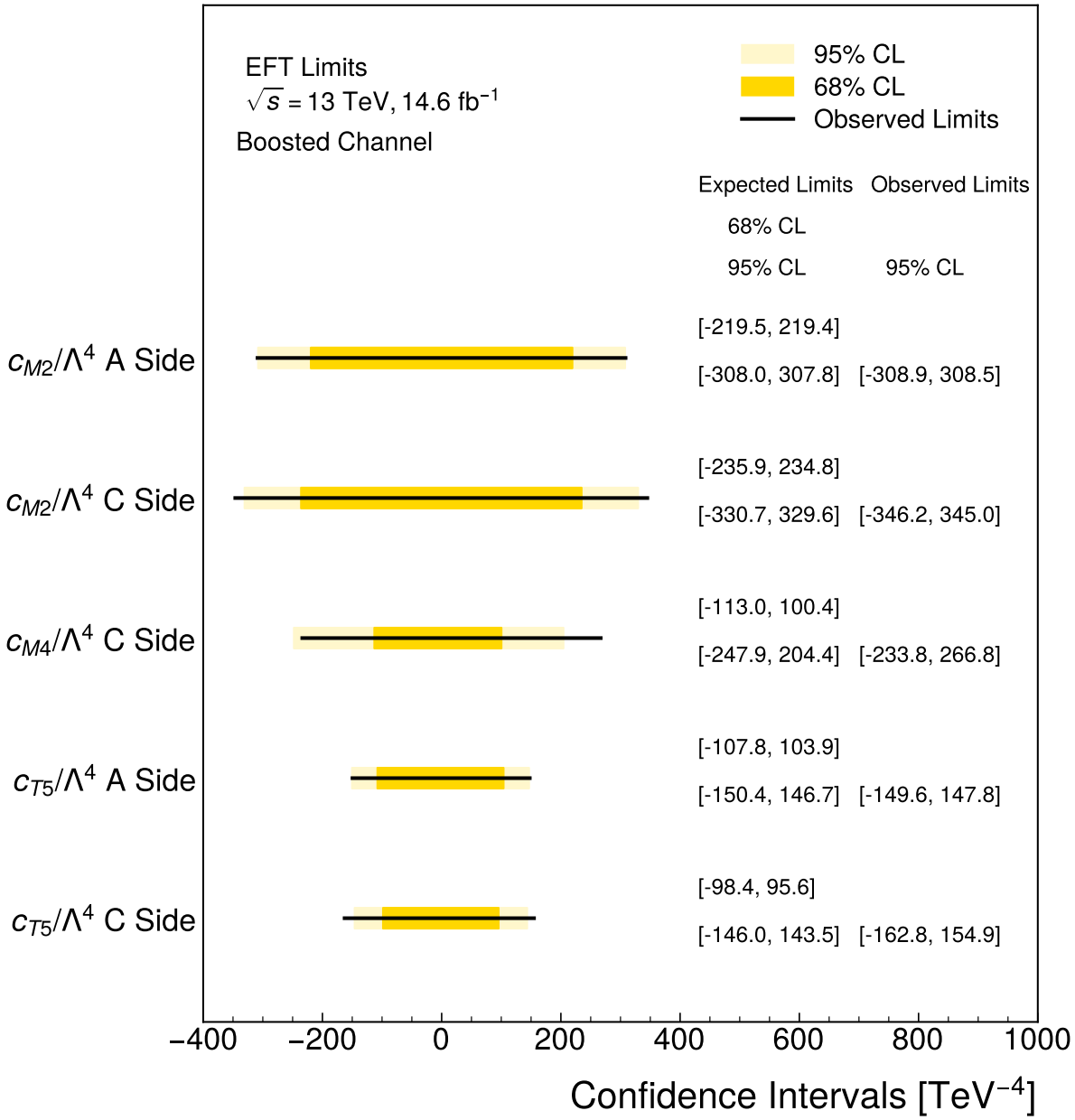

Figure 8.4. The expected and observed limits in the *boosted channels* on the anomalous coupling coefficients of dimension 8 operators. Shown are the $c_{M,2}/\Lambda^4$, $c_{M,4}/\Lambda^4$ and $c_{T,5}/\Lambda^4$ coefficient for signal region on the A and C side. Indicated in dark yellow are the expected limits at a 68% confidence level and in light yellow the 95% confidence level. The observed limits at a 95% confidence level are shown as a solid black line.

8.2.5 Unitarity Violation in SMEFT Model

At sufficiently high energies, the presence of non-zero anomalous quartic gauge couplings will violate unitarity at tree level thus the SMEFT is not a complete model [132]. It is essential to prevent violation of unitarity at high energies and so a cut-off scale is introduced, $\Lambda_{\text{cut-off}}$. The cut-off scale will remove any SMEFT contributions above the cut-off value. As a result, this will lead to the confidence interval becoming larger and less stringent. Contributions from the SM above this cut-off scale are not removed. For the $\gamma\gamma \to WW$ process, the dipole form factor [133] with a cut-off scale $\Lambda_{\text{cut-off}}$ can be applied to modify the coupling as:

$$c_i(m^2_{\gamma\gamma}) \to \frac{c_i(m^2_{\gamma\gamma})}{\left(1 + m^2_{\gamma\gamma}/\Lambda^2_{\text{cut-off}}\right)^2} \tag{8.8}$$

Typically the cut-off scale can be quantified by the invariant mass of the final state objects as it will scale with the energy of the system. For this process, the mass of the WW system can be determined from the energy loss of the protons which scattered, where $m_{\gamma\gamma} = \sqrt{s\ \xi^{\text{A}}_{\text{AFP}}\ \xi^{\text{C}}_{\text{AFP}}}$. In the event selection for both resolved and boosted channels, the $m_{\gamma\gamma}$ is constrained due to the acceptance of the fractional energy loss of the protons $\xi^{\text{A/C}}_{\text{AFP}} \in [0.035, 0.08]$. Schematically this can be seen in the truth level distribution shown in Figure 8.1b. This leads to an upper limit on the mass of $m_{\gamma\gamma} = 1040$ GeV. Consequently, the limits set in Section 8.2.4 are already unitarised. When comparing limits set by different physics processes, various values for a cut-off scale are used, most commonly around 1 TeV, as seen in the vector-boson-scattering searches which probed for sensitivity of dimension 8 anomalous quartic gauge couplings [42, 43, 44, 45]. Therefore for comparison, the results of this thesis will be compared to limits which are also unitarised by a cut-off scale.

8.2.6 Comparison between different processes

The exclusion limits on the anomalous gauge couplings found via the $\gamma\gamma \to WW$ process confirm previous measurements. The $W\gamma jj$ and $Z\gamma jj$ processes obtain the current best limits on the gauge couplings coefficients $c_{M,2}/\Lambda^4$, $c_{M,4}/\Lambda^4$ and $c_{T,5}/\Lambda^4$ [45, 44]. The confidence intervals obtained in this thesis can be compared to the best limits found in the $W\gamma jj$ and $Z\gamma jj$ VBS measurements. The measurements compared to are both searches performed by the ATLAS experiment with a $\sqrt{s} = 13$ TeV using the full Run 2 dataset corresponding to an integrated luminosity of 140 fb^{-1}. The data set used for this thesis is a subset of this at 14.6 fb^{-1}.

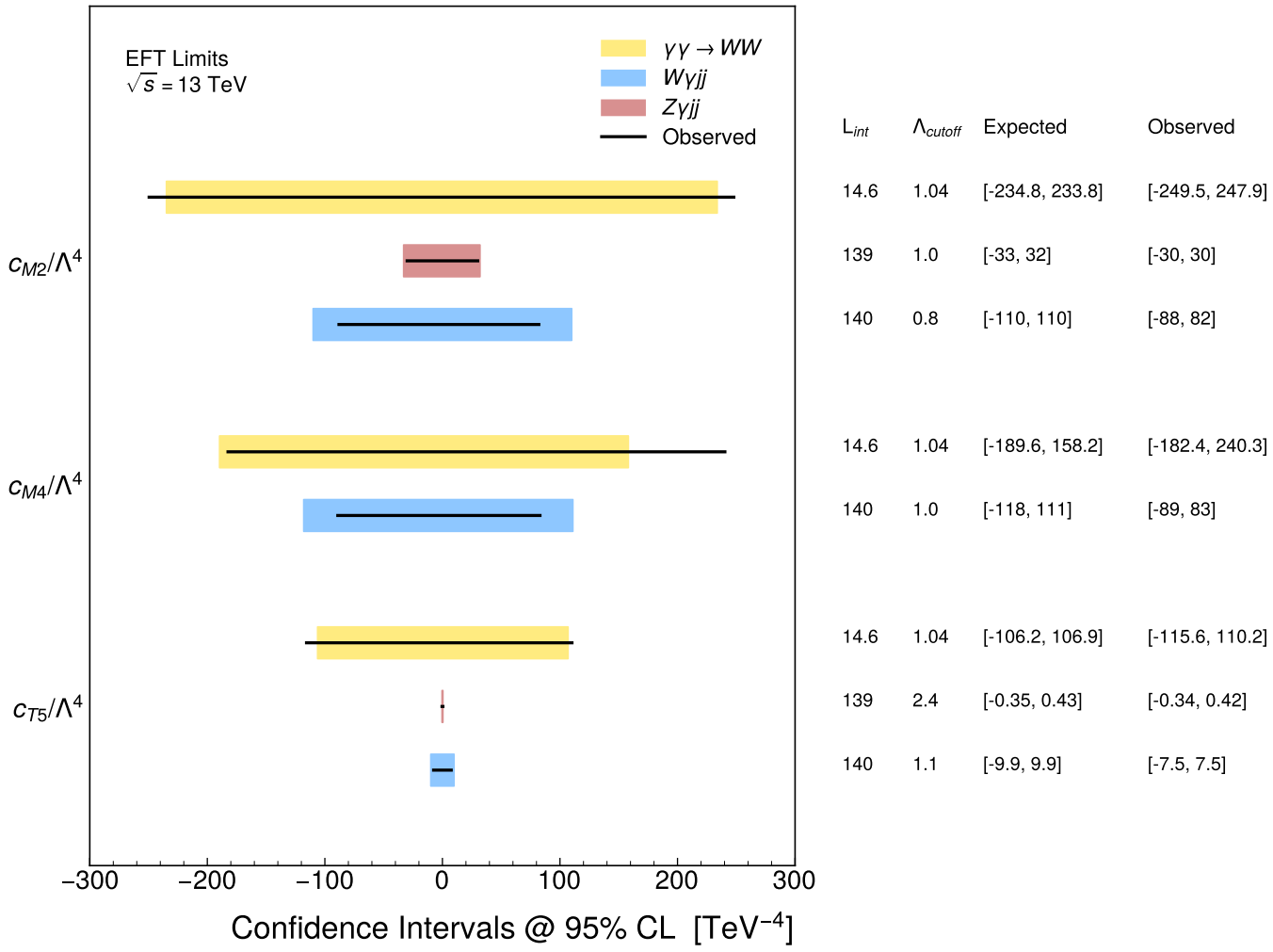

Figure 8.5. Comparison of limits expected and observed for coefficients $c_{M,2}/\Lambda^4$, $c_{M,4}/\Lambda^4$ and $c_{T,5}/\Lambda^4$. Limits compared between values obtained in this thesis via the semileptonic $\gamma\gamma \to WW$ process and values obtained in the ATLAS $W\gamma jj$ and $Z\gamma jj$ measurements, taken from Ref. [45, 44]. Values are all compared at a 95% confidence level. Indicated to the right are the luminosity (in units of fb^{-1}), cut-off energy scale (in units of TeV) and the expected and observed limits for all coefficients.

The comparison is shown in Figure 8.5 where the best limits found in all channels of the semileptonic $\gamma\gamma \to WW$ process are chosen. In yellow are measurements made in this thesis, red that of the $Z\gamma jj$ search and blue for the $W\gamma jj$. The VBS process of the $W\gamma jj$ is the identical quartic vertex to this thesis, $\gamma\gamma \to WW$. For all three operators the confidence intervals derived from the $W\gamma jj$ process are more stringent than that found in $\gamma\gamma \to WW$. The $Z\gamma jj$ has a $ZZ\gamma\gamma$ gauge coupling which is sensitive to the $\mathcal{O}_{M4}$ operator, however no limit was published, most likely due to lack of sensitivity. For the $\mathcal{O}_{M2}$ and $\mathcal{O}_{T5}$, the $Z\gamma jj$ measurement provides the most stringent limits at 13 TeV via a VBS process. The search takes advantage of the higher branching ratio of the $Z \to \nu\nu$ which increases the cross section of the anomalous couplings probed [44]. The measurements of both the $W\gamma jj$ and $Z\gamma jj$ have the advantage from the topology of the VBS process.

There is a large rapidity gap between the two jets produced, providing a kinematic region where the decay products of the scattered bosons are expected. This helps reducing the QCD backgrounds which, in turn, increases sensitivity to the anomalous couplings. The same-sign WW process has a $WWWW$ coupling which is not sensitive to the $\mathcal{O}_{M2}$, $\mathcal{O}_{M4}$ or $\mathcal{O}_{T5}$ operators [42]. The limits set for the coefficient of a given operator can be directly compared to the work of this thesis when a similar cut-off scale of $\Lambda = 1.04$ TeV is applied. The cut-off scale typically loosens the limits the lower the value is as fewer SMEFT contributions are expected at lower energies. The $Z\gamma jj$ uses a cut-off scale of $\Lambda = 2.4$ TeV for the $\mathcal{O}_{T5}$ operator. This helps provide the more stringent confidence interval as more contributions from the SMEFT will be included.

8.3 Kinematic-Dependent Limits

To increase the sensitivity of the measured operators in this thesis, one can consider setting the confidence intervals using information from the kinematic distributions, such as the $m_{\gamma\gamma}$ distribution. The use of a multi-bin likelihood fit provides more stringent confidence limits. This is due to contributions from anomalous couplings increasing with $m_{\gamma\gamma}$ as seen in Figure 8.1b. The gain comes in the opportunity to distinguish the shape of the EFT signal from the SM background, allowing the background to be better constrained in the fit. In this section a preliminary study on the impact of a multi-bin fit to the sensitivity is performed for the $\mathcal{O}_{M,2}$ operator. The quadratic component of the operator is used for this study as it has the smallest statistical uncertainty in the signal region, due to more simulated events passing the event selection. The best $c_{M,2}/\Lambda^4$ limit set was in the resolved channel, A Side, and therefore this channel will be used in the following section.

8.3.1 Background Estimate

The combinatorial background estimated in the signal region is calculated using the scale factor method. The scale factor is used to rescale the background simulated in each bin of the $m_{\gamma\gamma}$ distribution. From Chapter 7, the scale factors of the resolved channel A side are applied to the electron and muon channel separately. For completeness the scale factors which will be used are shown in Table 8.4. The CR3 scale factor is used as it is kinematically closer to the signal. The CR1 will be later included as the modelling systematic uncertainty.

Channel	f_{CR1}	f_{CR3}
e, A Side	1.70 ± 0.13	1.74 ± 0.15
μ, A Side	1.23 ± 0.12	1.47 ± 0.15

Table 8.4. Scale factors for the resolved channel A side. Uncertainties quoted are statistical only.

Figure 8.6 shows the signal region with the estimated combinatorial background obtained from the scale factor method after combining the scaled electron and muon channels. The data observed in the signal region and the the quadratic component of the $\mathcal{O}_{M,2}$ operator is also shown. It can be seen that for the first four bins, the agreement of the data to the estimated background is in agreement within 10%. The estimated background in the last bin is underestimates the data. No contributions from the $\mathcal{O}_{M,2}$ operator are present in the lower bins allowing the fit can constrain the background only model, in this region.

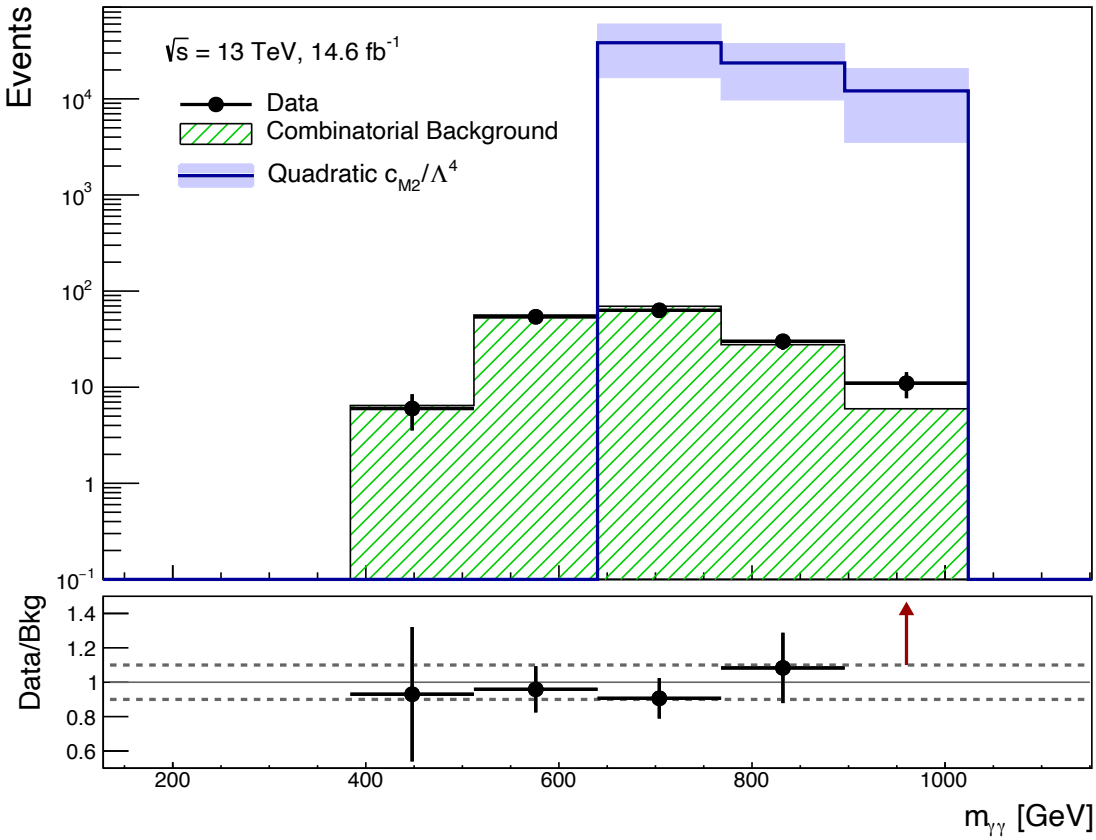

Figure 8.6. Distribution of the $m_{\gamma\gamma}$ in the A side signal region. The estimated combinatorial background obtained using the scale factor method is shown with the data observed. The blue line indicates the simulated contribution from the quadratic component of the $\mathcal{O}_{M,2}$ operator, with the statistical uncertainties in the blue bands. The lower panel shows the ratio between the data and estimated background, with up to 10% agreement in the first four bins.

The linear SMEFT component is omitted from this study as the statistical uncertainty of the linear terms is much larger when split into the bins of the $m_{\gamma\gamma}$ distribution. The impact of omitting it is not significant as the contribution of the linear term is 10^6 smaller than the quadratic terms, as seen in the cross sections obtained in Table 8.2.

The systematic uncertainties quantifying the mismodelling of the background estimate are recalculated for each bin in the likelihood fit. It is accounted for by the difference in the background estimated using the scale factor from CR3 compared to CR1. For the electron channel, the difference is small ($< 4\%$) as the scale factors obtained are very similar. For the muon channel, the difference is around 16%. This background modelling systematic uncertainty is accounted for in the nuisance parameters for the for the SM component in the likelihood fit. The other systematic uncertainty discussed in Section 8.2.3 are included in the nuisance parameters of the quadratic component of the SMEFT contribution in the signal region, assuming it is the same for each bin.

8.3.2 Expected and Observed Limits

The expected and observed limits of the $c_{M,2}/\Lambda^4$ are derived using the methodology described in Section 8.2.2. The limits found with the multibin fit are presented in Figure 8.7 with the limits found previously with the single-bin fit. Comparing to the single-bin fit, there is a clear improvement in the limits obtained. The expected limits at a 95% confidence level improve by 31% and the observed improve by 22%. This is because the multibin fit reveals the kinematic region where the signal is concentrated where the signal to background ratio is much larger than setting limits in the single bin fit. This provides a region where the signal is larger with respect to the background and therefore is better constrained in the fit. The improvement in the results is seen at both the 68% and 95% confidence interval. It merits the choice of using this distribution to set the limits on anomalous gauge quartic couplings. For this method to be applied to all operators, the simulations produced with the SMEFT operators must be produced with a much larger size in order to reduce statistical uncertainties. In doing so, all operators have the potential for the limits to become more stringent for the semileptonic $\gamma\gamma \to WW$ process.

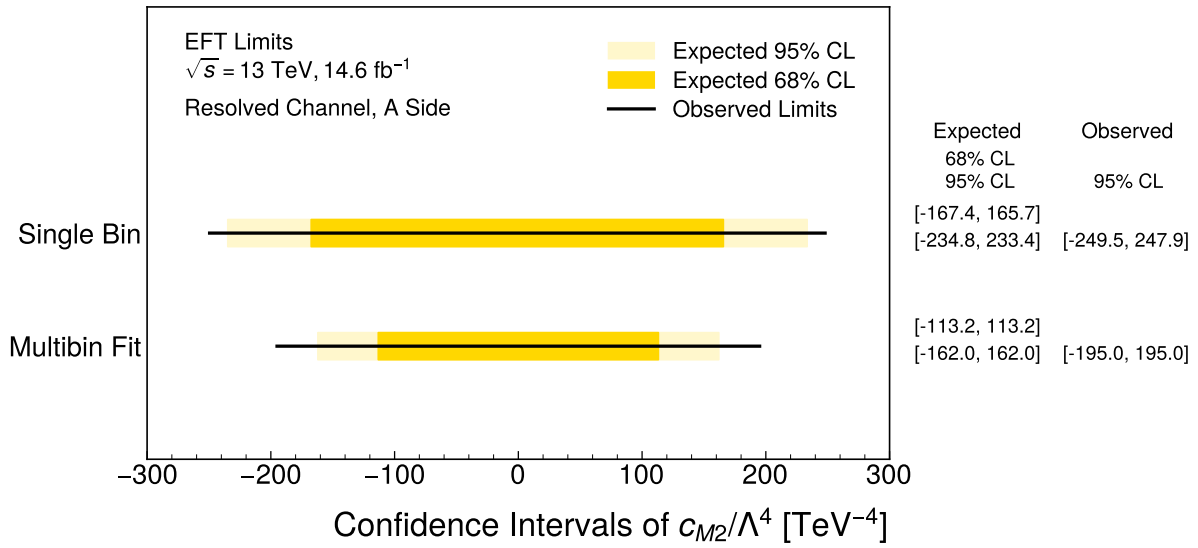

Figure 8.7. The expected and observed limits for the coefficient of the $\mathcal{O}_{M,2}$ operator, obtained with the previous single-bin fit and the multibin fit performed in the $m_{\gamma\gamma}$ distribution. Expected limits shown in dark yellow are at the 68% confidence level and in light yellow at the 95% confidence level. In black are the observed limits obtained at a 95% confidence level.

CHAPTER 9

SUMMARY AND OUTLOOK

Anomalous quartic gauge boson couplings provide a great insight to low energy modifications to the current SM predictions which can indicate New Physics. They are typically measured in vector boson scattering interactions at the LHC. An alternative approach is measuring the photon-induced WW production. The measurement takes advantage of the ATLAS Forward Proton Detector to fully constrain the energy of the W bosons produced in such a process, which is unique to photon-induced processes.

This thesis presents the measurement of anomalous quartic gauge boson couplings via the semileptonic $\gamma\gamma \to WW$ process. It is performed with proton-proton collisions at a centre of mass energy of $\sqrt{s} = 13$ TeV, corresponding to an integrated luminosity of 14.6 fb^{-1}. Simulations of background processes do not include forward pileup protons and therefore need to be modelled and included. The pileup protons are simulated using a data-driven method which models the multiplicity and energy of the protons. Two methods were developed and tested, showing both successfully model the forward pileup protons in regions of interest for this measurement.

The pileup protons overlay the background simulations used in this thesis. The background estimation models the combinatorial background arising from the ATLAS central detector and coincidental pileup protons reconstructed in the AFP detector. The measurements are performed in two models for the hadronic decaying W boson, a resolved channel where the boson decays into two resolved jets and a boosted channel where it decays into one large boosted jet. This is done to test how the sensitivity of anomalous couplings changes with the two reconstruction methods. Due to the differences in the reconstruction of the jets, the two channels have independent event selections which are optimised for the event topology of the $\gamma\gamma \to WW$ process. The signal regions are found to be background dominated due to the similarities of SM background processes and the photon-induced WW process. With the null-hypothesis that the signal region

is expected to only have contributions from SM background processes, the estimation of the backgrounds is performed. Different data-driven methodologies are implemented to validate the estimations derived for the resolved and boosted channels. The results of this estimation are compared with the observed number of events in data showing good agreement within the uncertainties.

Using the Standard Model Effective Field Theory framework, New Physics in the $\gamma\gamma \to WW$ processes can arise from modifications to the SM coupling of the photons and W bosons. The results observed are used to constrain the limits of anomalous quartic gauge boson couplings from this framework. This is done for dimension 8 operators which modify the SM quartic gauge couplings via additional operators added to the Standard Model Lagrangian density. Limits on the coupling coefficients of the respective operators constrained are presented in this thesis for both the resolved and boosted channel individually, at a 95% confidence level. The operators were constrained using signal regions constructed on the A side and on the C side of the AFP detector, which confirmed the limits set are consistent. Comparing the resolved and boosted channel, it is found that the limits set on the coefficients of the dimension 8 operators were $20 - 22\%$ better in the resolved channel. This is due to the larger contribution from SM backgrounds expected and observed in the boosted channel, with respect to the resolved channel. The derived confidence intervals of the coupling coefficients of the operators are in agreement with other vector boson scattering measurements, which are sensitive to the same operators of interest.

Limits observed for the coupling coefficient of the $\mathcal{O}_{M,2}$ operator using the differential distribution in $m_{\gamma\gamma}$ shows a 21% improvement over the frequentist limits set. To extend this differential measurement to all operators, a larger dataset is required. This search is limited in sensitivity due to the size of the dataset and the large combinatorial background which remains present in the signal regions. Future data collected by the AFP detector includes the Time-of-Flight subdetector which can aid in the reduction of backgrounds using the vertex matching of the forward protons and the central detector. Additionally, the larger dataset collected during Run 3 of the LHC will reduce the statistical uncertainties. Together, this will provide the opportunity to further constrain the limits on the anomalous quartic gauge coupling studied in this thesis.

APPENDIX A

NEUTRINO p_z

A.1 Derivation of p_{T}^{ν}

Due to the presence of the neutrino in the final state, the total momentum of the final state cannot be measured directly. A solution to this is to make an analytical measurement of the neutrino by fixing the leptonic W boson to the pole mass $m_W = 80.4$ GeV [93]. The methodology is taken from Ref [92]. To derive the analytical solution, one starts from the Einstein energy-momentum relation, expanding and substituting the mass assumptions.

$$
\begin{aligned}
m_W^2 &= (E^l + E^\nu)^2 - (p^l + p^\nu)^2 \\
m_W^2 &= E^{l2} + E^{\nu 2} + 2 \cdot E^{l2} E^{\nu 2} - p^{l2} - p^{\nu 2} - 2 \cdot p^l p^\nu \\
m_W^2 &= \cancel{E^{l2}} + \cancel{E^{\nu 2}} + 2 \cdot E^{l2} E^{\nu 2} - \cancel{p^{l2}} - \cancel{p^{\nu 2}} - 2 \cdot p^l p^\nu \\
m_W^2 &= 2 \cdot E^{l2} E^{\nu 2} - 2 \cdot p^l p^\nu \\
\frac{m_W^2}{2} &= E^{l2} E^{\nu 2} - p_T^l p_T^\nu - p_z^l p_z^\nu
\end{aligned}
$$

With the following substitution of ζ, the equation can be simplified to a quadratic equation of p_z^ν.

$$
\begin{aligned}
\zeta &= \frac{m_W^2}{2} + p_T^l p_T^\nu \\
(\zeta - p_z^l p_z^\nu)^2 &= E^{l2} E^{\nu 2} = E^{l2}(p_T^{\nu\,2} + p_z^{\nu 2}) \\
\Rightarrow p_z^\nu &= \frac{p_z^l \zeta \pm \sqrt{\Delta}}{{p_T^l}^2} \quad \text{where} \quad \Delta = {p_z^l}^2 \zeta^2 - {p_T^l}^2 [E^{l2} {p_T^\nu}^2 - \zeta^2]
\end{aligned}
$$

A.2 Validation of p_{T}^{ν}

The calculation of the longitudinal neutrino momentum on the reconstruction level can be validated by comparison to the truth level information in simulations. Shown in Figure A.1 is the difference between the reconstruction and truth level values for the simulated signal process $\gamma\gamma \to WW$ in the signal region. The distribution shows the reconstruction level is well modelling the true values of the neutrino p_z values.

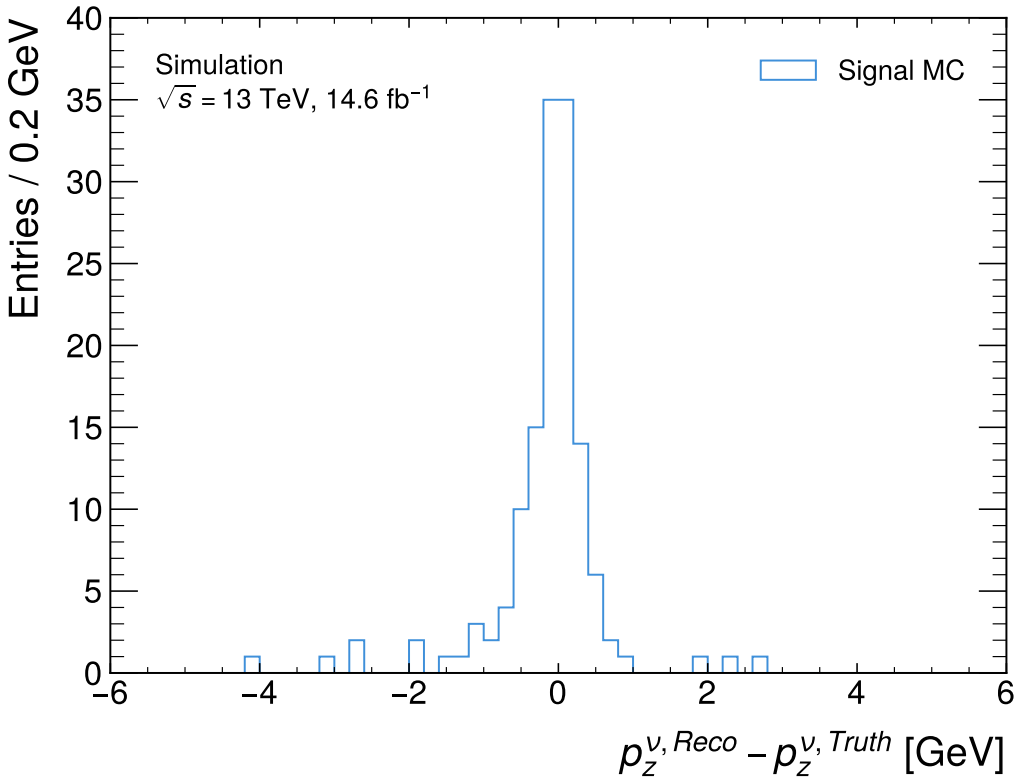

Figure A.1. Resolution of the neutrino p_z values for the signal process in the signal region. The reconstructed values are derived from the methodology discussed in this thesis and then compared to truth level information. The distribution demonstrates that the value is well modelled.

APPENDIX B

DERIVATION OF $\xi^{\pm}_{WW}$

The energy loss of the forward protons is determined with the ATLAS Forward Proton detector. Analogously, the energy loss can be derived from kinematics recorded only with the central ATLAS detector. This can be derived to obtain the expression $\xi^{\pm}_{WW}$. This is presented below for the photon-induced WW production, however it is the same for all photon-induced processes, independent of the final state.

The WW bosons produced in the photon-induced process are back to back in the transverse plane so it is assumed that $p_{\mathrm{T}}^{WW} = 0$. Therefore the energy conservation can be expressed as,

$$\therefore E^2_{WW} = M^2_{WW} + (p_z^{WW})^2. \tag{B.1}$$

The rapidity of the W boson pairs is expressed as,

$$y = \frac{1}{2} ln\left(\frac{E_{WW} + p_z^{WW}}{E_{WW} - p_z^{WW}}\right) \tag{B.2}$$

Substituting Equation B.1 into the denominator of Equation B.2 and simplified to

$$y = ln\left(\pm \frac{E_{WW} + p_z^{WW}}{m_{WW}}\right). \tag{B.3}$$

In the relativistic limit, one can assume that $E_{WW} \approx p_z^{WW}$. Solving Eqn B.3 for E_{WW}, putting in this assumption, one obtains,

$$E_{WW} = \frac{m_{WW} \cdot e^{\pm y}}{2}. \tag{B.4}$$

The fraction of energy lost by the protons with respect to the beam is equivalent to the

energy gained by the WW final state and therefore the ξ_{WW} can be expressed as

$$\xi_{WW} = \frac{E_{WW}}{\sqrt{s}}. \tag{B.5}$$

This value must be expressed separately for the contributions in the positive and negative rapidity of the ATLAS detector, and therefore a factor of half is required for Equation B.5 to be expressed as $\xi^{\pm}_{WW}$. Additionally inputting Eqn B.4, the fractional energy of the WW system can be expressed as

$$\xi^{\pm}_{WW} = \frac{M_{WW}e^{\pm y_{WW}}}{\sqrt{s}}. \tag{B.6}$$

Equation B.6 is used in this thesis as it only requires the mass and rapidity of the WW system which can be measured by the ATLAS experiment without any information from the forward detectors.

APPENDIX C

MODELLING OF PILEUP PROTONS

The modelling of $\xi_{AFP}^{A/C}$ is performed with both the event overlay and random sampling method. The results of the electron channel modelling are shown in Figure C.1. The two methods are in agreement and additionally model the data well.

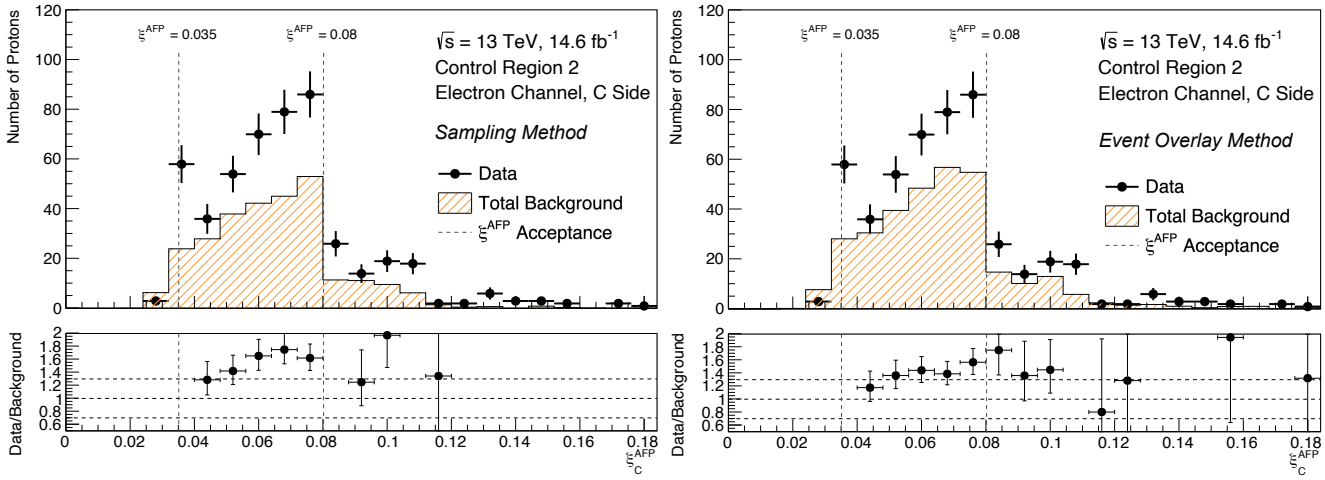

(a) **(b)**

Figure C.1. Comparison of proton fractional energy loss modelled in background simulations using the sampling method. Distributions shown are for the Electron channel for both A (Figure C.1a) and (Figure C.1b) side of the AFP detector. Lower panels show the ratio of Data/Total Background simulated.

APPENDIX D

ADDITIONAL DISTRIBUTIONS FOR BACKGROUND ESTIMATION

D.1 Comparison of $\xi_{\mathbf{AFP}}$ distribution for Muon Channel

In Chapter 7, the shape of the background processes in the region where the background estimation is calculated are compared. The shape being independent of the physics process justifies the modelling of the total background as a combinatorial background. The chapter showed this to be true for the resolved electron channel. Similar distributions are obtained for the resolved muon channel, presented below in Figure D.1.

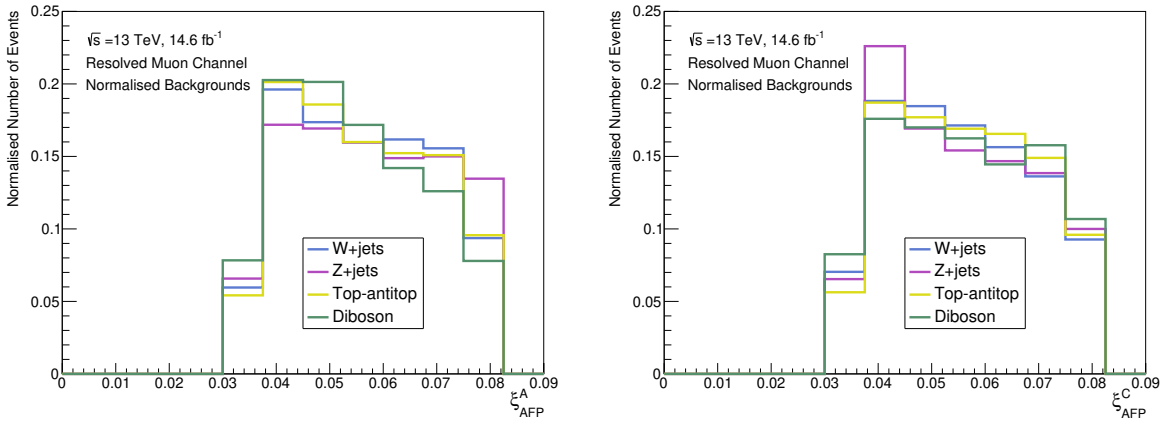

(a) **(b)**

Figure D.1. Normalised $\xi_{\mathrm{AFP}}^{\mathrm{A/C}}$ distributions of simulated background processes in the inclusive region where background estimation is determined. Shown are the distributions for the resolved muon channel on the A side (Fig.D.1a) and C side (Fig.D.1b).

D.2 Modelling CR for the Muon Channel

In the Chapter 7 the CR1 distributions on the A side are shown for the electron channel to show how the simulations models the shape of the data. Similar distributions are shown for the muon channel for the resolved channel, A side. in Figure D.2. Included for each distribution is the ratio between the data and the MC simulations which is constant within the uncertainties.

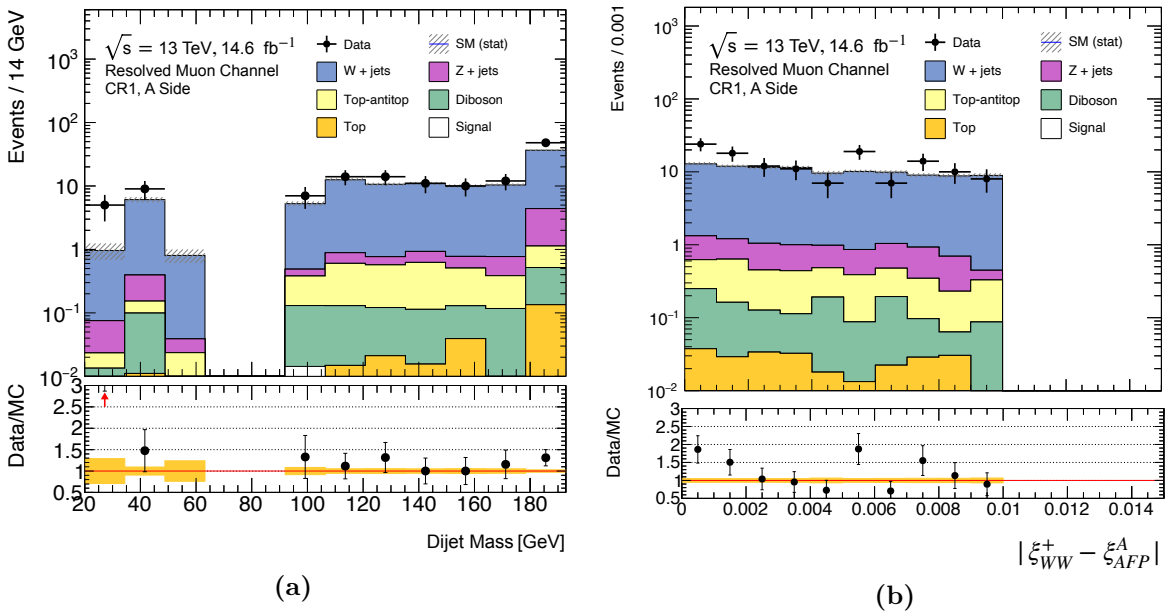

(a) (b)

Figure D.2. Distributions of the dijet mass (Fig.D.2a) and $|\xi^{\pm}_{WW} - \xi^{\mathrm{A/C}}_{\mathrm{AFP}}|$ (Fig.D.2b) in muon channel of CR1 on the A side.

D.3 Comparing CR2 and CR3

To ensure the modelling is constant in all control regions similar verifications are made in CR2 and CR3. Shown in Figure D.3 is the m_{jj} distribution of CR2 and CR3 for the electron resolved channel for the A side. Similar agreement in the ratios is observed again.

D.4 Comparing A and C Side

To confirm the distributions are similar on A and C side, the $|\xi^{\pm}_{WW} - \xi^{\mathrm{A/C}}_{\mathrm{AFP}}|$ distribution of the Control Region 3 are plotted below. Of the possible channels and kinematics this is the one with the largest differences from A to C side. Shown in Figure D.4, there is good agreement between the two sides, with the ratio of the data over MC simulation showing that the simulations models the shape of the data, i.e constant.

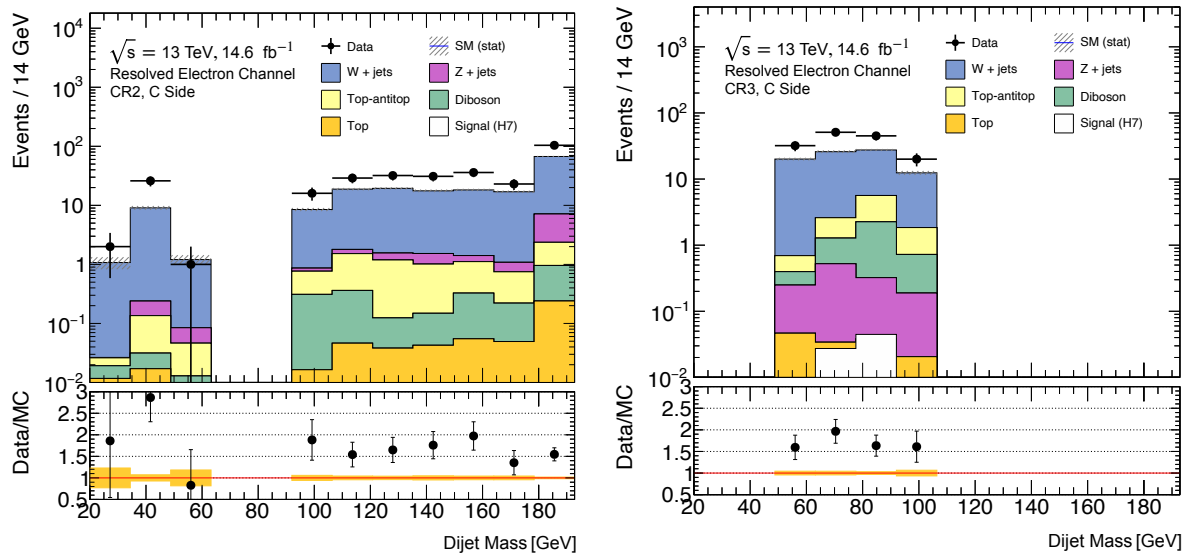

(a) (b)

Figure D.3. Distributions of the dijet mass for CR2 shown in Fig.D.3a and CR3 in Figure D.3b for the electron channel, A side.

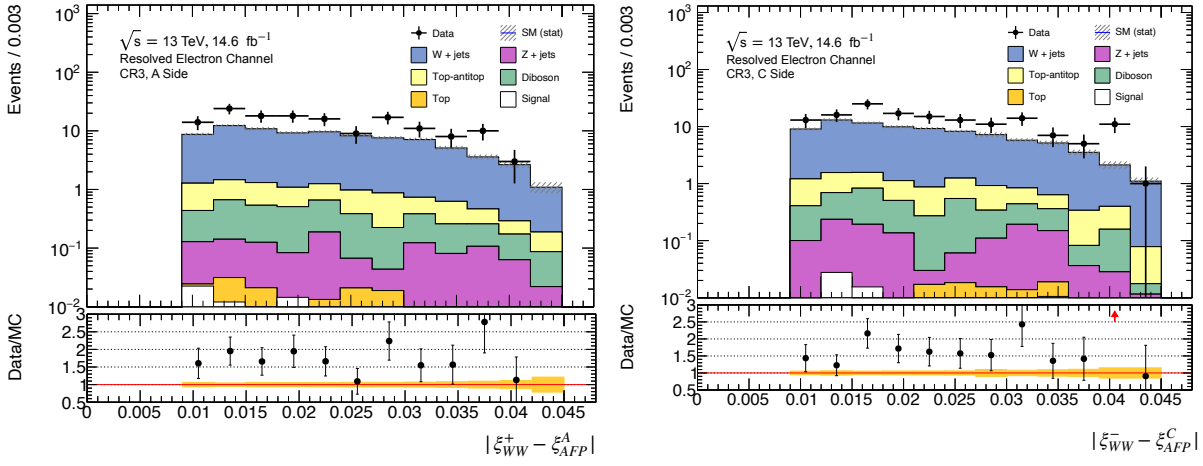

(a) (b)

Figure D.4. Distributions of $|\xi^{\pm}_{WW} - \xi^{\mathrm{A/C}}_{\mathrm{AFP}}|$ in the electron channel of CR3 on the A side (Fig.D.4a) and C Side (Fig.D.4b).

APPENDIX E

ADDITIONAL MATERIAL AND DISTRIBUTIONS FOR EFFECTIVE FIELD THEORY INTERPRETATION

E.1 Defining Dimension 8 EFT Operators

From the Eboli model of quartic gauge bosons [118], the fourteen operators which the $\gamma\gamma \to WW$ processes are defined below. They are constructed from field strength tensors $W_{\mu\nu}$ of the $\mathrm{SU(2)_L}$ symmetry and $B_{\mu\nu}$ of the $\mathrm{U(1)_Y}$ symmetric and from the covariant derivative of the Higgs field $D_\mu\Phi$. The field stregth tensors are previously defined in Equations 2.3 and 2.4 respectively. The operators of the dimension 8 Lagrangian in the SMEFT framework can be organised into mixed (M) operators, constructed from two field strength tensors and the $D\Phi$, and transverse (T) operators which are constructed purely from field strength tensors. There are also longitudinal operators (S) which are constructed of purely derivatives of the Higgs field. The $\gamma\gamma \to WW$ is not sensitive to these operators and are therefore omitted.

The mixed operators are defined as:

$$\mathscr{O}_{M,0} = Tr\left[\widehat{W}_{\mu\nu}\widehat{W}^{\mu\nu}\right] \times \left[(D_\beta\Phi)^\dagger D^\beta\Phi\right] \tag{E.1}$$

$$\mathscr{O}_{M,1} = Tr\left[\widehat{W}_{\mu\nu}\widehat{W}^{\beta\nu}\right] \times \left[(D_\beta\Phi)^\dagger D^\mu\Phi\right] \tag{E.2}$$

$$\mathscr{O}_{M,2} = \left[B_{\mu\nu}B^{\mu\nu}\right] \times \left[(D_\beta\Phi)^\dagger D^\beta\Phi\right] \tag{E.3}$$

$$\mathscr{O}_{M,3} = \left[B_{\mu\nu}B^{\beta\nu}\right] \times \left[(D_\beta\Phi)^\dagger D^\mu\Phi\right] \tag{E.4}$$

$$\mathscr{O}_{M,4} = \left[(D_\mu\Phi)^\dagger\widehat{W}_{\beta\nu}D^\mu\Phi\right] \times B^{\beta\nu} \tag{E.5}$$

$$\mathscr{O}_{M,5} = \left[(D_\mu\Phi)^\dagger\widehat{w}_{\beta\nu}D^\nu\Phi\right] \times B^{\beta\mu} + h.c \tag{E.6}$$

$$\mathscr{O}_{M,7} = \left[(D_\mu\Phi)^\dagger\widehat{W}_{\beta\nu}\widehat{W}^{\beta\mu}D^\nu\Phi\right]. \tag{E.7}$$

The transverse operators are defined as:

$$\mathcal{O}_{T,0} = Tr\left[\widehat{W}_{\mu\nu}\widehat{W}^{\mu\nu}\right] \times Tr\left[\widehat{W}_{\alpha\beta}\widehat{W}^{\alpha\beta}\right] \tag{E.8}$$

$$\mathcal{O}_{T,1} = Tr\left[\widehat{W}_{\alpha\nu}\widehat{W}^{\mu\beta}\right] \times Tr\left[\widehat{W}_{\mu\beta}\widehat{W}^{\alpha\nu}\right] \tag{E.9}$$

$$\mathcal{O}_{T,2} = Tr\left[\widehat{W}_{\alpha\mu}\widehat{W}^{\mu\beta}\right] \times Tr\left[\widehat{W}_{\beta\nu}\widehat{W}^{\nu\alpha}\right] \tag{E.10}$$

$$\mathcal{O}_{T,3} = Tr\left[\widehat{W}_{\alpha\mu}\widehat{W}^{\mu\beta}\widehat{W}^{\nu\alpha}\right] \times B_{\beta\nu} \tag{E.11}$$

$$\mathcal{O}_{T,4} = Tr\left[\widehat{W}_{\alpha\mu}\widehat{W}^{\alpha\mu}\widehat{W}^{\beta\nu}\right] \times B_{\beta\nu} \tag{E.12}$$

$$\mathcal{O}_{T,5} = Tr\left[\widehat{W}_{\mu\nu}\widehat{W}^{\mu\nu}\right] \times B_{\alpha\beta}B^{\alpha\beta} \tag{E.13}$$

$$\mathcal{O}_{T,6} = Tr\left[\widehat{W}_{\alpha\nu}\widehat{W}^{\mu\beta}\right] \times B_{\mu\beta}B^{\alpha\nu} \tag{E.14}$$

$$\mathcal{O}_{T,7} = Tr\left[\widehat{W}_{\alpha\mu}\widehat{W}^{\mu\beta}\right] \times B_{\beta\nu}B^{\nu\alpha} \tag{E.15}$$

E.2 Sensitivity to Dimension 6 EFT Operators

The $\gamma\gamma \to WW$ process is sensitive to both dimension 6 and dimension 8 operators of the SMEFT. The cross sections of the processes are modified when including the SMEFT operators with the SM Lagrangian. The cross section of this process with the inclusion of the respective dimension 6 operators are shown in Table E.1. They are orders of magnitude smaller than that in dimension 8 and are therefore omitted from this thesis.

Operator	Linear Cross Section [pb]	Quadratic Cross Section [pb]
Dimension 6 Operators		
$\mathcal{O}_W^6$	-1.1×10^{-1}	1.2×10^{0}
$\mathcal{O}_{HW}^6$	1.8×10^{-4}	6.8×10^{-5}
$\mathcal{O}_{HB}^6$	5.9×10^{-4}	8.1×10^{-4}
$\mathcal{O}_{HWB}^6$	3.3×10^{-3}	4.0×10^{-4}
$\mathcal{O}_{Hq3}^6$	18.9×10^{-4}	5.7×10^{-5}
$\mathcal{O}_{Hl3}^6$	-5.7×10^{-3}	5.2×10^{-4}
$\mathcal{O}_{ll1}^6$	3.8×10^{-3}	2.3×10^{-4}
$\mathcal{O}_{H\Box}^6$	-1.5×10^{-6}	5.0×10^{-9}
$\mathcal{O}_{HDD}^6$	-3.3×10^{-3}	1.7×10^{-4}

Table E.1. Generator cross section for dimension 6 operators which can be probed with the $\gamma\gamma \to WW$ process.

E.3 Rivet Sensitivity Studies

Using Rivet [119], the kinematic distribution of the Standard Model, linear and quadratic contributions, from the decomposition method. Shown in Figure E.1 are the distribution obtained for the proton fractional energy loss ($\xi_{\mathrm{AFP}}^{A/C}$).

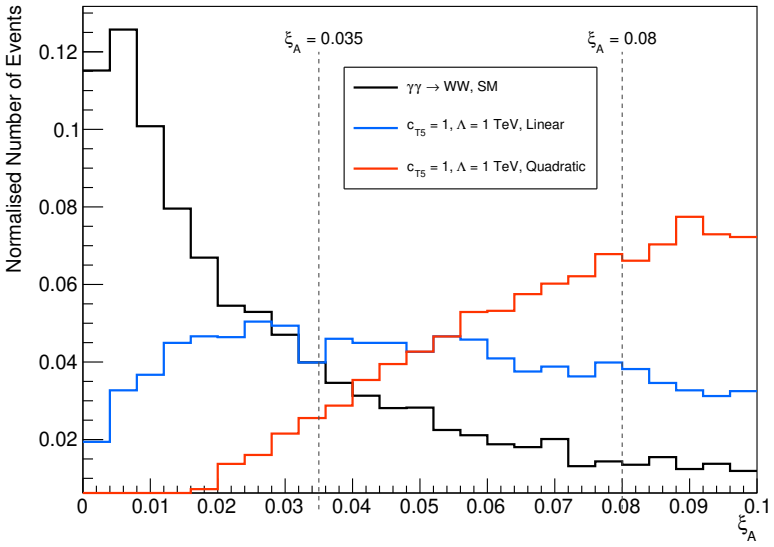

(a)

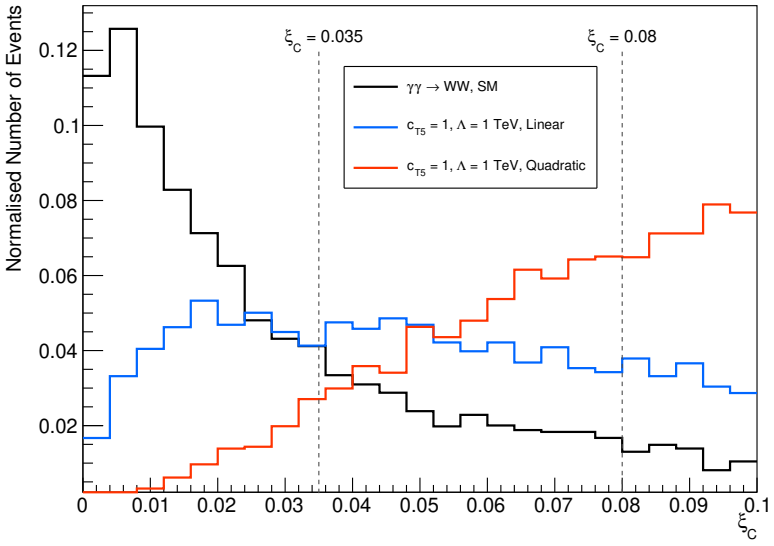

(b)

Figure E.1. Normalised generator level distributions of the proton $\xi_{\mathrm{AFP}}^{A/C}$. Shown are the SM, linear and quadratic distributions obtained with $\mathcal{O}_{T,5}$ operator with the coupling coefficient $c_{T,5}$ and the energy scale Λ set to unity.

E.4 EFT Limits for all Operators

In this thesis, the confidence interval for the coupling coefficient of the respective EFT operators are set. This section provides the complete list of limits obtained for all the dimension 8 operators which the $\gamma\gamma \to WW$ process is sensitive to. All four signal regions are presented, where in Table E.2 the resolved channel is presented for both A and C side. Similarly for the boosted channel in Table E.3. In both tables both the expected and observed limits are shown at a 95% confidence interval. Any missing operators is due to very low statistics which lead to the likelihood fits not converging.

Coupling	Expected $\times 10^3$ [TeV^4]	Observed $\times 10^3$ [TeV^4]
$c_{M,0}/\Lambda^4$, A Side	$[-1.66\ , 1.68]$	$[-1.8\ , 1.85]$
$c_{M,0}/\Lambda^4$, C Side	$[-1.67\ , 1.69]$	$[-2.0\ , 2.01]$
$c_{M,1}/\Lambda^4$, A Side	$[-6.46\ , 6.41]$	$[-7.0\ , 6.93]$
$c_{M,1}/\Lambda^4$, C Side	$[-5.69\ , 5.65]$	$[-7.1\ , 7.93]$
$c_{M,2}/\Lambda^4$, A Side	$[-0.23\ , 0.23]$	$[-0.18\ , 0.24]$
$c_{M,2}/\Lambda^4$, C Side	$[-0.21\ , 0.21]$	$[-0.26\ , 0.25]$
$c_{M,3}/\Lambda^4$, A Side	$[-0.77\ , 0.78]$	$[-0.86\ , 0.83]$
$c_{M,3}/\Lambda^4$, C Side	$[-0.75\ , 0.75]$	$[-0.89\ , 0.74]$
$c_{M,4}/\Lambda^4$, A Side	$[-0.19\ , 0.16]$	$[-0.18\ , 0.24]$
$c_{M,4}/\Lambda^4$, C Side	$[-0.46\ , 0.41]$	$[-0.52\ , 0.53]$
$c_{M,5}/\Lambda^4$, A Side	$[-1.37\ , 1.38]$	$[-1.36\ , 1.48]$
$c_{M,5}/\Lambda^4$, C Side	$[-1.27\ , 1.29]$	$[-1.47\ , 1.49]$
$c_{M,7}/\Lambda^4$, A Side	$[-1.37 \times 10^1\ , 1.42 \times 10^1]$	$[-1.43 \times 10^1\ , 1.46 \times 10^1]$
$c_{M,7}/\Lambda^4$, C Side	$[-1.33 \times 10^1\ , 1.35 \times 10^1]$	$[-1.32 \times 10^1\ , 1.31 \times 10^1]$
$c_{T,0}/\Lambda^4$, A Side	$[-8.33\ , 6.99]$	$[-8.40\ , 7.21]$
$c_{T,0}/\Lambda^4$, C Side	$[-5.16\ , 6.94]$	$[-9.89\ , 6.09]$
$c_{T,1}/\Lambda^4$, A Side	$[-1.05\ , 1.02]$	$[-1.10\ , 1.14]$
$c_{T,1}/\Lambda^4$, C Side	$[-1.03\ , 1.02]$	$[-1.26\ , 1.22]$
$c_{T,2}/\Lambda^4$, A Side	$[-1.18\ , 1.17]$	$[-1.28\ , 1.22]$
$c_{T,2}/\Lambda^4$, C Side	$[-1.03\ , 1.02]$	$[-1.25\ , 1.23]$
$c_{T,3}/\Lambda^4$, A Side	$[-1.61\ , 1.54]$	$[-1.78\ , 1.65]$
$c_{T,3}/\Lambda^4$, C Side	$[-1.58\ , 1.49]$	$[-1.89\ , 1.78]$
$c_{T,4}/\Lambda^4$, A Side	$[-0.36\ , 0.35]$	$[-0.39\ , 0.37]$
$c_{T,4}/\Lambda^4$, C Side	$[-0.38\ , 0.37]$	$[-0.45\ , 0.44]$
$c_{T,5}/\Lambda^4$, A Side	$[-0.11\ , 0.11]$	$[-0.12\ , 0.11]$
$c_{T,5}/\Lambda^4$, C Side	$[-0.16\ , 0.15]$	$[-0.19\ , 0.18]$
$c_{T,6}/\Lambda^4$, A Side	$[-0.29\ , 0.27]$	$[-0.31\ , 0.30]$
$c_{T,6}/\Lambda^4$, C Side	$[-0.27\ , 0.25]$	$[-0.34\ , 0.33]$
$c_{T,7}/\Lambda^4$, A Side	$[-7.58 \times 10^1\ , 2.30 \times 10^1]$	$[-5.47 \times 10^1\ , 6.46 \times 10^1]$
$c_{T,7}/\Lambda^4$, C Side	$[-1.94 \times 10^1\ , 1.47 \times 10^1]$	$[-1.30 \times 10^1\ , 2.64 \times 10^1]$

Table E.2. Expected and observed confidence intervals obtained at a 95% confidence level.

Coupling	Expected $\times 10^3$ [TeV^4]	Observed $\times 10^3$ [TeV^4]
$c_{M,0}/\Lambda^4$, A Side	$[-2.14,\ 2.14]$	$[-2.13,\ 2.14]$
$c_{M,0}/\Lambda^4$, C Side	$[-2.60,\ 2.64]$	$[-2.72,\ 2.77]$
$c_{M,1}/\Lambda^4$, A Side	$[-7.05,\ 6.88]$	$[-7.07,\ 6.90]$
$c_{M,1}/\Lambda^4$, C Side	$[-8.03,\ 8.14]$	$[-8.42,\ 8.33]$
$c_{M,2}/\Lambda^4$, A Side	$[-0.31,\ 0.31]$	$[-0.31,\ 0.31]$
$c_{M,2}/\Lambda^4$, C Side	$[-0.33,\ 0.33]$	$[-0.35,\ 0.35]$
$c_{M,3}/\Lambda^4$, A Side	$[-0.86,\ 0.89]$	$[-0.89,\ 0.88]$
$c_{M,3}/\Lambda^4$, C Side	$[-0.98,\ 0.98]$	$[-0.10,\ 0.10]$
$c_{M,4}/\Lambda^4$, C Side	$[-0.25,\ 0.20]$	$[-0.23,\ 0.27]$
$c_{M,5}/\Lambda^4$, A Side	$[-1.84,\ 1.84]$	$[-1.84,\ 1.84]$
$c_{M,5}/\Lambda^4$, C Side	$[-1.77,\ 1.78]$	$[-1.85,\ 1.86]$
$c_{M,7}/\Lambda^4$, A Side	$[-11.89,\ 12.06]$	$[-12.34,\ 12.23]$
$c_{M,7}/\Lambda^4$, C Side	$[-14.76,\ 14.91]$	$[-14.24,\ 14.13]$
$c_{T,0}/\Lambda^4$, A Side	$[-0.46,\ 0.45]$	$[-0.49,\ 0.49]$
$c_{T,0}/\Lambda^4$, C Side	$[-0.46,\ 0.45]$	$[-0.52,\ 0.50]$
$c_{T,1}/\Lambda^4$, A Side	$[-1.21,\ 1.21]$	$[-1.23,\ 1.23]$
$c_{T,1}/\Lambda^4$, C Side	$[-1.26,\ 1.21]$	$[-1.27,\ 1.25]$
$c_{T,2}/\Lambda^4$, A Side	$[-2.05,\ 2.05]$	$[-2.03,\ 1.98]$
$c_{T,2}/\Lambda^4$, C Side	$[-1.65,\ 1.61]$	$[-1.73,\ 1.69]$
$c_{T,3}/\Lambda^4$, A Side	$[-1.79,\ 1.77]$	$[-1.78,\ 1.75]$
$c_{T,3}/\Lambda^4$, C Side	$[-1.81,\ 1.78]$	$[-1.90,\ 1.87]$
$c_{T,4}/\Lambda^4$, A Side	$[-0.67,\ 0.67]$	$[-0.61,\ 0.62]$
$c_{T,4}/\Lambda^4$, C Side	$[-0.51,\ 0.51]$	$[-0.54,\ 0.54]$
$c_{T,5}/\Lambda^4$, A Side	$[-0.15,\ 0.15]$	$[-0.15,\ 0.15]$
$c_{T,5}/\Lambda^4$, C Side	$[-0.15,\ 0.14]$	$[-0.16,\ 0.15]$

Table E.3. Expected and observed confidence intervals obtained at a 95% confidence level.

BIBLIOGRAPHY

[1] ATLAS Collaboration. "Observation of a new particle in the search for the Standard Model Higgs boson with the ATLAS detector at the LHC". In: *Physics Letters B* 716.1 (Sept. 2012), pp. 1–29. ISSN: 0370-2693. DOI: 10.1016/j.physletb.2012.08.020.

[2] The CMS Collaboration. "Observation of a new boson at a mass of 125 GeV with the CMS experiment at the LHC". In: *Physics Letters B* 716.1 (Sept. 2012), pp. 30–61. ISSN: 0370-2693. DOI: 10.1016/j.physletb.2012.08.021.

[3] ATLAS Collaboration. "Performance of the ATLAS forward proton Time-of-Flight detector in Run 2". In: *Journal of Instrumentation* 19.05 (May 2024), P05054. ISSN: 1748-0221. DOI: 10.1088/1748-0221/19/05/p05054. URL: http://dx.doi.org/10.1088/1748-0221/19/05/P05054.

[4] Varsiha Sothilingam. "ATLAS Forward Proton Time-of-Flight detectors: status, performance and new physics results". In: Jan. 2024, p. 245. DOI: 10.22323/1.450.0245.

[5] Florian Frauen. "Trigger and Tracking Studies for Charged-Particles Multiplicity Measurements at $\sqrt{s}$=13.6 TeV with the ATLAS Detector". Masterarbeit. Heidelberg University, 2023.

[6] ATLAS Collaboration. *ATLAS Common Analysis Framework*. URL: https://atlas-caf.web.cern.ch.

[7] Alexander Bednyakov. "Quantum Field Theory and the Electroweak Standard Model". In: *CERN Yellow Rep. School Proc.* (2019). arXiv: 1812.10675 [hep-ph].

[8] Michael Edward Peskin and Daniel V. Schroeder. *An Introduction to Quantum Field Theory*. Reading, USA: Addison-Wesley (1995) 842 p. Westview Press, 1995.

[9] H. David Politzer. "Reliable Perturbative Results for Strong Interactions?" In: *Phys. Rev. Lett.* 30 (26 June 1973), pp. 1346–1349. DOI: 10.1103/PhysRevLett.30.1346.

[10] David J. Gross and Frank Wilczek. "Ultraviolet Behavior of Non-Abelian Gauge Theories". In: *Phys. Rev. Lett.* 30 (26 June 1973), pp. 1343–1346. DOI: 10.1103/PhysRevLett.30.1343.

[11] Steven Weinberg. "A Model of Leptons". In: *Phys. Rev. Lett.* 19 (21 Nov. 1967), pp. 1264–1266. DOI: 10.1103/PhysRevLett.19.1264.

[12] Sheldon L. Glashow. "Partial-symmetries of weak interactions". In: *Nuclear Physics* 22.4 (1961), pp. 579–588. ISSN: 0029-5582. DOI: https://doi.org/10.1016/0029-5582(61)90469-2. URL: https://www.sciencedirect.com/science/article/pii/0029558261904692.

[13] Abdus Salam. "Weak and Electromagnetic Interactions". In: *Conf. Proc. C* 680519 (1968), pp. 367–377. DOI: 10.1142/9789812795915_0034.

[14] Jorge Crispim Romão. *Advanced quantum field theory*. 2019. URL: http://porthos.ist.utl.pt/ftp/textos/tca.pdf.

[15] Mark Thomson. *Modern Particle Physics*. Cambridge University Press, 2013.

[16] P Abreu et al. "Measurement of the triple-gluon vertex from 4-jet events at LEP". In: *Z. Phys. C* 59 (1993), pp. 357–368. DOI: 10.1007/BF01498617. URL: https://cds.cern.ch/record/246874.

[17] Ettore Majorana. "A Symmetric Theory of Electrons and Positrons". In: *Scientific Papers of Ettore Majorana: A New Expanded Edition*. Ed. by Luisa Cifarelli. Cham: Springer International Publishing, 2020, pp. 113–128. ISBN: 978-3-030-23509-3. DOI: 10.1007/978-3-030-23509-3_11.

[18] Steven Weinberg. "Models of lepton and quark masses". In: *Physical Review D* 101.3 (Feb. 2020). ISSN: 2470-0029. DOI: 10.1103/physrevd.101.035020.

[19] Q. R. Ahmad et al. "Measurement of the Rate of $\nu_e + d \rightarrow p + p + e^-$ Interactions Produced by ^8B Solar Neutrinos at the Sudbury Neutrino Observatory". In: *Physical Review Letters* 87.7 (July 2001). ISSN: 1079-7114. DOI: 10.1103/physrevlett.87.071301.

[20] Y. Fukuda et al. "Evidence for Oscillation of Atmospheric Neutrinos". In: *Physical Review Letters* 81.8 (Aug. 1998), pp. 1562–1567. ISSN: 1079-7114. DOI: 10.1103/physrevlett.81.1562.

[21] F. Englert and R. Brout. "Broken Symmetry and the Mass of Gauge Vector Mesons". In: *Phys. Rev. Lett.* 13 (9 Aug. 1964), pp. 321–323. DOI: 10.1103/PhysRevLett.13.321.

[22] Peter W. Higgs. "Broken Symmetries and the Masses of Gauge Bosons". In: *Phys. Rev. Lett.* 13 (16 Oct. 1964), pp. 508–509. DOI: 10.1103/PhysRevLett.13.508.

[23] M. Tanabashi et al. "Review of Particle Physics". In: *Phys. Rev. D* 98 (3 Aug. 2018), p. 030001. DOI: 10.1103/PhysRevD.98.030001.

[24] ATLAS Collaboration. *Standard Model Summary Plots June 2024*. Tech. rep. Geneva: CERN, 2024. URL: https://cds.cern.ch/record/2903866.

[25] Giampiero Esposito. *An introduction to quantum gravity*. 2011. arXiv: 1108.3269 [hep-th].

[26] Fernando Marchesano, Gary Shiu, and Timo Weigand. "The Standard Model from String Theory: What Have We Learned?" In: *Annual Review of Nuclear and Particle Science* 74.1 (Sept. 2024), pp. 113–140. ISSN: 1545-4134. DOI: 10.1146/annurev-nucl-102622-012235.

[27] Planck Collaboration. "Planck 2013 results. I. Overview of products and scientific results". In: *Astronomy ; Astrophysics* 571 (Oct. 2014), A1. ISSN: 1432-0746. DOI: 10.1051/0004-6361/201321529.

[28] Sean M. Carroll. "The Cosmological Constant". In: *Living Reviews in Relativity* 4.1 (Feb. 2001). ISSN: 1433-8351. DOI: 10.12942/lrr-2001-1.

[29] Andrei D Sakharov. "Violation of CP invariance, C asymmetry, and baryon asymmetry of the universe". In: *Soviet Physics Uspekhi* 34.5 (May 1991), p. 392. DOI: 10.1070/PU1991v034n05ABEH002497.

[30] K. Abe et al. "Observation of mixing-induced CP violation in the neutral B meson system". In: *Physical Review D* 66.3 (Aug. 2002). ISSN: 1089-4918. DOI: 10.1103/physrevd.66.032007.

[31] A. Alavi-Harati et al. "Observation of Direct CP Violation in $K_{S,L} \to \pi\pi$ Decays". In: *Physical Review Letters* 83.1 (July 1999), pp. 22–27. ISSN: 1079-7114. DOI: 10.1103/physrevlett.83.22.

[32] B. Aubert et al. "Observation of CP violation in the B^0 meson system". In: *Physical Review Letters* 87.9 (Aug. 2001). ISSN: 1079-7114. DOI: 10.1103/physrevlett.87.091801.

[33] O. J. P. Éboli, M. C. Gonzalez-Garcia, and S. M. Lietti. "Bosonic quartic couplings at CERN LHC". In: *Physical Review D* 69.9 (May 2004). ISSN: 1550-2368. DOI: 10.1103/physrevd.69.095005.

[34] Céline Degrande et al. "Effective field theory: A modern approach to anomalous couplings". In: *Annals of Physics* 335 (Aug. 2013), pp. 21–32. ISSN: 0003-4916. DOI: 10.1016/j.aop.2013.04.016.

[35] Rodrigo Alonso et al. "Renormalization group evolution of the Standard Model dimension six operators III: gauge coupling dependence and phenomenology". In: *Journal of High Energy Physics* 2014.4 (Apr. 2014). ISSN: 1029-8479. DOI: 10.1007/jhep04(2014)159.

[36] B. Grzadkowski et al. "Dimension-six terms in the Standard Model Lagrangian". In: *Journal of High Energy Physics* 2010.10 (Oct. 2010). ISSN: 1029-8479. DOI: 10.1007/jhep10(2010)085.

[37] Christopher W. Murphy. "Dimension-8 operators in the Standard Model Effective Field Theory". In: *Journal of High Energy Physics* 2020.10 (Oct. 2020). ISSN: 1029-8479. DOI: 10.1007/jhep10(2020)174.

[38] F. Krauss, M. Greiner, and G. Soff. "Photon and gluon induced processes in relativistic heavy-ion collisions". In: *Progress in Particle and Nuclear Physics* 39 (1997), pp. 503–564. ISSN: 0146-6410. DOI: https://doi.org/10.1016/S0146-6410(97)00049-5. URL: https://www.sciencedirect.com/science/article/pii/S0146641097000495.

[39] Enrico Fermi. "On the Theory of Collisions between Atoms and Electrically Charged Particles". In: *Electromagnetic Probes of Fundamental Physics*. World Scientific, Sept. 2003, pp. 243–252. DOI: 10.1142/9789812704214_0026.

[40] C. F. v. Weizsäcker. "Ausstrahlung bei Stößen sehr schneller Elektronen". In: 88 (1934). DOI: 10.1007/BF01333110.

[41] E. J. Williams. "Nature of the high-energy particles of penetrating radiation and status of ionization and radiation formulae". In: *Phys. Rev.* 45 (1934), pp. 729–730. DOI: 10.1103/PhysRev.45.729.

[42] ATLAS Collaboration. "Measurement and interpretation of same-sign W boson pair production in association with two jets in pp collisions at $\sqrt{s} = 13$ TeV with the ATLAS detector". In: *Journal of High Energy Physics* 2024.4 (Apr. 2024). ISSN: 1029-8479. DOI: 10.1007/jhep04(2024)026.

[43] ATLAS Collaboration. "Measurements of electroweak $W^{\pm}Z$ boson pair production in association with two jets in pp collisions at $\sqrt{s} = 13$ TeV with the ATLAS detector". In: *Journal of High Energy Physics* 2024.6 (June 2024). ISSN: 1029-8479. DOI: 10.1007/jhep06(2024)192.

[44] ATLAS Collaboration. "Measurement of electroweak $Z(\nu\overline{\nu})\gamma jj$ production and limits on anomalous quartic gauge couplings in pp collisions at $\sqrt{s} = 13$ TeV with the ATLAS detector". In: *Journal of High Energy Physics* 2023.6 (June 2023). ISSN: 1029-8479. DOI: 10.1007/jhep06(2023)082.

[45] ATLAS Collaboration. "Fiducial and differential cross-section measurements of electroweak $W\gamma jj$ production in pp collisions at $\sqrt{s} = 13$ TeV with the ATLAS detector". In: *The European Physical Journal C* 84.10 (Oct. 2024). ISSN: 1434-6052. DOI: 10.1140/epjc/s10052-024-13311-6.

[46] ATLAS Collaboration. "Observation of photon-induced W^+W^- production in pp collisions at $\sqrt{s} = 13$ TeV using the ATLAS detector". In: *Physics Letters B* 816 (May 2021). ISSN: 0370-2693. DOI: 10.1016/j.physletb.2021.136190.

[47] Lyndon Evans. "The Large Hadron Collider". In: *New Journal of Physics* 9.9 (Sept. 2007), p. 335. DOI: 10.1088/1367-2630/9/9/335.

[48] ATLAS Collaboration. "The ATLAS Experiment at the CERN Large Hadron Collider". In: *JINST* 3 (2008). Also published by CERN Geneva in 2010, S08003. DOI: 10.1088/1748-0221/3/08/S08003. URL: https://cds.cern.ch/record/1129811.

[49] The CMS Collaboration. "The CMS experiment at the CERN LHC". In: *Journal of Instrumentation* 3.08 (Aug. 2008), S08004–S08004. DOI: 10.1088/1748-0221/3/08/s08004.

[50] L. Adamczyk et al. "Technical Design Report for the ATLAS Forward Proton Detector". In: (May 2015).

[51] M Albrow et al. *CMS-TOTEM Precision Proton Spectrometer*. Tech. rep. 2014. URL: https://cds.cern.ch/record/1753795.

[52] Christiane Lefèvre. "The CERN accelerator complex. Complexe des accélérateurs du CERN". 2008. URL: https://cds.cern.ch/record/1260465.

[53] Oliver Sim Brüning et al. *LHC Design Report*. CERN Yellow Reports: Monographs. Geneva: CERN, 2004. DOI: 10.5170/CERN-2004-003-V-1. URL: https://cds.cern.ch/record/782076.

[54] Werner Herr and B Muratori. *Concept of luminosity*. 2006. DOI: 10.5170/CERN-2006-002.361. URL: https://cds.cern.ch/record/941318.

[55] Corinne Pralavorio and Corinne Pralavorio. "Record luminosity: well done LHC". In: (2017). URL: https://cds.cern.ch/record/2295027.

[56] ATLAS Collaboration. *The ATLAS Experiment at the CERN Large Hadron Collider*. Tech. rep. 08. Aug. 2008, S08003–S08003. DOI: 10.1088/1748-0221/3/08/s08003.

[57] Joao Pequenao. "Computer generated image of the ATLAS inner detector". 2008. URL: https://cds.cern.ch/record/1095926.

[58] ATLAS Collabaration. "ATLAS pixel detector electronics and sensors". In: *Journal of Instrumentation* 3.07 (July 2008), P07007. DOI: 10.1088/1748-0221/3/07/P07007.

[59] ATLAS Collaboration. *ATLAS Insertable B-Layer Technical Design Report*. Tech. rep. 2010. URL: https://cds.cern.ch/record/1291633.

[60] ATLAS Collaboration. "Operation and performance of the ATLAS semiconductor tracker in LHC Run 2". In: *JINST* 17 (2022), P01013. DOI: 10.1088/1748-0221/17/01/P01013. arXiv: 2109.02591. URL: https://cds.cern.ch/record/2780336.

[61] A Vogel. *ATLAS Transition Radiation Tracker (TRT): Straw Tube Gaseous Detectors at High Rates*. Tech. rep. Geneva: CERN, 2013. URL: https://cds.cern.ch/record/1537991.

[62] ATLAS Collaboration. "The ATLAS Inner Detector commissioning and calibration". In: *The European Physical Journal C* 70.3 (Aug. 2010), pp. 787–821. ISSN: 1434-6052. DOI: 10.1140/epjc/s10052-010-1366-7.

[63] Joao Pequenao. "Computer Generated image of the ATLAS calorimeter". 2008. URL: https://cds.cern.ch/record/1095927.

[64] ATLAS Collaboration. *ATLAS liquid-argon calorimeter: Technical Design Report*. Technical design report. ATLAS. Geneva: CERN, 1996. DOI: 10.17181/CERN.FWRW.FOOQ. URL: https://cds.cern.ch/record/331061.

[65] T Davidek and (on behalf of the Atlas Tilecal system). "ATLAS Tile Calorimeter performance for single particles in beam tests". In: *Journal of Physics: Conference Series* 160.1 (Apr. 2009), p. 012057. DOI: 10.1088/1742-6596/160/1/012057.

[66] ATLAS Collaboration. "Energy linearity and resolution of the ATLAS electromagnetic barrel calorimeter in an electron test-beam". In: *Nuclear Instruments and Methods in Physics Research Section A: Accelerators, Spectrometers, Detectors and Associated Equipment* 568.2 (Dec. 2006), pp. 601–623. ISSN: 0168-9002. DOI: 10.1016/j.nima.2006.07.053.

[67] Hannah Herde. *Muon reconstruction performance in ATLAS at Run-II*. Tech. rep. Geneva: CERN, 2015. URL: https://cds.cern.ch/record/2059849.

[68] M. Arnaud et al. "Commissioning of the magnetic field in the ATLAS muon spectrometer". In: *Nuclear Physics B - Proceedings Supplements* 177-178 (2008). Proceedings of the Hadron Collider Physics Symposium 2007, pp. 265–266. ISSN: 0920-5632. DOI: https://doi.org/10.1016/j.nuclphysbps.2007.11.123. URL: https://www.sciencedirect.com/science/article/pii/S0920563207009528.

[69] Rosa Simoniello. *The ATLAS Level-1 Topological Processor: from design to routine usage in Run-2*. Tech. rep. Geneva: CERN, 2019. DOI: 10.1109/NSSMIC.2018.8824280. URL: https://cds.cern.ch/record/2649959.

[70] ATLAS Collabaration. "Operation of the ATLAS trigger system in Run 2". In: *Journal of Instrumentation* 15.10 (Oct. 2020), P10004–P10004. ISSN: 1748-0221. DOI: 10.1088/1748-0221/15/10/p10004.

[71] ATLAS Collaboration. *AFP Figures*. URL: https://twiki.cern.ch/twiki/bin/viewauth/Atlas/AFP_Figures.

[72] ATLAS Collaboration. "Topological cell clustering in the ATLAS calorimeters and its performance in LHC Run 1". In: *The European Physical Journal C* 77.7 (July 2017). ISSN: 1434-6052. DOI: 10.1140/epjc/s10052-017-5004-5.

[73] Matteo Cacciari, Gavin P Salam, and Gregory Soyez. "The anti-k_t jet clustering algorithm". In: *Journal of High Energy Physics* 2008.04 (Apr. 2008), pp. 063–063. ISSN: 1029-8479. DOI: 10.1088/1126-6708/2008/04/063.

[74] S. Catani et al. "Longitudinally-invariant k_t-clustering algorithms for hadron-hadron collisions". In: *Nuclear Physics B* 406.1 (1993), pp. 187–224. ISSN: 0550-3213. DOI: https://doi.org/10.1016/0550-3213(93)90166-M. URL: https://www.sciencedirect.com/science/article/pii/055032139390166M.

[75] Stephen D. Ellis and Davison E. Soper. "Successive combination jet algorithm for hadron collisions". In: *Physical Review D* 48.7 (Oct. 1993), pp. 3160–3166. ISSN: 0556-2821. DOI: 10.1103/physrevd.48.3160.

[76] Yu.L. Dokshitzer et al. "Better jet clustering algorithms". In: *Journal of High Energy Physics* 1997.08 (1997), p. 001. DOI: 10.1088/1126-6708/1997/08/001.

[77] M. Wobisch and T. Wengler. *Hadronization Corrections to Jet Cross Sections in Deep-Inelastic Scattering*. 1999. arXiv: hep-ph/9907280 [hep-ph].

[78] ATLAS Collaboration. "Jet reconstruction and performance using particle flow with the ATLAS Detector". In: *The European Physical Journal C* 77.7 (2017). ISSN: 1434-6052. DOI: 10.1140/epjc/s10052-017-5031-2.

[79] ATLAS Collaboration. "Reconstruction of primary vertices at the ATLAS experiment in Run 1 proton–proton collisions at the LHC". In: *The European Physical Journal C* 77.5 (May 2017). ISSN: 1434-6052. DOI: 10.1140/epjc/s10052-017-4887-5.

[80] ATLAS Collaboration. "Jet energy scale and resolution measured in proton-proton collisions at $\sqrt{s} = 13$ TeV with the ATLAS detector". In: *The European Physical Journal C* 81.8 (Aug. 2021). ISSN: 1434-6052. DOI: 10.1140/epjc/s10052-021-09402-3.

[81] ATLAS Collaboration. *Tagging and suppression of pileup jets with the ATLAS detector*. Tech. rep. Geneva: CERN, 2014. URL: https://cds.cern.ch/record/1700870.

[82] ATLAS Collaboration. "Measurements of b-jet tagging efficiency with the ATLAS detector using $t\bar{t}$ events at $\sqrt{s} = 13$ TeV". In: *Journal of High Energy Physics* 2018.8 (Aug. 2018). ISSN: 1029-8479. DOI: 10.1007/jhep08(2018)089.

[83] ATLAS Collaboration. *Calibration of light-flavour b-jet mistagging rates using ATLAS proton-proton collision data at $\sqrt{s} = 13$ TeV*. Tech. rep. Geneva: CERN, 2018. URL: https://cds.cern.ch/record/2314418.

[84] ATLAS Collaboration. "In situ calibration of large-radius jet energy and mass in 13 TeV proton-proton collisions with the ATLAS detector". In: *The European Physical Journal C* 79.2 (Feb. 2019). ISSN: 1434-6052. DOI: 10.1140/epjc/s10052-019-6632-8.

[85] Da Xu et al. *Constituent-Based W-boson Tagging with the ATLAS Detector*. Tech. rep. Geneva: CERN, 2023. URL: https://cds.cern.ch/record/2860189.

[86] ATLAS Collaboration. "Electron and photon performance measurements with the ATLAS detector using the 2015-2017 LHC proton-proton collision data". In: *Journal of Instrumentation* 14.12 (Dec. 2019), P12006–P12006. ISSN: 1748-0221. DOI: 10.1088/1748-0221/14/12/p12006.

[87] ATLAS Collaboration. "Electron reconstruction and identification in the ATLAS experiment using the 2015 and 2016 LHC proton-proton collision data at $\sqrt{s} = 13$ TeV". In: *The European Physical Journal C* 79.8 (Aug. 2019). ISSN: 1434-6052. DOI: 10.1140/epjc/s10052-019-7140-6.

[88] ATLAS Collaboration. "Electron efficiency measurements with the ATLAS detector using 2012 LHC proton–proton collision data". In: *The European Physical Journal C* 77.3 (Mar. 2017). ISSN: 1434-6052. DOI: 10.1140/epjc/s10052-017-4756-2.

[89] ATLAS Collaboration. "Muon reconstruction performance of the ATLAS detector in proton-proton collision data at $\sqrt{s} = 13$ TeV". In: *The European Physical Journal C* 76.5 (May 2016). ISSN: 1434-6052. DOI: 10.1140/epjc/s10052-016-4120-y.

[90] ATLAS Collaboration. "Identification and energy calibration of hadronically decaying tau leptons with the ATLAS experiment in *pp* collisions at $\sqrt{s} = 8$ TeV". In: *The European Physical Journal C* 75.7 (July 2015). ISSN: 1434-6052. DOI: 10.1140/epjc/s10052-015-3500-z.

[91] ATLAS Collaboration. *E_T^{miss} performance in the ATLAS detector using 2015-2016 LHC p-p collisions*. Tech. rep. Geneva: CERN, 2018. URL: https://cds.cern.ch/record/2625233.

[92] A. Ballestrero, E. Maina, and G. Pelliccioli. "Polarized vector boson scattering in the fully leptonic WZ and ZZ channels at the LHC". In: *Journal of High Energy Physics* 2019.9 (Sept. 2019). ISSN: 1029-8479. DOI: 10.1007/jhep09(2019)087.

[93] S. Navas et al. "Review of particle physics". In: *Phys. Rev. D* 110.3 (2024), p. 030001. DOI: 10.1103/PhysRevD.110.030001.

[94] R. Staszewski and J. Chwastowski. "Transport simulation and diffractive event reconstruction at the LHC". In: *Nuclear Instruments and Methods in Physics Research Section A: Accelerators, Spectrometers, Detectors and Associated Equipment* 609.2–3 (Oct. 2009), pp. 136–141. ISSN: 0168-9002. DOI: 10.1016/j.nima.2009.08.023.

[95] ATLAS Collaboration. *Performance of the ATLAS Forward Proton Spectrometer during High Luminosity 2017 Data Taking*. Tech. rep. Geneva: CERN, 2024. URL: https://cds.cern.ch/record/2890974.

[96] *LHC Optics Working Group. LHC Optics Web: LHC Run II pp physics optics*. URL: https://abpdata.web.cern.ch/abpdata/lhc_optics_web/www/opt2017.

[97] ATLAS Collabaration. "ATLAS data quality operations and performance for 2015–2018 data-taking". In: *Journal of Instrumentation* 15.04 (Apr. 2020), P04003–P04003. ISSN: 1748-0221. DOI: 10.1088/1748-0221/15/04/p04003.

[98] Andy Buckley et al. "General-purpose event generators for LHC physics". In: *Physics Reports* 504.5 (2011), pp. 145–233. ISSN: 0370-1573. DOI: https://doi.org/10.1016/j.physrep.2011.03.005. URL: https://www.sciencedirect.com/science/article/pii/S0370157311000846.

[99] Sebastian Weber. "Measurement of Vector Boson plus Jet Production Cross Sections and Dark Matter Interpretation with the ATLAS Detector". PhD thesis. Universität Heidelberg, Jan. 2023.

[100] Carlos A. Bertulani. "Photon Exchange in Nucleus-Nucleus Collisions". In: *International Journal of Modern Physics A* 18.05 (Feb. 2003), pp. 685–723. ISSN: 1793-656X. DOI: 10.1142/s0217751x03012357.

[101] ATLAS Collaboration. "Determination of the parton distribution functions of the proton using diverse ATLAS data from pp collisions at $\sqrt{s} = 7$, 8 and 13 TeV". In: *The European Physical Journal C* 82.5 (May 2022). ISSN: 1434-6052. DOI: 10.1140/epjc/s10052-022-10217-z.

[102] J. M. Campbell et al. *Event Generators for High-Energy Physics Experiments*. 2025. arXiv: 2203.11110 [hep-ph].

[103] Tilman Plehn. *Lectures on LHC Physics*. Springer Berlin Heidelberg, 2012. ISBN: 9783642240409. DOI: 10.1007/978-3-642-24040-9.

[104] B. Andersson et al. "Parton fragmentation and string dynamics". In: *Physics Reports* 97.2 (1983), pp. 31–145. ISSN: 0370-1573. DOI: https://doi.org/10.1016/0370-1573(83)90080-7. URL: https://www.sciencedirect.com/science/article/pii/0370157383900807.

[105] B. R. Webber. "A QCD Model for Jet Fragmentation Including Soft Gluon Interference". In: *Nucl. Phys. B* 238 (1984), pp. 492–528. DOI: 10.1016/0550-3213(84)90333-X.

[106] S. Agostinelli et al. "Geant4—a simulation toolkit". In: *Nuclear Instruments and Methods in Physics Research Section A: Accelerators, Spectrometers, Detectors and Associated Equipment* 506.3 (2003), pp. 250–303. ISSN: 0168-9002. DOI: https://doi.org/10.1016/S0168-9002(03)01368-8. URL: https://www.sciencedirect.com/science/article/pii/S0168900203013688.

[107] ATLAS Collaboration. "The ATLAS Simulation Infrastructure". In: *The European Physical Journal C* 70.3 (Sept. 2010), pp. 823–874. ISSN: 1434-6052. DOI: 10.1140/epjc/s10052-010-1429-9.

[108] J. Alwall et al. "The automated computation of tree-level and next-to-leading order differential cross sections, and their matching to parton shower simulations". In: *Journal of High Energy Physics* 2014.7 (July 2014). ISSN: 1029-8479. DOI: 10.1007/jhep07(2014)079.

[109] Torbjörn Sjöstrand et al. "An introduction to PYTHIA 8.2". In: *Computer Physics Communications* 191 (June 2015), pp. 159–177. ISSN: 0010-4655. DOI: 10.1016/j.cpc.2015.01.024.

[110] Johannes Bellm et al. "Herwig 7.0/Herwig++ 3.0 release note". In: *The European Physical Journal C* 76.4 (Apr. 2016). ISSN: 1434-6052. DOI: 10.1140/epjc/s10052-016-4018-8.

[111] Enrico Bothmann et al. "Event generation with Sherpa 2.2". In: *SciPost Physics* 7.3 (Sept. 2019). ISSN: 2542-4653. DOI: 10.21468/scipostphys.7.3.034.

[112] Simone Alioli et al. "A general framework for implementing NLO calculations in shower Monte Carlo programs: the POWHEG BOX". In: *Journal of High Energy Physics* 2010.6 (June 2010). ISSN: 1029-8479. DOI: 10.1007/jhep06(2010)043.

[113] ATLAS Collaboration. *Measurements of the W production cross sections in association with jets with the ATLAS detector*. Tech. rep. Geneva: CERN, 2014. URL: https://cds.cern.ch/record/1735193.

[114] ATLAS Collaboration. *Measurements of differential cross-sections in top-quark pair events with a high transverse momentum top quark and limits on beyond the Standard Model contributions to top quark pair production with the ATLAS detector*. Tech. rep. Geneva: CERN, 2021. URL: https://cds.cern.ch/record/2777237.

[115] ATLAS Collaboration. "Measurement of the $t\bar{t}$ production cross-section using $e\mu$ events with b-tagged jets in pp collisions at $\sqrt{s}$=13 TeV with the ATLAS detector. Measurement of the $t\bar{t}$ production cross-section using $e\mu$ events with b-tagged jets in pp collisions at $\sqrt{s}$=13 TeV with the ATLAS detector". In: *Phys. Lett. B* 761 (2016), p. 136. DOI: 10.1016/j.physletb.2016.08.019. arXiv: 1606.02699. URL: https://cds.cern.ch/record/2159581.

[116] Ilaria Brivio, Yun Jiang, and Michael Trott. "The SMEFTsim package, theory and tools". In: *Journal of High Energy Physics* 2017.12 (Dec. 2017). ISSN: 1029-8479. DOI: 10.1007/jhep12(2017)070.

[117] Carl Schmidt et al. "CT14QED parton distribution functions from isolated photon production in deep inelastic scattering". In: *Physical Review D* 93.11 (June 2016). ISSN: 2470-0029. DOI: 10.1103/physrevd.93.114015.

[118] O. J. P. Éboli and M. C. Gonzalez–Garcia. "Classifying the bosonic quartic couplings". In: *Physical Review D* 93.9 (May 2016). ISSN: 2470-0029. DOI: 10.1103/physrevd.93.093013.

[119] Christian Bierlich et al. "Robust Independent Validation of Experiment and Theory: Rivet version 3". In: *SciPost Physics* 8.2 (Feb. 2020). ISSN: 2542-4653. DOI: 10.21468/scipostphys.8.2.026.

[120] Czesław Stepniak. "Neyman-Pearson Lemma". In: *International Encyclopedia of Statistical Science*. Ed. by Miodrag Lovric. Berlin, Heidelberg: Springer Berlin Heidelberg, 2011, pp. 945–946. ISBN: 978-3-642-04898-2. DOI: 10.1007/978-3-642-04898-2_406.

[121] Glen Cowan et al. "Asymptotic formulae for likelihood-based tests of new physics". In: *The European Physical Journal C* 71.2 (Feb. 2011). ISSN: 1434-6052. DOI: 10.1140/epjc/s10052-011-1554-0.

[122] S. S. Wilks. "The Large-Sample Distribution of the Likelihood Ratio for Testing Composite Hypotheses". In: *The Annals of Mathematical Statistics* 9.1 (Mar. 1983). URL: http://www.jstor.org/stable/2957648.

[123] ATLAS Collaboration. "Luminosity determination in pp collisions at $\sqrt{s} = 13$ TeV using the ATLAS detector at the LHC". In: *The European Physical Journal C* 83.10 (Oct. 2023). ISSN: 1434-6052. DOI: 10.1140/epjc/s10052-023-11747-w.

[124] ATLAS Collaboration. "Search for high-mass $W\gamma$ and $Z\gamma$ resonances using hadronic W/Z boson decays from 139 fb^{-1} of pp collisions at $\sqrt{s} = 13$ TeV with the ATLAS detector". In: *Journal of High Energy Physics* 2023.7 (July 2023). ISSN: 1029-8479. DOI: 10.1007/jhep07(2023)125.

[125] ATLAS Collaboration. "Observation and Measurement of Forward Proton Scattering in Association with Lepton Pairs Produced via the Photon Fusion Mechanism at ATLAS". In: *Physical Review Letters* 125.26 (Dec. 2020). ISSN: 1079-7114. DOI: 10.1103/physrevlett.125.261801.

[126] ATLAS Collaboration. "Jet energy scale measurements and their systematic uncertainties in proton-proton collisions at $\sqrt{s} = 13$ TeV with the ATLAS detector". In: *Physical Review D* 96.7 (Oct. 2017). ISSN: 2470-0029. DOI: 10.1103/physrevd.96.072002.

[127] ATLAS Collaboration. "Electron and photon performance measurements with the ATLAS detector using the 2015-2017 LHC proton-proton collision data". In: *Journal of Instrumentation* 14.12 (Dec. 2019). ISSN: 1748-0221. DOI: 10.1088/1748-0221/14/12/p12006.

[128] ATLAS Collaboration. "Muon reconstruction performance of the ATLAS detector in proton-proton collision data at $\sqrt{s} = 13$ TeV". In: *The European Physical Journal C* 76.5 (May 2016). ISSN: 1434-6052. DOI: 10.1140/epjc/s10052-016-4120-y.

[129] ATLAS Collaboration. "Measurement of $W^{\pm}$ and Z-boson production cross sections in pp collisions at $\sqrt{s} = 13$ TeV with the ATLAS detector". In: *Physics Letters B* 759 (Aug. 2016). ISSN: 0370-2693. DOI: 10.1016/j.physletb.2016.06.023.

[130] ATLAS Collaboration. "Measurement of the W^+W^- production cross section in pp collisions at a centre-of-mass energy of $\sqrt{s} = 13$ TeV with the ATLAS experiment". In: *Physics Letters B* 773 (Oct. 2017). ISSN: 0370-2693. DOI: 10.1016/j.physletb.2017.08.047.

[131] ATLAS Collaboration. "Performance of missing transverse momentum reconstruction with the ATLAS detector using proton-proton collisions at $\sqrt{s} = 13$ TeV". In: *The European Physical Journal C* 78.11 (Nov. 2018). ISSN: 1434-6052. DOI: 10.1140/epjc/s10052-018-6288-9.

[132] Jan Kalinowski et al. "Same-sign WW scattering at the LHC: can we discover BSM effects before discovering new states?" In: *The European Physical Journal C* 78.5 (May 2018). ISSN: 1434-6052. DOI: 10.1140/epjc/s10052-018-5885-y.

[133] O. Kepka and C. Royon. "Anomalous $WW\gamma$ coupling in photon-induced processes using forward detectors at the CERN LHC". In: *Physical Review D* 78.7 (Oct. 2008). ISSN: 1550-2368. DOI: 10.1103/physrevd.78.073005.

ACKNOWLEDGEMENTS

Completing this PhD has been as much a personal journey as it has been an academic one. I consider it a privilege to acknowledge the many people who have supported, guided, and inspired me along the way.

First and foremost, I would like to thank my supervisor, Prof. Dr. Monica Dunford, for giving me the opportunity not only to begin this PhD but also to move to Germany. Her trust in me and the many opportunities she provided—to work on a wide range of projects and to grow as a researcher—have been invaluable. Despite her numerous responsibilities within the collaboration, she always made time for our regular discussions, for which I am truly grateful.

I am also thankful to Prof. Dr. Stephanie Hansmann-Menzemer for agreeing to be my second supervisor. Her support through the Research Training Group was especially meaningful during the early stages of my PhD, and her work setting up the Women's Initiative was impactful.

A heartfelt thank you goes to the ATLAS Forward Physics community. From the beginning, they welcomed me warmly—even when I was still finding my way, and entrusted me with the responsibility of commissioning work alongside the experts of the field. I'm especially thankful for the opportunity to present at LHCP in 2023, which remains one of the most memorable experiences of my PhD. I extend special thanks to Kristin for her invaluable insights and many thoughtful discussions throughout the course of this analysis.

To the F8 and F11 groups at KIP: thank you for fostering such a supportive and enjoyable working environment. What began as a group of colleagues quickly became a second family. A special thanks goes to Falk and Thomas, who came to my rescue more than once in the final months of writing. From setting up a rooster for my specific plotting scripts and answering to my questions at almost every hour, their help was indispensable.

I'm grateful to those who helped review different chapters of this thesis: Anke, Falk, Isa, Lisa, Lucas, and Mathias. A special thanks to my sister Vidura, who impressively read through nearly the entire thesis—and somehow managed to stay sane.

Finally, I would like to express my deepest thanks to my friends and family for their patience, love, and unwavering support throughout this journey. Without their quiet strength and belief in me, this PhD would not have been possible.